IMPERIAL COLLEGE

Novel Application of MEMS-Type Surfaces to Control Protein Crystallization

Department of Chemical Engineering

Agnese Zicari

MPhil

© 2015 by Agnese Zicari

All rights reserved.

'This is entirely my own work otherwise it has been clearly referenced'

'The copyright of this thesis rests with the author and is made available under a Creative Commons Attribution Non-Commercial No Derivatives license. Researchers are free to copy, distribute or transmit the thesis on the condition that they attribute it, that they do not use it for commercial purposes and that they do not alter, transform or build upon it. For any reuse or redistribution, researchers must make clear to others the license terms of this work'

TABLE OF CONTENTS

CONTENT **PAGE**

- **ABSTRACT** vi
- **DEDICATION** vii
- **ACKNOWLEDGMENTS** viii
- **LIST OF FIGURES & TABLES** ix
- **CHAPTER 1** – ***Introduction*** 1
- **CHAPTER 2** – ***The Aggregation of Proteins*** 5
  - ***2.1 Theory*** 5
    - ***2.1.1*** *The classical aggregation theory in comparison to the recent aggregation models* 5
    - ***2.1.2*** *Aggregation vs. crystallization* 12
  - ***2.2 Applications*** 19
  - ***2.3 Techniques for Detecting and Measuring Aggregation*** 23
- **CHAPTER 3** – ***The Crystallization of Proteins*** 28
  - ***3.1 Theory*** 28
    - ***3.1.1*** *The modelling of protein adsorption and homogeneous crystallization* 28
    - ***3.1.2*** *The modelling of protein heterogeneous crystallization* 34
    - ***3.1.3*** *The classical crystallization theory in comparison to the recent crystallization models* 38
  - **3.2** ***Applications*** 46
  - **3.3** ***Techniques for Detecting and Measuring Crystallization*** 48
- **CHAPTER 4** – ***Surfaces with controlled roughness*** 52
  - ***4.1 Nano-patterned Surfaces*** 52

· *4.1.1 Techniques to produce nano-patterned surfaces* 52

• ***4.2 MEMS & NEMS: substrates for the characterization of protein adsorption and crystallization*** 58

· *4.2.1 The use of MEMS and NEMS substrates to adsorb & crystallize proteins: repeatability issues* 58

· *4.2.2 The fabrication of MEMS-substrates for protein adsorption & crystallization by nano-imprinting* 60

· *4.2.3 The fabrication of NEMS-substrates for protein adsorption & crystallization by interference lithography* 72

· *4.2.4 The modification and characterization of MEMS & NEMS surfaces* 73

o **CHAPTER 5 – *Crystallization Trials*** 85

• ***5.1 Introduction to the Crystallization Trials: heterogeneous adsorption and nucleation*** 85

• **5.2 *Optimization of the HEWL Crystallizing Formulation*** 90

· *5.2.1 Crystallization via an air-depleted micro-batch method* 101

o **CHAPTER 6 – *Experimental Design & Methodology*** 106

• ***6.1 Introduction to the Experiments' Design*** 106

· *6.1.1 Introduction the heterogeneous nucleation of lysozyme* 106

· *6.1.2 Planning experiments with protein solutions* 108

· *6.1.3 Reducing the uncontrollable factors* 109

· *6.1.4 Making simple procedures to manufacture MEMS-type substrates* 109

· *6.1.5 Homogeneous vs. heterogeneous crystallization times* 109

• ***6.2 Reduction of Unwanted Interference Factors*** 110

· *6.2.1 Reduction of the salt interference in the nucleating solution* 110

· *6.2.2 Reduction of the air droplet entrainment and dust contamination by the interface* 114

• ***6.3 A Simple Procedure to Manufacture Controlled Surface Features*** 116

· *6.3.1 Introduction* 116

· *6.3.2 The manufacture of substrates by nano-imprinting* 117

· *6.3.3 The manufacture of substrates by interference lithography* 118

· *6.3.4 Surface chemistry modification procedures* 119

• ***6.4 Comparing Homogeneous vs. Heterogeneous Crystallization Times*** 127

· *6.4.1 Making ⇒ characterising the low-salt formulation & implementing the air-depleted method* 127

· ***6.4.2*** *Designing & testing the robustness of the air-depleted micro-batch method* 129

o **SUMMARY & RECOMMENDATION** 139

o **REFERENCES** 142

o **APPENDICES**

• **Appendix A –** ***Contact details relating to the multi-institutional collaborations*** i

• **Appendix B –** ***Abstracts and sketches relating to the exploratory simulation work*** ii

Abstract

Addressing the problem of protein crystallization bottlenecks is a broadly regarded, but complex, research topic. High-throughput screening techniques have been developed in the recent decades to proceed with the investigations in this field. Some of these techniques are regularly used to detect the best crystallizing formulations and form crystals that are suitable for characterization. However, although slow crystallization processes can produce regular (or large) crystals, a faster growth rate is aimed for. Videlicet, gaining a certain control over the nucleation (or crystal growth) rate of proteins would be a breakthrough in modern science.

In this work, we focus on developing a low-concentration crystallizing solution and on the design of a novel device to crystallize lysozyme from the above solution within an air-depleted micro-batch environment. It was, de facto, observed, during this project, that the heterogeneous crystallization of lysozyme in standard laboratories and from its conventionally formulated solutions, hardly, would lead to a real understanding of this process. Videlicet, the effect of the solid substrate topographies (or chemistries) on the lysozyme heterogeneous nucleation rate might be altered also by interfering solution factors. Hence, the introduction of a controlled crystallization environment, including surfaces bearing highly controlled features, and the formulation of a low-salt precipitating solution were necessary.

This would also mean that, although, so far, a variety of surface effects on the crystallization of conventionally formulated protein solutions have been observed, a far better characterization of protein heterogeneous nucleation, and crystal growth, could be attained. Videlicet, reducing the local effect of interfering, or uncontrollable, factors, almost certainly, would lead to a better definition, and control, of the protein nucleation dynamics. Also, for the same reason, it is pivotal that substrates with strictly controlled chemistries (or topographies) are employed. Indeed, gaining a real understanding of the criteria that govern the protein heterogeneous nucleation would be the ultimate scope of any work in this research field.

"Try everything that can be done. Be deliberate.
Be spontaneous. Be thoughtful and painstaking.
Be abandoned and impulsive. Learn your own possibilities."

George Bellows, 1920

In Memory of Anna Monaco

Acknowledgements

All the staff and colleagues from the:

Imperial College-South Kensington Campus (London), **Nanofilm** (Germany), **Obducat AB** (Sweden), **Eulitha AG** (Switzerland), **UCL Cancer Institute and Wolfson Institute for Biomedical Research** (London), **London Centre for Nanotechnology (**London**)**, **King's College** (London), **Science and Technology Facilities Council** (Oxford), **Toshiba Research Europe Limited** (Cambridge), **The Manufacturing Engineering Centre** (Cardiff), **X-ray Photoelectron Spectroscopy facility in School of Chemistry** (Nottingham) and **Yield Engineering Systems** (USA).

List of Figures & Tables

FIG 2.1
The phase diagram of copolymers with 100 and 1000 constituting units: 1 phase above the curve and 2 phases below it. The polymer with n = 100 is represented by both the Fields Gregg theory (continuous line) and the Flory-Huggins theory (dotted line).
pp. **6**

FIG 2.2
Where A_1 represents the monomer species, $(A_1)^{''}$ represents the inactivated monomer species, (where $+k^{''}$ and $-k^{''}$ are, respectively, the forward and backward inactivation rate constants); n^* represents the critical nucleus (where $+k^*$ and $-k^*$ are, respectively, the rate constants for the formation and disassembly of this nucleus); A_i represents the nucleus i-mers and A_{i+1} represents the growing i+1-mers (where $+k^i$, and $-k^i$ are, respectively, the forward and backward rate constants for the following ith growth reaction, (Arnaudov, 2007).
pp. **8**

FIG 2.3
The phase behaviour of proteins: where C/cm is the millimolar concentration of the protein and T/K is the temperature in Kelvin. FS represents the fibrillar phase in equilibrium with the solution. DOS represents the disordered oligomer phase in equilibrium with the native oligomer phase (that is, the DOS phase is made of fully folded, partially folded, and unfolded peptides) and NOS represents the ordered native oligomer phase in equilibrium with the solution (that is, the NOS phase is made of fully folded α-helical peptides). The simulation shows a dotted black line, which represents T_f, i.e., the peptide folding temperature. The red open circles indicate the points at which no aggregation has been observed, and the red filled circles indicate the points at which aggregation has been observed. At point A, the protein solution is supersaturated with respect to the fibrillar phase only. At point B, the protein solution is supersaturated with respect to both the oligomeric and fibrillar phases, (Ricchiuto et al., 2012).
pp. **9**

FIG 2.4
*The effects of the temperature decrease on the thermodynamics, and the kinetics, of the peptide aggregation have been simulated. Specifically the above simulation has been run at a lag time of 0.47 ms (t = 0.47 ms) and at different concentrations (C = 7 mM, green ▲, C = 1 mM, red ■ and C = 0.1 mM, black ●), after instant cooling from T (390 K) to T_s (361, 351, 306, 251, 222, 195 K). **(a)** Shows 〈N〉 the average total number of oligomers in solution and the numbers by the plot symbols that represent 〈n〉, i.e., the average size of the largest oligomer in solution; **(b)** Shows the average time t to form an oligomer of size 10 at 2 different concentrations (C = 7 mM and C = 1 mM), and of size 5 (at C = 0.1 mM); **(c)** Shows the α-helical content (dashed line) and the β-sheet content (solid line) for the largest oligomer in solution; **(d)** Shows the concentration that is left in solution, (Ricchiuto et al., 2012).*
pp. **10**

FIG 2.5
The time-dependent formation of the fraction fibril mass is plotted against time while increasing the initial monomer concentration, (Cohen et al., 2012).
pp. **11**

FIG 2.6
2-Amino-5-guanidinopentanoic acid, (arginine).
pp. **16**

FIG 2.7
A simple representation of the colloidal aggregation process.
pp. **17**

FIG 2.8
The DLVO theory claims that the interaction between 2 particles (or a particle and a solid surface) in the presence of electrolytes depends on the combination of the Coulombic repulsive forces (V_R) and Van der Waals attractive forces (V_A), (Boström et al. 2006).
pp. **18**

FIG 3.1
The folded lysozyme is a compact protein of 129 amino acids that has five α helical regions (the region that runs from residue 109 to 115 and other two regions that run from residues 80 to 84 and 120 to 124). Also it has five β sheet regions, random coils and β turns. During adsorption, the protein hydrophilic and hydrophobic portions will try to match with the hydrophilic and hydrophobic surface sections, respectively, in an attempt to reach the ensemble energy minimum. The energy barrier of adsorption is, usually, described by the Gibbs free energy of adsorption $\Delta G_{ads} = \Delta H_{ads} - T \Delta S_{ads}$ where ΔG_{ads} represents the change in the system free energy, H is the enthalpy, T is the temperature and S is the entropy, (the lysozyme monomer structure is from the PDB, file 8LYZ).
pp. **29**

FIG 3.2
The unfolded protein (U) is in a very fast equilibrium with its mis-folded intermediate form (I). This, in turn, is in a slow equilibrium with its natural form (N), (Creighton, Protein Structure, Second Edition, IRL Press, 2002).
pp. **33**

FIG 3.3
The normalized nucleation rates have been plotted against the ε parameter, which expresses the effects of all the controllable parameters (such as temperature, buffers, salts, pH, concentrations or additives). ***Green****: the lysozyme crystallization induction times from the literature, (Pullara et al., 2005).* ***Red****: the data on lysozyme crystallization; these data have been produced in different studies at different pH, temperature, and solute or salt concentrations.* ***Black****: sickle hemoglobin (HbS) fiber initiation kinetics, (Vaiana et al., 2005). In* ***Blu****: data derived from the universal scaling properties of critical fluctuations, (Pullara et al., 2005).*
pp. **42**

FIG 3.4
The hanging drop method.
pp. **49**

FIG 4.1 *The diverse applications of MEMS within the nanotechnology sector. The data have been reported from the Loadpoint website.*
pp. **53**

FIG 4.2
The pattern of the UV-curable polymer presents a 180 nm pitch, 126 nm height and 55 nm width after the AFM analysis from the Obducat clean rooms, (Obducat ltd ©, 2010).
pp. **63**

FIG 4.3
The data relating to the AFM analysis (in tapping mode), from the Toshiba Research Europe limited clean rooms, show that the pattern of the UV-curable polymer has a 175 nm pitch, "60 nm" height and 55 nm width, (Agnese Zicari ©, 2010).
pp. **63**

FIG 4.4
The Veeco 3100 atomic force microscope.
pp. **64**

FIG 4.5
The height of the features, which was recorded in this second set of experiments, was 60 nm. That is, there is a disagreement between the 2 different sets of experiments for the height dimension only. This different value stems from an artefact of the cantilever tip that was used in this second set of experiments. That is, its geometry (and, possibly, its chemistry) did not allow a real measurement of this dimension. There is a full match, indeed, for all the other dimensions.
pp. **64**

FIG 4.6
The scanning pattern that was performed with the Kla-Tencor, P15 surface profiler. The centre position coordinates were x = – 28074.87 and y = + 28636.36, (Agnese Zicari ©, 2010).
pp. **65**

FIG 4.7
The 1st series ***(a)*** *and 2nd series* ***(b)*** *of the 9000 μm line scans. The wafer scans were mapped on four lines each (a red arrow indicates the position of each line).* ***(a)*** *The 1st scan series from left to right: the 1st to 4th line positions (at the top) & relating analyses (at the bottom).* ***(b)*** *The 2nd scan series from left to right: the 1st to 4th line positions (at the top) & relating analyses (at the bottom), (Agnese Zicari ©, 2012).*
pp. **66**

FIG 4.8
(a) The 3rd 9000 µm × 9000 µm scan, which is mapped on 2000 lines. (b) The imperfections in the mapped areas were observed also under light microscopy, (Obducat ltd ©, 2010).
pp. **67**

FIG 4.9
The measurement of the wafer deformation: no thickness variation or warp were observed. That is, the wafer bow shows regular. The top and bottom profiles represent the 1st and 2nd scan, respectively.
pp. **68**

FIG 4.10
The HM1400 by GSI Lumonics, in the manufacturing engineering centre in Cardiff, (left). The method calibration lines, that were performed on a 600 µm thick spare wafer, are shown (right).
pp. **69**

FIG 4.11
The dicing arrangement to detect the defective sections (left). A picture of the diced wafer is also shown (right), (Agnese Zicari ©, 2010).
pp. **70**

FIG 4.12
The edge of the silicon wafer chips after dicing, (Agnese Zicari ©, 2010).
pp. **70**

FIG 4.13
(a) The top scan was taken on the sample a without treating it with the oxygen plasma. (b) The bottom scan was taken on the sample b after treating it with both the oxygen plasma and the precipitant solution, (Agnese Zicari ©, 2010).
pp. **71**

FIG 4.14
The description and representation of the pattern specifications, (Eulitha ltd ©, 2010).
pp. **73**

TAB 4.1
The description of the piranha activation protocols, (Agnese Zicari ©, 2009).
pp. **74**

FIG 4.15
(a) The CA (80.3°) of the epoxy-surface after reaction, on the left, while, on the right (b), the silanized epoxy-surface has been treated, once more, with oxygen plasma (CA 9.8°). When the latter was stored in a vacuum oven (for 2 hrs at 120 °C) there was not a recovery of the original contact angle in (a), (Agnese Zicari ©, 2009).
pp......**76**

FIG 4.16
(a) The patterned epoxy-surface on the left (CA 72.9°) and (b) the patterned epoxy-surface after plasma treatment on the right (CA 13.6°), (Agnese Zicari ©, 2009).
pp. **76**

FIG 4.17
The surface was treated under vacuum (and temperature) after cleaning, plasma treatment and exposure to the precipitant solution. The contact angle was found reverted to a value close to the original value (CA 80.8°), (Agnese Zicari ©, 2009).
pp. **76**

FIG 4.18
The AFM & SEM analysis of the sub-micron pattern after cleaning, oxygen plasma treatment and exposure to the precipitant solution. Top (a): the AFM analysis. Left; the analysis of a 4µ square area. Right; the Z-axis values showing the intact pattern (the height dimensions show altered due to the tip size). Bottom (b): the SEM Analysis. On the left; the picture of the pattern after plasma treatment only. On the right; the picture the pattern after performing all the 3 above steps, (Agnese Zicari ©, 2010).
pp. **77**

FIG 4.19
The XPS technique measures the kinetic energies of the emitted photoelectrons. After that the photoelectrons' energy has been measured, the binding energies of the photoelectrons are calculated according to the Planck-Einstein equation. This in turn allows to, quantitatively and qualitatively, describe the atomic composition of the sample surface, (http://www.phy.cuhk.edu.hk/course/surfacesci/mod3/m3_s1.pdf).
pp. **78**

FIG 4.20
The XPS analysis of some silanized substrates. Sample 1 and 2 have been methyl-trimethoxy silane treated, while sample 3 has been 3,3,3-trifluoropropyl-trimethoxy silane treated. Sample 3 shows very little fluorine content, that is, it shows very little degree of substitution when it is compared to sample 1 and 2.
pp. **79**

FIG 4.21
A representation of the ellipsometric analysis: it measures the change in the polarization state of light after reflection from the surface of a sample. The polarized light, once this has been measured, can provide information relating to the substrate material optical properties or the thickness of any layer that has been deposited on it, (http://www.aps.org/units/fiap/meetings/presentations/upload/tompkins.pdf).
pp. **80**

FIG 4.22
Ellipsometric analysis of the delta (Δ) and psi (Ψ) parameters at different angles of incidence (AOI). a) The profile of the delta values for the 3-aminopropyl-triethoxysilane treated surfaces at Time = 0 (left) and after exposure to the original precipitant solution, Time = 14 days (right). b1) & b2) The profiles of the Δ and Ψ values for the 3-aminopropyl-triethoxysilane, the 3-mercaptopropyl-trimethoxysilane, the 3,3,3-trifluoropropyl-trimethoxysilane and the methyl-trimethoxy silane treated surfaces after exposure to the original precipitant solution for 14 days (Agnese Zicari ©, 2009).
pp. **81/82**

TAB 4.2
This table summarizes the average CA values for the different silanized surfaces, (http://www.gelest.com).
pp. **83**

FIG 4.23
A representation of the anhydrous deposition of silanes, (Agnese Zicari ©, 2010).
pp. **83**

FIG 5.1
The picture shows some of the UV microscopy exploratory observations. That is, it shows a lysozyme solution after a few hours crystallization on a silicon slide. The fluorescence signal is much weaker than predicted and the technique was non utilizable as a result of this.
pp. **88**

FIG 5.2
The representation of the crystal forms from the seven crystal systems.
pp. **90**

FIG 5.3
The crystallization of lysozyme after 24 hrs is shown in these pictures (top pictures), and the details relating to the crystal forms are shown below these (bottom pictures). The pictures have been taken with a Leica Microscope M165C, (Agnese Zicari ©, 2009).
pp. **93**

FIG 5.4
***(a)** A chosen lysozyme crystal has been tested under x-rays. **(b_1 & b_2)** The diffraction patterns of the crystal from picture (a) are shown. **(c)** This picture shows the gel electrophoresis of the crystallizing solution, where the crystal in (a) formed.*
pp. **94**

FIG 5.5
The correlation coefficients of the lysozyme crystallizing solutions with decreasing concentration (20 mg/ml, 15 mg/ml, 10 mg/ml and 5 mg/ml) have been compared, after 220 nm filtration, (Agnese Zicari ©, 2012).
pp. **96**

FIG 5.6
The lower concentration lysozyme solution has been filtered with 5 nm, 10 nm, 20 nm cut-off Millipore syringe filters: from the top: (a) "5 nm", (b) 10 nm and (c) 20 nm; (these data have not been averaged intentionally), (Agnese Zicari ©, 2010).
pp. **97**

TAB 5.1
This table summarizes the 1st & 2nd peak mean hydrodynamic diameter for the 5 mg/ml solution, in the first 4 hrs, (Agnese Zicari ©, 2015).
pp. **98**

FIG 5.7
The 5 mg/ml lysozyme solution has been filtered after 24 hrs with 220 nm cut-off syringe filters (these data have not been averaged intentionally), (Agnese Zicari ©, 2010).
pp. **98**

FIG 5.8
The (350 nm) turbidity values of the 5 mg/ml lysozyme solution at low precipitant concentration ≈ 3 % v/v: ***(a)*** *The plot over 24 hrs shows that the nucleation process may start between 20 and 24 hrs (a 10 mm path length was used on this occasion).* ***(b)*** *The plot over 48 hrs reveals that a sedimentation process may blur the nucleation process since time 1 hr (40 mm path length was used on this occasion), (Agnese Zicari ©, 2010).*
pp. **100**

FIG 5.9
The crystallization devices with the inlet and outlet points (✵): (a) The initial design (b) The most recent design with internal and external cell dimensions of ≈ 20 mm (height), 60 mm (side), and a cylindrical internal "tank" of 5 × 14 mm, (Agnese Zicari ©, 2009).
pp. **101**

FIG 5.10
The crystallization of lysozyme from the original formulation on bare silica in the presence of visible air droplets after: 24 hrs (a) and 48 hrs (b). A Wild/Leica M420 photomicroscope provided with an Olympus DP70 camera was used in this instance, (Agnese Zicari ©, 2009).
pp. **103**

FIG 5.11
The air-depleted crystallization of the 5 mg/ml lysozyme solution (new formulation) after 6 hrs only: (a) top - the details of the crystal formed on the epoxy substrate; (b) bottom - the details of the crystal formed on the epoxy substrate after exposure to the oxygen plasma. The pictures have been taken with a Leica Microscope M165C under UV light, (a 500 μm scale-bar was set), (Agnese Zicari ©, 2010).
pp. **104**

FIG 5.12
The air-depleted crystallization of the 5 mg/ml lysozyme solution (new formulation) after 24 hrs: (a) top - the details of the crystal formed on the epoxy substrate; (b) bottom - the details of the crystal formed on the epoxy substrate after exposure to the oxygen plasma. The pictures have been taken with a Leica Microscope M165C under UV light, (a 500 μm scale-bar was set), (Agnese Zicari ©, 2010).
pp. **105**

FIG 6.1
The protein homogeneous & heterogeneous nucleation dynamics differ in that the latter is affected, also, by the surface chemical potentials.
pp. **106**

FIG 6.2
A flow-chart of the solution & surface controllable & non-controllable factors, (Agnese Zicari ©, 2015).
pp. **107**

FIG 6.3
The repeatability issue is, intrinsically, associated with performing experiments on proteins, (Agnese Zicari ©, 2010).
pp. **108**

FIG 6.4
The ellipsometric analyses represent the delta values (Δ) against the lambda (λ) or angle of incidence variations (AOI) for the silanized surfaces before & after exposure to the precipitant solution. The 3-aminopropyl-triethoxysilane (⬥) and 3-mercaptopropyl-trimethoxysilane (Δ) treated surfaces before exposure, for the samples in (a) and (b). The 3-aminopropyl-triethoxysilane (•), 3-mercaptopropyl-trimethoxysilane (⬥), 3,3,3-trifluoropropyl-trimethoxysilane (■) and methyl-trimethoxysilane (x) treated surfaces and the bare-silicon (-) surface after 14 day exposure to the precipitant solution, for the samples in (a) and (b), (Agnese Zicari ©, 2009).
pp. **111/112**

FIG 6.5
A sketch representing how air droplets may interfere with interfacial phenomena, (Agnese Zicari ©, 2010).
pp. **114**

FIG 6.6
The micro-batch crystallization devices that have been designed and manufactured in-house. The most recently manufactured design is shown on the left and a proposed new design is shown on the right, (Design and model by Agnese Zicari ©, 2009).
pp. **115**

FIG 6.7
In the picture;
A is the area, V is the volume, t is the time and x, y, z are the Cartesian variables.
PSF and TF are the protein solution and topographic factors (respectively);
μ_{ps}, μ_R and μ_{CD} are the chemical potential contributions of the protein solution, surface roughness and surface chemistry (respectively);
μ_{sol} and μ_{surf} are the solution and surface chemical potentials (respectively);
U and K: are unknown and known variables (respectively), (Agnese Zicari ©, 2014).
pp. **116**

FIG 6.8
A representation of the stealth-dicing process (left). A picture of the wafer after stealth-dicing (right), (Agnese Zicari ©, 2010).
pp. **118**

FIG 6.9
A representation of the interference lythography process: a EUV light beam is used to generate 4 coherent light beams that, after 45° diffraction, recombine (on the spin-coated silicon based resist) to form, after interference, a regular pattern of exposed dots.
pp. **119**

FIG 6.10
In this picture a mini-reactor, which was designed and manufactured in-house (PTFE), is shown, (Agnese Zicari ©, 2009).
pp. **120**

FIG 6.11
From left to right the average contact angles of the substrates that were treated with different silanes: 1st, 3-aminopropyl-triethoxysilane; 2nd, 3-mercaptopropyl-trimethoxysilane; 3rd, 3,3,3-trifluoropropyl-trimethoxysilane and 4th, methyl-trimethoxysilane.
pp. **122**

FIG 6.12
In this picture the XPS fluorinated/carbonated ratio for the 3,3,3-trifluoropropyl-trimethoxysilane functionalised substrates shows that their surfaces have a highly inhomogeneous chemical distribution.
pp. **122**

FIG 6.13
The optical microscopy (a) & SEM (b) of the patterned epoxy-substrates: the signs of edge-delamination were observed after 24 hr exposure to wet-conditions, (Agnese Zicari ©, 2010).
pp. **125**

FIG 6.14
The AFM analysis of the epoxy-patterned substrates after exposure to the oxygen plasma and precipitant solution (on the left) & the SEM analysis of the epoxy-patterned substrates after exposure to the oxygen plasma only (in the middle), and after exposure to the oxygen plasma and precipitant solution (on the right), (Agnese Zicari ©, 2010).
pp. **126**

FIG 6.15
The light microscopy of the lysozyme crystals that have formed from the 5 mg/ml solutions after 24 hrs at RT, (Agnese Zicari ©, 2010).
pp. **128**

FIG 6.16
A section of the reflection sphere, which is generated through a crystal lattice plane set.
pp. **129**

FIG 6.17
A metaphase nucleation model; it describes time-related protein-mass fluctuations, (Agnese Zicari ©, 2011)
pp. **130**

FIG 6.18
The correlation between the correlation coefficient decays and the 2 peaks of intensity scattering has been represented in this picture, (Agnese Zicari ©, 2015).
pp. **135**

FIG 6.19
The (350 nm) turbidity values of the 5 mg/ml lysozyme solution at high precipitant concentration ≈ 8 % v/v: (a) the plot over 48 hrs may show that the nucleation process is progressively increasing over the 48 hrs (a 10 mm path length was used on this occasion). (b) the plot over 66 hrs may reveal that for longer path lengths the sedimentation process blurs the nucleation process since time 0 (a 40 mm path length was used on this occasion), (Agnese Zicari ©, 2010).
pp. **137**

FIG 6.20
The (350 nm) turbidity values of the 5 mg/ml lysozyme solution at low precipitant concentration ≈ 3 % v/v: the turbidity data are plotted over 48 hrs and these may reveal that the heterogeneous nucleation is proceeding over time (10 mm path length was used on this occasion), (Agnese Zicari ©, 2010).
pp. **138**

Chapter 1

Introduction

According to the historical data that are available in the literature, the crystallization of proteins should be an inexpensive and straightforward process. Indeed, the crystallization of different proteins (such as hemoglobin) has been well performed since 1840 by several researchers (including Hunefeld and Hoppe-Seyler). About one hundred years later Max Perutz et al. have determined the 3-D structure of hemoglobin by x-ray diffraction (Hazelwood, 2001). At present, the crystallization of proteins is, in fact, performed in a variety of scientific and manufacture fields (such as protein structure research or therapeutic protein production). Nevertheless, making proteins crystallize is, still, the major rate-limiting step in most of the protein industrial operations. That is, since most of the common protein crystallization protocols yield only 30 % of the input protein, and few of these crystals are suitable for crystallography, this process has become a troublesome bottleneck for industrial production. It is, indeed, well known that protein crystals are generally characterised by x-ray diffraction and that this technique is usable only for regular, and large enough, crystals. That is, only crystals of around 0.1 mm, or larger, size are characterizable by x-ray.

A common method that is, nowadays, used to ameliorate the crystallization output (as well as quality) is the screening of the crystallization conditions for the protein of interest. At present, high-throughput crystallization equipment has been developed to straightforwardly perform the above-mentioned screening, in an attempt to improve the production yield rate. That is, the use of high-throughput methods to perform the screening of the crystallization conditions is, indubitably, necessary to produce good quality protein crystals within a reasonable time. Also, the use of high-throughput equipment allows for a user-friendly detection and characterization of the intrinsic (and environmental) factors that affect the

the crystallization process. This would become very laborious, or impossible, when lower throughput laboratories were used instead. It is worth mentioning in this regard that there are additional methods that are used to improve the protein stability and, therefore, facilitate its crystallization. Indeed, the protein molecular structure is often modified into a stable rigid structure, since this could make the protein easier to crystallize. Recombinant proteins (that is, proteins that are provided with an affinity tag) are generally used for this purpose. Also, for the same purpose, proteins may be truncated, or chemically modified, on specifically chosen residues, (Stevens, 2000; Heinemann et al., 2003).

Multi-institutional collaborations are now developing to optimize the screening methods for protein production, purification or crystallization. Key competences from biology, biochemistry, biophysics, computing or mechanical engineering have been combined for this purpose. At present, a wide group of internationally worldwide renowned institutes are actively working in this sense, and some of these are listed here blow:
the Structural Genomics Consortium (SGC), the Architecture et Fonction des Macromolécules Biologiques, the Berkeley Structural Genomics Center, the China Structural Genomics Consortium, the Integrated Center for Structure and Function Innovation, the Israel Structural Proteomics Center, the Joint Center for Structural Genomics, the Midwest Center for Structural Genomics, the New York Structural Genomix Research Center for Structural Genomics, the Northeast Structural Genomics Consortium, the Oxford Protein Production Facility, the Protein Sample Production Facility, the Max Delbrück Center for Molecular Medicine, the RIKEN Structural Genomics & Proteomics Initiative and the SPINE2-Complexes.
Recently, Nicholson Price (from the Hauptmann-Woodward Institute) has performed the high-throughput crystallization screening of 1,536 wells and screened each of the proteins failing to produce crystals during this first screening in 300 – 500 different conditions. Also, Edwards et al. (from the University of Toronto) and the SGC have systematically investigated the stabilizing effect of different ligands (Vedadi et al., 2006). Finally, with respect to the research advances that have followed the enhancement of high-throughput screening technologies, it is

worth pointing out that the database of 3-dimensionl protein structures (i.e., the Protein Data Bank, PDB) has remarkably grown since its foundation in the 1970's (http://www.wwpdb.org).

On the other hand, the scientific community has given partial attention to the study of protein heterogeneous crystallization, until now. Indeed, the grouping of proteins in the bulk has been, repeatedly, described, in the literature. That is to say, in most of the experimental studies from the literature, lysozyme has been, conventionally, formulated under different conditions and phase diagrams describing its bulk metastable region (i.e., the concentration & temperature induced first order phase transitions) have been plotted already (Muschol et al., 1997; Manno et al., 2003). The heterogeneous crystallization of proteins, though, has been well known since 1987, when McPherson et al. introduced the idea of using mineral substrates to induce protein crystallization. Later, lipid layers were used to enhance the formation of protein crystals (Hemming et al., 1995). Recently, different researchers have experimentally observed that differently charged surfaces, and a variety of silicon (or natural) substrates, enhance the heterogeneous crystallization of some proteins (Fermani et al., 2001; Sanjoh et al., 1999/2001; D'Arcy et al., 2003). Notwithstanding this, the theory understood in the heterogeneous crystallization of proteins is currently poorly understood and the classical homogeneous nucleation theory has been, so far, used to elucidate also heterogeneous nucleation phenomena. More recently, however, local solute concentration fluctuations that form pre-nucleation clusters have been differently described for the supersaturation, or heterogeneously, induced nucleation processes (Lutsko, 2012; Fermani et al., 2013).

Computer modelling, indeed, may better explain the grouping dynamics of protein molecules. In fact, since the aggregation of proteins is initiated by conformationally active molecules its grouping dynamics are statistically determined. That is, these molecules are, not only, subjected to different types of Brownian motion, but also, to conformational motion that may originate unfolding (Chan et al., 1994). The unfolding equilibria, in turn, may play a major role during amorphous aggregation or nucleation (Anfinsen, 1973). Although, conventional bulk nucleation parameters (such as the nucleus critical radius and the nucleation rate) have

been, regularly, reported in the literature, it has been, recently, detailed that, during heterogeneous phenomena, the interface chemical potential and solute molecule conformations play a significant role too. Hence, the heterogeneous dynamics of protein nucleation should be modelled, not only, as a function of the solution parameters (such as the protein diffusion rate), but also, the solid-liquid interface potential energy and its energy of interaction with the solute molecules as well as the solution structured maculae. That is, non-specific solvent-mediated interactions may, indeed, play the major role during both the homogeneous and the heterogeneous clustering of protein molecules.

In practical terms, the possibility to understand the protein heterogeneous dynamics and control their nucleation rate at the solid-liquid interface by engineering catalytic surfaces would be a scientific breakthrough. That is, any advancement in this field would contribute to widening the well-known bottleneck of protein crystallization (Chayen, 2004). In the following thesis a low-salt (and low-solute) lysozyme solution has been formulated and nano-patterned substrates (with different features and different chemistries) have been prepared to identify the effect of the surface features on the lysozyme heterogeneous nucleation rate. Specifically, in this work, the homogeneous nucleation rate of the low-salt (and low-solute) lysozyme solution is 48 hrs only. Moreover, nano-patterned substrates have been fabricated by nano-molding & nano-imprinting, or step & repeat interference, lithography and have been used for crystallization. The nano-molding & nano-imprinting procedure is, usually, performed by transferring a pattern from a silicon mask (with an anti-adhesion layer) onto a PDMS soft stamp (i.e., polydimethylsiloxane). The pattern (which, generally, features periods of size more than 100 nm) is stamped from the soft stamp onto a wafer bearing a layer of spin-coated epoxy-polymer (Viheriälä et al., 2009). The step & repeat interference procedure, instead, is, usually, performed by repeatedly diffracting a patterned area on a surface with spin-coated photoresist. A diffraction grating system and a beam of EUV coherent light (i.e., extreme ultraviolet light) are, generally, used to make vary narrow patterns, that is, EUV exposure can generate features with periods of size less than 100 nm (Solak et al., 2002; Auzelyte et al., 2009).

Chapter 2

The Aggregation of Proteins

2.1 Theory

2.1.1 The classical aggregation theory in comparison to the recent models

Proteins may be regarded as copolymers that are made of units with diverse hydrophilic or hydrophobic properties (amino acids). The chance that copolymers aggregate when these are mixed together with a solvent (such as water) is directly related to the chances of inter-chain interaction among polymeric molecules. The Flory-Huggins solution theory is often used to interpret the results from experiments on the aggregation of polymers, and, recently, it has been also extended to proteins (Sadana A., 1998).

Nevertheless, the above-mentioned mathematical model makes assumptions that neglect the changes in the freedom of the chain conformation upon different conditions. Recently, Fields has described the copolymer solution dynamics with the following general equation (2.1):

$$F = E - T\,(S_{mix} + S_{conf}) \qquad (2.1)$$

where the free energy of the solution (F) results from the contact energy (E), the temperature (T), the translational mixing entropy (S_{mix}) and the conformational entropy (S_{conf}). E in itself is a negative function of the volume fraction of the copolymer in solution (Ψ) and the contact interaction parameter (χ) to the power of the non-polar fraction of the copolymer residues (Φ). If there is little solvent in the solution, the copolymer volume fraction increases (that is, $\Psi \rightarrow 1$) and the contact free energy is lower. Likewise, when the contact interaction parameter (χ), or the number of hydrophobic residues (Φ), is high (i.e., $\chi\Phi^2$ increases), the contact free energy becomes more negative. That is, the specific grouping patterns are contemporarily defined

by the contact interaction parameter (χ), the number of hydrophobic residues (Φ) and the copolymer chain length. Though, this seems easier to observe whenever the volume fraction of the polymer in the solution increases (Fields, 1992). Also, it is shown in Fig 2.1 that, according to the above model, the clustering process has an initial lag time, during which no detectable aggregation occurs, and a following maximum, at which the copolymer straightforwardly converts into an aggregate. That is, there is a critical point, which occurs at fairly low copolymer volume fractions (Ψ), where the change of one amino acid in the protein can cause the protein to cluster. Finally, a clear correlation is, also, observable between the aggregation rate and the above-mentioned lag time. The latter, in fact, would be inversely proportional to the copolymer chain length.

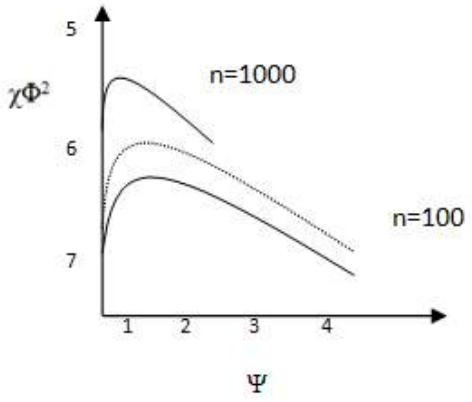


Fig. 2.1 *The phase diagram of copolymers with 100 and 1000 constituting units: 1 phase above the curve and 2 phases below it. The polymer with n = 100 is represented by both the Fields Gregg theory (continuous line) and the Flory-Huggins theory (dotted line).*

Furthermore, protein molecules may be regarded as monomers that aggregate via polymerization reactions and their clustering dynamics may be regarded as the combination of different types of polymerization reactions (Li Y. et al., 2009). These reactions may, indeed, occur contemporarily, or, depending on the solution conditions, one, or more, of these reactions may be kinetically favoured over all the others. That is, different solution factors (such as the solvent type, protein, or co-solute, type and concentration as well as pH) may contemporarily, or at turns, govern the overall polymerization process. The above representation of the protein aggregation process may also explain the broad range of clustering dynamics it originates from. Proteins, indeed, may immediately collapse into oligomeric intermediates that adjust into

clusters, or conformationally convert into a partially mis-folded molecule. When an aggregation process stems from a rapid collapse of copolymer molecules via a clear equilibrium, the specific pathway followed is not important to define the features of the final cluster. Conversely, when irreversible, or partially reversible monomeric interactions occur, one favoured pathway of polymerization, or highly interconnected parallel pathways, may govern the overall aggregation process. That is, the dynamics of the pathway, or pathways, that leads to the formation of the clustered state, may, also, clarify the forces, and parameters, that govern the evolution of the entire clustering process. Kelly (2000), indeed, has modeled four possible pathways that lead to the formation of protein clusters:

1. The collision of two monomers induces misfolding and, therefore, clustering;
2. A thermodynamically unstable monomer starts an addition polymerization;
3. A templated grouping, in which monomers add onto a pre-existing cluster;
4. Monomers collapse into a conformational conversion while clustering.

As previously mentioned, the partially reversible, or irreversible, kinetics of protein clustering may be modeled as a group of simultaneous polymerization reactions, or consecutive steps from different polymerization reactions. Also, it has been said that each of these reactions (or one of their individual steps) may become the rate-determinant step for the whole clustering process. That is, similarly to a polymerization reaction, there would be the degradation of an initiator (such as the misfolding, or partial unfolding, of a protein monomer) that is, then, followed by additional initiation and propagation steps. Indeed, during initiation monomers expose hydrophobic amino acid regions that previously were hidden by the protein tertiary, or quaternary, structure. As hydrophobic forces induce the folding of protein monomers (i.e. molecules), hydrophobic interactions, primarily, might also initiate atypical grouping. That is, non-specific solvent-mediated forces may rule both the aggregation process and the nucleation dynamics. According to the literature, the polymerization equilibria might be represented according to Fig. 2.2. Hence, protein monomers (A_1), may generate degraded monomer species $(A_1)^{\mu}$, with given forward, and backward, "degradation" rates ($+k^{\mu}$ and $-k^{\mu}$ respectively).

Also, these may induce the formation dynamics of critical nuclei (n*) with characteristic formation and disassembly rates ($+k^*$ and $-k^*$ respectively). Finally, after nucleation, A_i oligomers may grow by following a polymerization-like reaction (A_{i+1}) with characteristic growth ($+k_i$) and decomposition ($-k_i$) rates (Arnaudov, 2007).

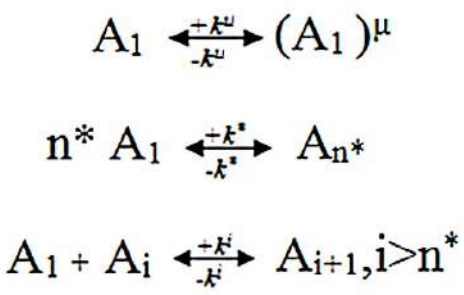


Fig. 2.2 *Where A_1 represents the monomer species, $(A_1)^\mu$ represents the inactivated monomer species, (where $+k^\mu$ and $-k^\mu$ are, respectively, the forward and backward inactivation rate constants); **n*** represents the critical nucleus (where $+k^*$ and $-k^*$ are, respectively, the rate constants for the formation and disassembly of this nucleus); A_i represents the nucleus i-mers and A_{i+1} represents the growing i+1-mers (where $+k^i$, and $-k^i$ are, respectively, the forward and backward rate constants for the following ith growth reaction, (Arnaudov, 2007).*

The medical literature has often reported that the understanding of the thermodynamic stability of proteins and their kinetics of aggregation under physiological conditions are, both, of primary importance in research. Cell proteins, indeed, may form clusters of regular structure, also under physiological conditions, and the understanding of the relating dynamics of formation may reveal the root causes of several protein related diseases. Generally, these diseases are determined by anomalous protein interactions that, ultimately, may result in highly regular structures (such as fibrils).

Ricchiuto et al. (2012) have modeled the solubility of the oligomeric and fibrillar phases of natively folded α-helical, and β-sheet, forming peptides. The model in Fig. 2.3 features protein disordered (*DOS*) and native (*NOS*) oligomer phases, in equilibrium with the peptide solution or its fibrillar phase. That is, while the *DOS* phase is made of fully (or partially) folded and unfolded peptides, the *NOS* phase is made of native oligomers. Also, the peptide folding temperature is represented by a dotted line (in T_f), while the red open (and red filled) circles indicate the points at which aggregation has not (or has) been observed. Moreover, aggregation parameters that detail the related clustering scenario have been defined by Ricchiuto et al. and some of these are well described in Fig. 2.4.

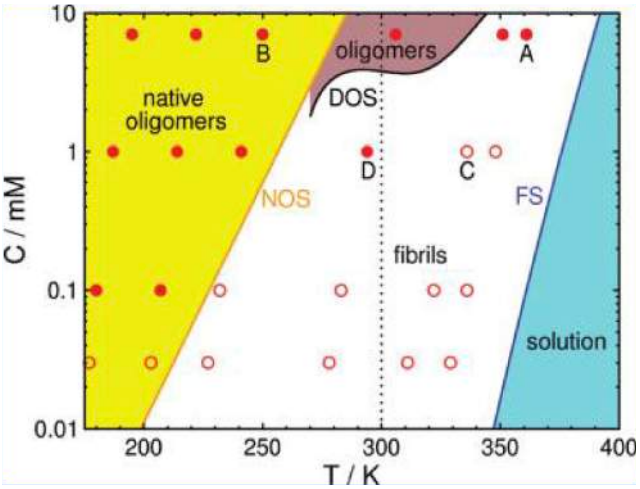


Fig. 2.3 *The phase behaviour of proteins: where C/cm is the millimolar concentration of the protein and T/K is the temperature in Kelvin. FS represents the fibrillar phase in equilibrium with the solution. DOS represents the disordered oligomer phase in equilibrium with the native oligomer phase (that is, the DOS phase is made of fully folded, partially folded, and unfolded peptides) and NOS represents the ordered native oligomer phase in equilibrium with the solution (that is, the NOS phase is made of fully folded α-helical peptides). The simulation shows a dotted black line, which represents T_f, i.e., the peptide folding temperature. The red open circles indicate the points at which no aggregation has been observed, and the red filled circles indicate the points at which aggregation has been observed. At point A, the protein solution is supersaturated with respect to the fibrillar phase only. At point B, the protein solution is supersaturated with respect to both the oligomeric and fibrillar phases, (Ricchiuto et al., 2012).*

That is, the effect of the temperature decrease, and peptide concentration, on the peptide cluster size or composition is shown in this figure. Specifically, in Fig. 2.4 (a) the temperature dependence of the oligomer average number ⟨N⟩, and the average size ⟨n⟩ of the largest oligomer (i.e., the numbers by the curve), is represented. Furthermore, Fig. 2.4 (b) shows that the oligomers have a very short average formation time at higher concentrations and lower temperatures. In addition Fig. 2.4 (c) represents the analysis of the largest oligomer structure. That is, the β-sheet content increases with temperature, while a milder, but inverted, effect is observable for the α-helical content. Finally, Fig. 2.4 (d) explains that when the larger oligomers form at low temperatures the protein concentration left in solution decreases.

It may be, therefore, inferred that different concentration and temperature values favour different ordered structures within the prenucleation cluster and, possibly, initiate different morphologies. Therefore, simulations, that are comparable to the above-mentioned model, might be designed to approximately define, not only, the temperature (or concentration) related parameters, but also, the specific dynamics that locally govern the structuring of the protein oligomers. This would, also, give a major contribution to explaining the types of anomalous interactions that induce protein pathologic structures, and, ultimately, the root causes of the related diseases. Also, the dynamics of aggregation, or nucleation, would be further discerned in relation to this.

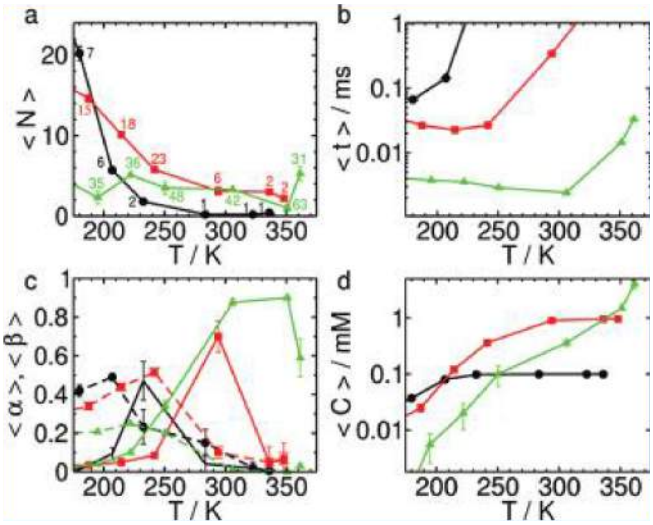


Fig. 2.4 *The effects of the temperature decrease on the thermodynamics, and the kinetics, of the peptide aggregation have been simulated. Specifically the above simulation has been run at a lag time of 0.47 ms (t = 0.47 ms) and at different concentrations (C = 7 mM, green ▲, C = 1 mM, red ■ and C = 0.1 mM, black ●), after instant cooling from T (390 K) to T_s (361, 351, 306, 251, 222, 195 K).* ***(a)*** *Shows ⟨N⟩ the average total number of oligomers in solution and the numbers by the plot symbols that represent ⟨n⟩, i.e., the average size of the largest oligomer in solution;* ***(b)*** *Shows the average time t to form an oligomer of size 10 at 2 different concentrations (C = 7 mM and C = 1 mM), and of size 5 (at C = 0.1 mM);* ***(c)*** *Shows the α-helical content (dashed line) and the β-sheet content (solid line) for the largest oligomer in solution;* ***(d)*** *Shows the concentration that is left in solution, (Ricchiuto et al., 2012).*

Additionally, according to Bemporad (2012), there is a monomer native-like state that is only slightly more expanded than the fully native state. The native-like state, by Bemporad, does not present unfolding, while it has large enough conformational fluctuations to enable specific interactions. It has been mentioned already, that the simulation of the monomer clustering dynamics might provide information about the oligomer exact structuring (as well as size) and, possibly, the specific fluctuations that induce grouping. That is, modelling the exact pathways that originate the oligomer may, also, reveal how its regular structure is progressively configuring. Also it may reveal how the solution environmental factors, other than the intrinsic properties of the grouping molecules, induce and, govern, the formation of the above structure. Since modelling the cluster intrinsic structure may notably contribute to drawing better conclusions on the root causes of protein related disease, at present, the study of protein clustering dynamics has become a major subject of interest. The research in this field, so far, has been, mainly, about defining the local folding, or assembly, under physiological conditions and the structural density variations of regularly assembled clusters, (Ferguson et al., 2003). Cohen et al. have, in fact, plotted against time, the experimental effect of the protein nominal concentration on the formation of fibrils, which is shown in Fig. 2.5. As expected, it shows that the fibril mass fraction forms faster once the protein nominal concentration has been increased. That is, apparently, the oligomer structuring depends on nominally controllable factors.

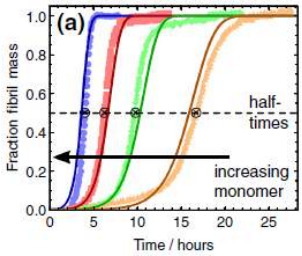


Fig. 2.5 *The time-dependent formation of the fraction fibril mass is plotted against time while increasing the initial monomer concentration, (Cohen et al., 2012).*

Nevertheless, highly entangled factors that characterize the crystallizing solution may, often, induce non-controllable primary, and secondary, structuring dynamics, the relative importance of which might even become time dependent.

At the beginning of this chapter, it has been mentioned that the concentration of hydrophobic residues would play a major role in the formation of protein clusters (i.e., Fields Gregg theory). Also, later on, it has been inferred that during initiation monomers expose hydrophobic amino acid regions that previously were hidden and that hydrophobic interactions, primarily, might favour monomer grouping by means of non-specific solvent-mediated forces. As a result of this, a crucial role may be inferred for the arginine residues during the formation of protein spatial ensembles. It has been observed in the literature, already, that arginine residues increase the protein solubility (Hamada et al., 2009). That is, very probably, the influence of the nominal protein concentration onto the molecular clustering, or structuring, dynamics, is primarily shaped by the overall solution amino-acidic (and co-solute) composition. This would also mean that the aggregation process is strongly constrained by the solvent type as well as its locally structured polarizability. Hence, determining and controlling the above-mentioned clustering dynamics might become straightforward once the associated solvent dynamics had been clarified. It has been, mentioned, indeed, that the protein monomers cluster differently as a result of the different local solution dynamics (Etzkorn et al., 2011). Almost certainly, these dynamics are driven also by water-mediated interactions that evolve with respect to time and define the pathway, or the single step, that governs the local clustering (or restructuring) reaction rate. Klimov et al. (2003) have, indeed, simulated the water expulsion that precedes clustering and have concluded that this event may trigger the formation of ordered structures. Though, in the same simulation it has been also concluded that this

expulsion should not be the rate-limiting step of the whole aggregation process.

Furthermore, the consistency of the aggregation process might change also in relation to the protein conformational stability. Proteins may be intrinsically unfolded, or globular, and these may aggregate both in vitro and in vivo. Intrinsically unfolded proteins cluster promptly, while globular proteins have more stable a structure. Indeed, although some globular proteins start clustering while exposing their physiologically active site (Masino et al., 2010), external perturbations may well induce the indistinctive clustering, also, of globular proteins (Tomaselli et al., 2006; Adrover et al., 2010). The activation of a globular protein to amorphous aggregation, or structured clustering, is often called misfolding. It is, in fact, after misfolding and clustering, that each local protein solution ensemble reaches its energy minimum. This would, also, induce conformational energy minima within all the different dimensions of the protein solute (Guo et al., 1995; Scheraga, 1996). That is, the various combinations of the conformational energy minima of the protein (and the structured solvent/co-solute maculae) lead to the formation of stable clusters with different morphologies. These morphologies may involve the formation of repeating β strands or other regular structures that (after domain-swapping or end-to-end stacking) differently rearrange along the main axis of the protein cluster (Bennett et al. 2006; Nelson et al., 2006).

2.1.2 Aggregation vs. crystallization

Although it seems, now, inferable that each of the local conformational energy minima has been fully reached after clustering, the conformational energy minimum for each parallel polymerization pathway would be reached at different stages of the overall clustering process. This means that, almost certainly, there is a landscape of very diverse (and time-dependent) energy levels (i.e., conformational, or configurational, arrangements) that may, locally, combine to form a well-defined cluster. Indeed, it has been often observed in the literature that the amorphous aggregates form once their local energy minima have been

reached. Nevertheless, when all the local energy minima are close enough to a certain value, crystallization may occur instead (Tessier et al., 2003; Velev et al., 1998; Curtis et al., 1998; George et al., 1997; Narayanan et al., 2003).

Different solution factors may, therefore, play a major role during protein nucleation, especially. Indeed, the solution properties can be tuned to induce a certain degree of detachment from the aggregation energy minima, and, therefore, to trigger nucleation. The solution second virial coefficient (B_{22}) is a good indication of what type of structure is going to form (that is, either an amorphous aggregate or a crystal). The second virial coefficient accounts, not only, for the solution electrostatic and density factors, but also, for the steric anisotropy properties of the protein molecules. Specifically, dilute lysozyme solutions show a positive B_{22} when the sodium chloride concentration (NaCl) is equal to 0.05 M but B_{22} decreases when the sodium chloride concentrations are greater than 0.05 M. While it becomes negative and crystallization occurs at sodium chloride concentrations greater than 0.2 M. However, there is no more crystallization when the sodium chloride concentration reaches 1.75 M. Another parameter, which is closely related to $B_{22,}$ is the mutual diffusion coefficient (D_m). The mutual diffusion of proteins is slowed by monomers' attraction, while it is enhanced by their repulsion. Both the B_{22} and D_m have been correlated in the following equation:

$$\frac{D_m}{D_s} = 1 + \left(2B_{22} - \upsilon_{sp}\right)c \qquad (2.2)$$

where D_m is the mutual-diffusion coefficient, D_s is the self-diffusion coefficient, B_{22} is the second virial coefficient, υ_{sp} is the specific volume of the solute (which, for lysozyme, is 50.7 ml/g) and c is the local concentration. That is, the mutual-diffusion coefficient D_m is directly proportional to both the second virial coefficient B_{22} and the copolymer local concentration (Zhang J. et al., 2003). Also, in the above equation, the mutual diffusion coefficient is related to the self-diffusion coefficient D_s and these both are linear functions of the local copolymer concentration. While the self-diffusion of each molecule is an entropy-driven parameter, their mutual diffusion is closely associated with the solvent-mediated solute–solute interactions.

Therefore, differently from D_s, the local D_m may be regarded as an order degree indicator of each infinitesimal local solution. The nominal D_m may be, also, experimentally determined by measuring the protein post electrophoresis relaxation (PER), (Young et al., 1982).

Nevertheless, nucleation, or crystal growth (which is primarily determined by surface molecular incorporation dynamics), occurs only when the protein molecules have appropriate orientations and conformations (i.e., suitable relative configurations). That is, protein molecules couple while defining closely related energy minima that may be, also, expressed by means of D_m values. Indeed, depending on their mutually determined (or co-solute/solvent mediated) orientational freedom protein monomers have higher or lower chance to keep their relative configurations, and, therefore, higher or lower chance to form local amorphous aggregates. For low orientational freedom values (as well as long relaxation times), monomers do not have enough time to reach the suitable relative configuration before arranging contacts with the aggregating (or aggregated) molecules. That is, the formation of a bulk amorphous phase is entropically favoured over that of ordered protein crystals (Teraoka, 2002).

It has been previously mentioned that protein monomers have been observed to cluster differently depending on the different solution ionic concentrations and that this is often parameterized by means of the D_m and B_{22} variables. More specifically, in the case of lysozyme, when B_{22} is positive, that is, when the sodium chloride concentration is equal to 0.05 M, D_m increases with the lysozyme concentration. While when B_{22} is negative, that is, when the sodium chloride concentration is equal to 0.5, 1.0, 1.5, or 2.0 M, D_m decreases with the lysozyme concentration. As a result of this, solution conditions such as the pH or ionic strength may be regarded as the major environmental factors that drive clustering. It seems that the main reason for this response is primarily related to the protein isoelectric point. Indeed, protein monomers carry a net positive charge at pH values that are below their isoelectric point, while these carry a net negative charge at pH values that are above it. Nevertheless, the net charge of each protein monomer results from the average of all its charges. These charges, in fact,

change in number, identity and location depending on the protein type (or conformation), and the solution concentration, pH or ionic strength values. That is, very probably, protein intermolecular interaction dynamics (and, therefore, D_m values) are primarily governed by their surface charges. In practice, most proteins have an isoelectric point that is between 5 and 8.5, that is, almost all proteins are negatively charged at a neutral pH. That is, the solution pH might be set within the above range to perform protein salting out, since the isoelectric point is also the pH at which the lowest protein solubility occurs (Scopes, 1982).

Nevertheless, with respect to this, it is worth mentioning also the Hofmeister series. According to Hofmeister, indeed, proteins respond differently to the type of salt and solution ionic strength depending on the solution pH. Salts, in solution, induce hydration changes and reduce protein solubility. It is now well known that this is because of the ability of these salts to affect the stability of the protein molecules, while coordinating the solvent molecules. As the salt anions seem to have a larger effect than cations, the anions only will be referred to in the following paragraphs. Specifically, when the solution pH is above the protein isoelectric point, the net charge of its molecules is negative a direct Hofmeister order applies. That is, the salt anions and the protein monomers compete for the solvent molecules. Indeed, since kosmotropes (such as SO_4^{-2} and F^-) structure more solvent molecules, these cause a salting-out effect, while chaotropes (such as I^-, ClO_4^-, SCN^-) keep protein molecules in solution. An inverse order applies instead, when the net charge of the monomers becomes positive, as the solution pH is below the protein isolectric point (Finet et al., 2004; Boström et al., 2005).

Specifically for lysozyme, (which has a ≈11.35 isoelectric point) an inverse Hofmeister order often applies as its monomers are generally suspended in a solution with a pH that is below its isoelectric point. The phase transition temperature behaviour of lysozyme is, though, quite complex. The phase transition temperature of lysozyme in the presence of some chaotropes rises at lower salt concentrations, while it decreases at higher salt concentrations. That is, it follows the inverse Hofmeister order only at quite low salt concentrations, while it follows a direct Hofmeister order as the salt concentration is increased. Furthermore, the phase-

transition behaviour of lysozyme in sodium chloride solutions is still different from the above-mentioned behaviour. Indeed, in this instance, the phase transition temperature rises sharply at low salt concentrations (and salting out is enhanced), but, at higher salt concentrations, it continues to rise. The above lysozyme dynamics have been also described for sodium chloride (NaCl) solutions by means of the relevant solution parameters (that is, B_{22} and D_m). It has been, in fact, observed that when B_{22} is positive (i.e., when the NaCl concentration is equal to 0.05 M) D_m increases with the lysozyme concentration (as there is little intermonomeric attraction). Nevertheless, when B_{22} is negative (that is, when the NaCl concentration is equal to 0.5, 1.0, 1.5, or 2.0 M) D_m decreases with the lysozyme concentration (as there is higher intermonomeric attraction). At even higher NaCl concentrations, and more negative B_{22} values, D_m decreases faster, (Lima et al., 2007).

It may be, therefore, inferred that at low ionic strength values the clustering dynamics of the protein monomers would be, primarily, related to the co-solute anion size, the hydration layers and their polarizability (which, in turn, are related to B_{22}). It has been, in fact, previously mentioned that according to Hamada et al. the presence of arginine residues in a protein copolymer increases its solubility. L-arginine is one of the most common natural amino acids and each lysozyme monomer contains 11 arginine residues. Arginine, is also called 2-amino-5-guanidinopentanoic acid and its structure is represented in Fig 2.6. The physicochemical characteristics of this amino acid are quite peculiar, as it has a high pKa (i.e., 12.48). That is, it is positively charged at the habitual solution pH values.

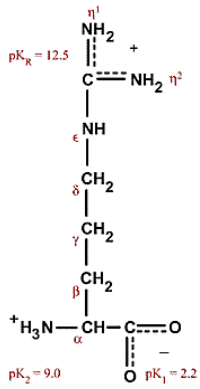


Fig. 2.6 *2-Amino-5-guanidinopentanoic acid, (arginine).*

This amino acid was first isolated in 1886. However, the ability of arginine to improve the refolding of proteins, as a solution additive, was discovered only twenty years ago and since then it has been object of many studies (Arakawa et al., 2007).

L-Arginine hydrochloride, especially, has been regularly used as an aggregation suppressor. That is, not only, this salt prevents intermonomeric interactions, but also, it does it without perturbing the conformational stability of each protein molecule. At present, researchers have only tried to investigate the reasons why this molecule is able to inhibit protein aggregation. As previously discussed the misfolding of a protein molecule is the major monomer activation event that triggers clustering reactions and the l-arginine hydrochloride must hinder this polymerization activation mechanism. Although its electronic characteristics are typical of most amino acids, very probably, the unique structure of arginine permits a sterically changeable polarizability for this residue. Indeed, as a result of its guanidine group, aside from the field, and Charton, electronic effect, the polarizability (i.e., steric) effect would be, especially, enhanced. It is worth noting, here, that, although the l-arginine chloride salt is the one that is predominantly used in medical formulations, different l-arginine salts are, nowadays, available. That is to say, given that the chlorine anion is approximately in the middle of the Hofmeister series, with respect to the clustering suppression properties of the l-arginine salts, the arginine cation might, primarily, determine the above stabilization.

Due to the intermonomeric interactions, a protein in an aqueous solution constitutes a colloidal solution with molecules that might straightforwardly cluster according to the picture in Fig. 2.7. That is, ideally, colloidal interactions are tunable by, only, changing solution environmental factors such as the pH or ionic strength (Frenkel, 2002).

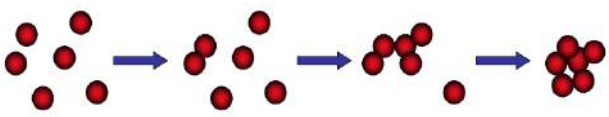


Fig. 2.7 *A simple representation of the colloidal aggregation process.*

Nevertheless, there are different theoretical laws that have been used to define the interaction among colloidal particles, so far, the Derjagin-Landau & Verwey-Overbeek theory (i.e., the DLVO theory) has been the most widely reported. This theory (or its extended version) defines a trend describing the inter-particle potential energy of interaction and it is conventionally plotted according to the sketch in Fig. 2.8. However, protein solution dynamics are more complicated than traditional colloidal solutions', and, apart from the novel aggregation models, a comprehensive theory that describes the colloidal interactions of protein solutions during aggregation is, currently, missing (Lomakin et al., 2003). Protein monomers, indeed, are made of various units with differently ionizable groups that are randomly distributed on their surfaces and, depending on the solution pH and ionic strength, dissociate differently.

Boström et al. (2006) have detailed the extended version of the DLVO theory with experimental data. It has been, indeed, observed that the traditional theory, does not fully apply to proteins, as it does not take into account hydrophobic or hydrogen-bonding effects.

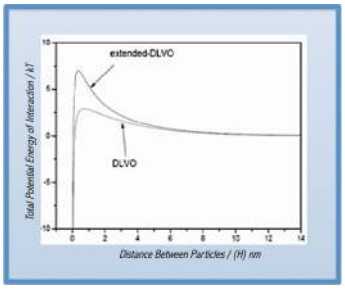


Fig. 2.8 *The DLVO theory claims that the interaction between 2 particles (or a particle and a solid surface) in the presence of electrolytes depends on the combination of the Coulombic repulsive forces (V_R) and Van der Waals attractive forces (V_A), (Boström et al. 2006).*

Conventionally, this theory defines the interaction between particles (or a particle and a surface) in presence of electrolytes by combining the 2.3 equations:

$$V_R = \frac{64\pi r_p n_0 \kappa_B T}{\kappa^2}\gamma^2 e^{-\kappa d} \;\; ; \;\; V_A = -\frac{A}{48\pi(d/2)^2} \;\; ; \;\; V_A = -\frac{2A\, r_p}{12(z_0)^2} \qquad (2.3)$$

where V_R defines the Coulombic repulsive forces and V_A the Van der Waals attractive forces, A is the Hamaker constant, r_p is the particle radius, d is the distance between the two particles, z_o is the separation distance between the interface and the particle, n_0 is the number of ions,

$1/\kappa$ is the Debye−Huckel screening length, γ is a parameter proportional to the Debye−Huckel surface potential (ψ) and T is the absolute temperature. Very probably, in the specific case of protein monomers, a gradient of different hydrogen-bonding bridges form between the ions of the solution electrolyte and the superficial monomer residues that, indeed, feature different degrees of polarity. The latter would induce a different detachment of the counter-ions from the different infinitesimal surface sections of the monomer outer surface. The surface-associated counter-ions and all the other ions generate a gradient of Coulomb-screened Debye-Huckel potential and osmotic interactions among the conformational active protein molecules (i.e., monomers). Non-electrostatic forces (NES forces) may this way initiate additional interaction dynamics and generate the extended version of this theory, (Boström et al. 2006). The traditional DLVO theory, indeed, reproduces only a qualitative description of the protein intermolecular interactions at low solution ionic strengths, while this theory may provide a more quantitative description of these interactions only at higher solution ionic strengths. Specifically, the DLVO theory is able describe the lysozyme monomer interactions only qualitatively when the solution ionic strength is less or equal to 0.102 M, and the experimental scattering intensity is predictable only if the distances are less or equal to a couple of lysozyme diameters. On the other hand, when the solution ionic strength is equal to 0.124 M (that is, when the solution ionic strength is sufficiently high), and the NES forces are hidden, the DLVO theory correctly predicts the experimental light scattering data (Pellicane, 2012).

2.2 Applications

Over the past few years, protein misfolding and aggregation phenomena have, progressively, become a subject of interest to scientists. Apart from the new findings on protein related degenerative diseases, the increasing number of therapeutic proteins has instigated researchers' interest in the characterization of protein aggregates. Nowadays, protein aggregation is a major issue in both pharmaceutical and biotechnology companies, as

aggregation may take place during both the formulation and the storage stages of protein production. This becomes a troublesome issue, especially, during the production of protein-based therapeutics. Indeed, the main issue, relating to the production of protein therapeutics, is that during the biopharmaceutical manufacture processes proteins are often exposed to a wide range of mechanical, and chemical, stresses, and these stresses may well trigger the misfolding and aggregation. That is to say, undesired aggregation, in this specific instance, reduces the production yield, and, very probably, may cause additional problems during the downstream purification processes. Furthermore, protein aggregates in therapeutic products may also become biologically active and induce immunological response or other side effects (once these had been administered to patients). Consequently, over the last twenty years there has been an exponentially growing interest in the development of new methods to prevent protein aggregation (Leader et al., 2008). As previously stated, the use of aggregation suppressing additives (such as l-arginine hydrochloride) has become a regular practice during the formulation, and the production, of protein therapeutics in order to counteract the above-mentioned issue. Though, for this same purpose, also the solution pH and ionic strength may be tuned, when this is possible, to meet the therapeutic and production requirements.

The first therapeutic protein (human insulin) was introduced over 85 years ago and, nowadays, there are several proteins that are used as therapeutics. Therapeutic proteins may be arranged by different categories, according to their pharmacological action especially. Indeed, the American food and drug administration (FDA) has categorized the therapeutic proteins in four groups: group I and group II (that list all the protein-based therapies), and groups III and IV (that list examples of proteins that are used in vaccines or diagnostic agents). Therefore, group I includes therapeutic proteins having enzymatic or regulatory activities (that is, proteins that replace a protein that is deficient or abnormal, proteins that enhance existing pathways and proteins that provide a novel function). Secondly, group II includes therapeutics with targeting activities (that is, proteins that intercept and interfere with molecules or organisms, and proteins that transport compounds or other proteins). Group III includes protein vaccines (that is,

proteins that act against detrimental external agents, proteins that treat autoimmune diseases and proteins that treat cancer). Finally group IV includes all the in vitro and in vivo protein diagnostics (that is, proteins that are used either in vivo, or in vitro, to diagnose diseases or pathological and physiological conditions). Examples from each of these therapeutic groups are shown below (http://www.fda.gov/):

From Group I:

- Insulin: that is used to treat diabetes mellitus.
- Protein C: that is used for the treatment of venous thrombosis and purpura fulminans (that is, patients with hereditary protein c deficiency).
- Erythropoietin: that is used mainly to treat the anaemia of chronic diseases, myleodysplasia and the anaemia due to renal failure or chemotherapy.
- Salmon Calcitonin: that is used to treat postmenopausal ostheoporosis.
- Bivalirudin: that is used to reduce the risk of blood clotting in coronary angioplasty and heparin-induced thrombocytopenia.

From Group II:

- Pegvisomant: that is used to treat acromegaly.
- Digoxin immune: serum Fab that is used to protect from digoxin toxicity.
- Palivizumab: that is used to prevent (in high-risk paediatric patients) respiratory syncytial virus infection.
- Denileukin diftitox: that is used to treat the cutaneous T-cell lymphoma with malignant cells (which express the cD25 component of the iL2 receptor).

From Group III:

- Hepatitis B surface antigen: that is used to formulate the hepatitis B vaccination.
- HPV protein: that is used as a vaccine against HPV infection.
- OspA protein: that is used as a vaccine against the Lyme's disease.

From Group IV:

- Recombinant purified protein derivative: that is used for the diagnosis of tuberculosis (in vivo).
- Secretin: that stimulates pancreatic secretions or gastrin and it is used to diagnose the pancreatic exocrine dysfunction, or gastrinoma, and to help other diagnoses such as that of the ampulla of Vater (in vivo).
- HIV antigens: that are used to diagnose the HIV infection (in vitro).

- Hepatitis C antigens: that are used to diagnose any exposure to the hepatitis C virus (in vitro).

Preventing the formation of potentially hazardous aggregates during the prolonged storage of protein therapeutics is crucial for their production. Indeed, the characterization of the time related aggregation dynamics is indispensable to estimate the expiry date and the shelf life of therapeutic protein products. Furthermore, also the characterization of the protein adsorption dynamics at interfaces (such as the medicine container) and their aggregation together with inorganic impurities, or other extraneous proteins, is of primary importance to safely estimate the shelf life of therapeutic proteins. Indeed, different types of aggregates with different degree of hazard rating may form during storage, since aggregates may be soluble or insoluble. Soluble aggregates are dimers, small oligomers, or higher molecular weight aggregates, while insoluble aggregates are usually denoted as precipitates or particulates (Webb et al., 2002).

In vivo protein aggregates are also subject of intense research, as these cause neurodegenerative diseases. The Alzheimer disease for example is a neurodegenerative disease, which involves the amyloid peptide and the tau protein. These form extracellular amyloid plaques and hyperphosphorylated-aggregates of the neuronal microtubule-associated protein tau. Also, the transmissible spongiform encephalopathy, or prion disease, occurs as the prion protein evolves from a physiological form into a pathogenic aggregating infectious form (Gilch et al., 2001; Aguzzi et al., 2010). Similarly, the Parkinson disease is caused by inclusions containing α-Synuclein (Kahle, 2008). Also, polyglutamine proteins are associated to several diseases such as the hereditary neurodegenerative disorders, Huntington's disease, spinocerebellar ataxia, dentatorubral-pallidoluysian atrophy, bulbar muscular atrophy, familial amyloid polyneuropathy and senile (heart) systemic amyloidosis (Tanskanen et al., 2008). Moreover, dialysis-related amyloidosis is caused by β2-microglobulin. The latter, in fact, forms amyloid deposits in the osteo-articular tissues of long-term dialysis patients. That is, its blood concentration increases after catabolising in the proximal kidney tubules of the patients, who are affected by renal dysfunction, and triggers the formation of osteo-articular deposits (Otsubo

et al., 2009). Finally, the type II diabetes is induced by amylin aggregates. This is a hormone peptide and it is secreted, after transformation from a precursor protein, by the cells in the pancreatic islets of Langerhans. Following this transformation pathologic amyloid aggregates are formed in the pancreatic cells (Westermark et al., 2011).

2.3 Techniques for Detecting and Measuring Aggregation

As previously stated, although therapeutic proteins are often diluted in physiological solutions before administration, protein aggregation may, indeed, affect both the safety and efficacy of therapeutic protein formulations. As a result of this, different techniques, or methods, are commonly used to detect, and measure, the protein aggregate content in therapeutic formulations. Different applications, such as clinical characterization as well as scientific research, may necessitate more sensitive methods in order to detect, or measure, protein aggregation according to the required standards. The techniques for detecting or measuring aggregation may be, broadly, grouped into two different categories: conventional techniques and recent techniques. Examples from each category have been listed here below.

Some conventional techniques are:

1. Light scattering,
2. The measurement of the sedimentation velocity,
3. Filtration followed by SDS–PAGE or western blotting,
4. Size exclusion/gel permeation chromatography (SEC/GPC).

Also some more recent techniques are:

1. Asymmetrical field-flow fractionation (FFF),
2. Fluorescence spectroscopy and fluorescence microscopy,
3. Transmission electron microscopy (TEM) and atomic force microscopy (AFM).

Dynamic light scattering (DLS)

Dynamic light scattering (DLS), which is also called photon correlation spectroscopy (PCS), is an experimental technique that is widely used in scientific research and industry. This technique was initially called quasi-elastic light scattering (QELS) because photons are elastically scattered by particles that are subjected to Brownian motion. Light-scattering techniques are widely used to study the properties of colloids and solutions of macromolecules, polymers, or microorganisms. This is a non-destructive technique and therefore it is extremely suitable for testing protein solutions. During DLS a monochromatic light beam passes through the solution containing the particles, or molecules, that are in Brownian motion. The Brownian motion describes the movement of particles in a solution as a result of the bombardment by the other solvent, or co-solute, molecules. A change in the wavelength of the entering monochromatic light (which is usually generated either by a He–Ne laser source, $\lambda = 632.8$ nm, or an Nd Yag laser source, $\lambda = 532$ nm) occurs as a result of the above-mentioned molecular motion. Indeed, the properties of the scattered light depend also on the wavelength and the frequency of the light before being scattered. Nevertheless, the wavelength shift, which is characteristic of the scattered light, is primarily proportional the particle mobility, that is, also the Brownian motion. As the particle motion, in itself, is also proportional to the particle size, the latter may be, thereafter, calculated. Indeed, the shift in wavelength, which is measured after that the light beam enters a solution at a specific angle, may give detailed information on the hydrodynamic radius of the suspended particles (the Malvern manual on http://www.malvern.com).

According to the classical theory of light scattering, an incident electromagnetic field exerts a force on the solution molecular charges that after acceleration radiate light. Each sub-region will scatter light differently at different dielectric constants. According to Einstein (1910), light scattering results from local fluctuations of the dielectric constants in the different solution sub-regions. Indeed, different molecules translate and rotate differently, as a result of the externally imparted kinetic energy and intrinsic (or environmentally controlled) mobility.

Sedimentation velocity method

The sedimentation velocity method, also called analytical ultracentrifugation method (AUC), measures the rate at which molecules move upon centrifugation. The sedimentation rate is proportional to a number of parameters, which include the mass, shape and density of the molecules, the liquid density and viscosity, and the gravitational acceleration. During sedimentation a sample is subjected to a very high centrifugal force that rapidly moves the protein molecules away from the centre towards the lower portion of the solution (that is, away from the air-solution interface). Sedimentation via-ultracentrifugation experiments may last up to 6 hrs and the sample volume that is necessary to run this type of experiments may go down to 0.45 ml at a protein concentration of 0.1 – 1 mg/ml. That is, the protein concentration may range from 10 μg up to 40 mg/ml, though usually the concentration is set around 2 mg/ml or below. Furthermore, this technique allows testing over a wide range of pH or ionic strength values and temperatures, (http://www.ap-lab.com/).

Filtration followed by SDS–PAGE or western blotting

The characterization of protein monomer size, usually, follows their extraction from a media (via SDS/Urea, TCA-precipitation, or sonication methods) and their filtration.
The SDS (sodium dodecyl sulphate) polyacrylamide gel electrophoresis is often used to separate the filtered proteins according to the length of their polypeptide chain and charge (that is, their electrophoretic mobility). The sample is treated with an anionic detergent (SDS), or heated, to denature the secondary and tertiary structure of the protein (that is, without breaking its disulfide links). A negative charge is applied to the proteins that move at different speeds as a result of their different charges and molecular weights. After gel electrophoresis the proteins are transferred to a nitrocellulose or polyvinylidene-di-fluoride membrane and stained with antibodies specific to the each target protein. The latter step is called western blotting (http://www.ruf.rice.edu/~bioslabs/studies/sds-page/gellab2.html and http://www.lifetechnologies.com/uk/en/home/technical-resources.html).

Size exclusion/gel permeation chromatography (SEC/GPC)

Size exclusion/gel permeation chromatography (SEC/GPC) is used to separate proteins according to their size or charge. The proteins flow through a porous bed in a chromatographic column and are eluted at different times. Also a detector, which may be placed at the end of the column, records the signals related to the concentrations of the different elutes.

Asymmetrical flow field-flow fractionation (FFF)

This is a high-resolution separation technique. The equipment of this technique consists of two plates that are separated by a spacer with a thickness of ≈ 100 − 500 μm. There is an impermeable upper plate and a permeable bottom plate (which is provided with channels). The bottom plate is also covered with an ultra-filtration 10 kDa membrane, which prevents the sample from penetrating the channels. The separation process follows three stages: injection, focusing and elution. As a result of the laminar flow, the liquid moves slower when this is closer to the plates and faster when this is at the centre of the spacer. The Brownian motion, however, counteracts the motion of those proteins that are driven towards the bottom plate. That is, smaller particles, because of their higher diffusion rates, tend to reach an equilibrium position in the middle of the spacer, and, therefore, flow faster. As a result of this, the smaller particles are eluted (and, therefore, detected) before the larger particles (http://www.postnova.com/).

Fluorescence spectroscopy and fluorescence microscopy

Fluorescence spectroscopy, fluorometry or spectrofluorometry, is an electromagnetic spectroscopy that analyzes fluorescence from a protein solution using a beam of ultraviolet light. The light beam causes certain protein amino acids to emit light of a specific wavelength, which is, thereafter, measured with a fluorometer. There are three amino acids with intrinsic fluorescence properties, phenylalanine (Phe), tyrosine (Tyr) and tryptophan (Trp). However,

only the photon ratios (emitted/exited photons) of Tyr and Trp give fluorescence signals that are experimentally detectable (and, therefore, useful). That is, this technique cannot be used if the protein does not present either Trp or Tyr, or both residues. As a 280 nm wavelength beam excites both Trp and Tyr residues, while a 295 nm wavelength beam excites Trp residues only, the 280 nm peak should be, mainly, regarded for this type of measurements. The above-mentioned residues may, also, be used to detect the protein folded state, as the residue response to fluorescence changes when their environment changes (that is, when molecules fold, or unfold). Indeed, as Trp and Tyr are hydrophobic amino acids, their residues are usually placed inside the protein tertiary structure. That is, the protein fluorescence properties change when the monomers refold or unfold as a result of their exposure to the different solution conditions (http://www.biophys.phys.uri.edu & http://www.microscopyu.com/articles/fluorescence/).

Transmission electron microscopy (TEM) and atomic force microscopy (AFM)

The TEM technique (i.e., transmission electron microscopy) consists of an electron beam that is directed towards a sample. The electrons pass through the sample. The exiting beam is, thereafter, recorded by means of an imaging device, which may be of different nature (a fluorescent, photographic or charge-coupled device). TEM has a resolution that is much higher than usual light microscopy's, that is, it goes down to one Angstrom (i.e., 10^{-10} meters).

Also, AFM (i.e., atomic force microscopy) is a high-resolution scanning probe microscopy. Differently from conventional microscopes, it does not use lenses. The size of the probe only limits the resolution of this microscope and its resolution may go down to below one nanometer. This technique has the advantage over electron microscopy in that it may be used in solution. However, when this technique is used for biological application, the preparation of the protein sample may be complicated and time consuming. In fact, the experiment repeatability may be affected as a result of this, (http://www.nobelprize.org/; Zhao et al., 2006; Ng et al., 2007).

Chapter 3

The Crystallization of Proteins

3.1 Theory

3.1.1 The modelling of protein adsorption and homogeneous crystallization

It has been suggested in the previous chapter that the most common initiation step of amorphous polymerization is the misfolding of a protein monomer (i.e., molecule). Also it has been said that protein monomers nucleate when their energy minima are close enough to aggregation's, that is, when they generate a conformationally, and spatially, homogeneous patterned configuration. Furthermore, it has been suggested that proteins are sensitive to a wide range of mechanical and chemical stresses that may induce misfolding and, thereafter, initiate nucleation or amorphous aggregation. This would mean that mechanically, or chemically, induced misfolding events do trigger ordered structuring. That is to say, environmental disturbances, or phase changes such as the approach to, or the presence of, a surface in solution may trigger protein molecule amorphous aggregation or nucleation (and, possibly, favour crystal growth). More specifically, when protein monomers reach a surface they may adsorb, or structure, onto it. The above-mentioned environmental disturbances may, also, instigate conformational activity, or denaturation, before and during, or after, adsorption (or structuring). That is to say, statistically determined protein features may arise at the solid-liquid interface and progressively evolve, while inducing continuous adsorption dynamics.

As previously stated, proteins are copolymers that are made of units with diverse hydrophobic properties (i.e., amino acids). The folded lysozyme molecule is made of 129 units and it presents five α helical and five β sheet regions as well as random coils and β turns.

Protein clustering in the bulk is proportional to the chances of inter-chain interaction among the copolymeric molecules, that is, it stems from their motion or conformational activity. The latter might be well altered by the presence of a solid-liquid interface. Indeed, in the latter case the protein hydrophilic and hydrophobic portions will try to match the solid surface portions with similar attributes in an attempt to reach the ensemble energy minimum. That is, local energy of adsorption dynamics would arise. This is well represented in Fig. 3.1.

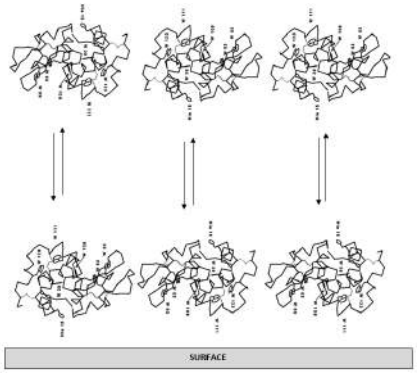


Fig. 3.1 *The folded lysozyme is a compact protein of 129 amino acids that has five α helical regions (the region that runs from residue 109 to 115 and other two regions that run from residues 80 to 84 and 120 to 124). Also it has five β sheet regions, random coils and β turns. During adsorption, the protein hydrophilic and hydrophobic portions will try to match with the hydrophilic and hydrophobic surface sections, respectively, in an attempt to reach the ensemble energy minimum. The energy barrier of adsorption is, usually, described by the Gibbs free energy of adsorption* $\Delta G_{ads} = \Delta H_{ads} - T\,\Delta S_{ads}$ *where* ΔG_{ads} *represents the change in the system free energy, H is the enthalpy, T is the temperature and S is the entropy, (the lysozyme monomer structure is from the PDB, file 8LYZ).*

The free energy of aggregation in the bulk has been described in the equation 2.1 already. According to the latter equation the contact free energy becomes more negative whenever there is an increase in the contact interaction parameter χ, the number of hydrophobic residues Φ, the chain length and the volume fraction of the copolymer in solution. Nevertheless, according to the classical Gibb's equation:

$$\Delta G_{ads} = \Delta H_{ads} - T\,\Delta S_{ads} \qquad (3.1)$$

the adsorption and structuring onto an interface is proportional to a well-defined energy barrier, which, in the literature, has been, in fact, defined as an elastic (i.e., locally determined) barrier.

Likewise the diffusion to an interface has been defined as a random progression. That is, similarly to the bulk fluctuating clustering dynamics, also the protein surface structuring process has been defined as a function of the self-diffusion coefficient (D_s), the time (t), the bulk concentration (C_b) and the adsorbed concentration (C_s) in the 3.2 equation:

$$C_s = 2C_b \sqrt[2]{\frac{D_s\, t}{\Pi}} \qquad (3.2)$$

Where, D_s is an entropy-driven, and, in fact, Brownian motion related, random variable. That is to say, almost certainly, the protein monomer diffusion to, and adsorption onto, the solid-liquid interface is statistically determined. Indeed, it has been well explained in the literature that interfacial structuring occurs when the probability (p) that the monomer bounces result in adsorption at the solid-liquid interface is higher than the probability (1-p) that the monomer rebounds, (Feller et al., 1966; Young et al., 1988). Since protein monomers diffuse performing bounces that are governed by the self-diffusion coefficient (D_s), the coefficients that are determined by the solution environmental factors (such as D_m) are equally important. That is, D_s, is a motion related parameter and, hence, it is constrained by the suspending medium.

The study of surface structuring dynamics has been an area of scientific investigation for decades. It is now clear that the thermodynamic energy barrier for protein adsorption stems from highly interdependent factors (and this is well explained in chapter 6). This elastic barrier is determined by both diffusion related and conformationally determined multi-step dynamics, that is, depending on locally induced factors, one or more steps will be rate limiting the overall adsorption process. That is, the related kinetics are determined by the forces that drive the protein molecules from the solution compartment into the interface compartment. The Vroman effect is a practical consequence of the above multifactorial dynamics and it is, often, observed in multi-component protein solutions (such as blood serum). That is, kinetically, low-molecular weight proteins diffuse, and adsorb, faster than other protein molecules. Nevertheless, the higher-molecular weight molecules displace the low-molecular weight ones, since their interfacial aggregation dynamics are thermodynamically favoured (Milner, 1907).

Furthermore, according to the Fick's core theory (Fick, 1855) if the diffusion stage was rate limiting, for a given entropy value ($T\Delta S_{ads}$), the free energy of adsorption would depend on the diffusion coefficient only and the adsorption would occur fast. Indeed, according to the Young's equation (3.3) higher diffusion coefficient values induce higher adsorption rates:

$$D_s = {C_s}^2 \Pi \Big/ 4t{C_b}^2 \qquad (3.3)$$

where, again, D_s is the diffusion coefficient, t is the time, C_b is the bulk concentration and C_s is the adsorbed concentration. Conversely, the overall adsorption process has been often observed slow. That is, the above mentioned energy barrier would be primarily related to the dynamics of adsorption at the interface (rather than to the diffusion to it). Also, the entropy variable might evolve progressively, due to different factors, and become rate determinant. This would, hence, mean that the surface chemistry, as well as topography, could well enable control over the protein adsorption step. Nevertheless, some protein molecules seem to adsorb indistinctively on surfaces having very different chemistries exactly in view of the fact that, probably, the entropy variable (ΔS_{ads}) is primarily affected by solution factors (which include intrinsic solute molecular properties and solvent, or co-solute, related factors). That is to say, as a result of the multifactorial interrelationship within the adsorbing ensemble, the solution chemical potential might taper the energy contribution that stems from the solid surface properties. In other words, the effect of the solid-liquid interface chemical potential on the adsorption dynamics would seem absent, while it has been only concealed. That is, the relative importance of the different adsorption chemical potentials may evolve with respect to time and induce different dynamics, entropy values and adsorption rates at different times.

Subsequently, the energy barrier concept and the Fick's law have been recombined in the literature, and the protein adsorption process has been remodelled into an elastic energy barrier model. Earlier in this report, the self-diffusion of a protein monomer has been defined as a motion-related process, and the local variability of the mutual diffusion coefficient has been, also, mentioned in relation to this. It is not by chance that the modelling from the literature has depicted an ideal plane, just below the interface, that becomes increasingly supplied with the solute molecules that diffuse from the bulk solution against the nominal concentration gradient. Hence, unwanted perturbations in any of the above parameters may slow, one step only, or the whole adsorption process. More over, a modified resonant microbalance has been, recently, used to experimentally observe the adsorption delays that are induced by the aforementioned energy barrier (Varoqui et al., 1985; Clark et al., 2007).

As previously explained, the monomer diffusion to the solid-liquid interface during adsorption is hardly regarded as the rate-limiting step of the whole adsorption process. It has been, also, said that protein monomers may induce local alterations at the interface while adsorbing. Therefore, while the diffusion coefficients predominantly govern the behaviour of the protein molecules while these approach a surface, their structuring at the interface must present a broader set of governing parameters. Indeed, once the protein molecules have gathered by the interface different dynamics start up and mechanisms such as surface dehydration, ion transfer, and overlap of electrical fields may govern the adsorption dynamics at turns. That is, alterations in the surface features may well take place as a result of the initially adsorbed protein layer and determine, or simply alter the relative importance of, the leading parameters. This would also mean that additional environmental factors (such as the additional solutes and solvent responses) may, in turn, become the leading forces for adsorption. That is to say, almost certainly, the adsorption of protein monomers is driven by the interplay of different interdependent factors that control the interaction between, not only, the solid surface and the protein monomers, but also, between these and the solvent, and the co-solute molecules. However, so far, not all these factors have been satisfactorily identified or characterised (Galisteo et al., 1995; Chun et al., 2006).

Furthermore, the above-mentioned adsorbing system has bee conventionally described by means of a theoretical model consisting of a solvent I and solute II (Gibbs et al., 1876, and Guggenheim et al., 1967). Indeed, this model describes an interface compartment, where the solute and the solvent dynamically coexist. That is, the molecules quickly gather by the interface but induce interface tension changes, well after. Nevertheless, these changes appear to be determined only by solution chemical potentials, since the amount of the adsorbed mass does not seem influential. Hence, the adsorbing solute-solvent ensemble is governed by different chemical potentials, the relative importance of which evolves progressively. This may mean that at a certain stage the positioning of the solution molecules only might govern the

adsorbing dynamics within the interface compartment and alter the interface energy.

Moreover, due to the stericity of the protein molecules different local chemical potential values might evolve within the adsorbing layer. In fact, protein monomers are characterised by a sterically mobile chemistry as they present chemical patches that can dissociate differently depending on different local environments. As a result of their conformational activity, the different molecular conformations (and their ionised, or solvated, forms) generate, in turn, different local chemical potentials. That is, the protein steric chemistry evolves with respect to time and generates variably charged species and local solutions with very different features (or adsorption dynamics). Hence, the local solution chemical potentials dynamically coexist and evolve to form a gradient of potentials by the solid-liquid interface during adsorption. Also, since the solvent and co-solute promptly respond to the above variability, protein monomers may also reversibly (or irreversibly) unfold and generate very different local features within the adsorbed layer. This would generate, also, a broad range of surface aggregation mechanisms, that is, a probabilistic scenario that may result in an anisotropic, but ordered, structuring (Ward et al., 1944/1946; Miller et al., 2000; Creighton, 2002; Alahverdjieva et al., 2007).



Fig 3.2 *The unfolded protein (U) is in a very fast equilibrium with its mis-folded intermediate form (I). This, in turn, is in a slow equilibrium with its natural form (N), (Creighton, Protein Structure, Second Edition, IRL Press, 2002).*

Since protein ordered structuring is observed favoured by the solid-liquid interface, this very probably stems from the enhanced unfolding-refolding equilibria that are reported to facilitate nucleation (Kaulmann et al., 2003). That is, a greater number of these reversible equilibria might occur by the hydrophobic solid-liquid interfaces, that is, exactly, where the nucleation has been proven, regularly, enhanced.

3.1.2 The modelling of protein heterogeneous crystallization

As previously stated, slow adsorption kinetics have been often observed and this might demonstrate that the adsorption dynamics at solid-liquid interfaces are not diffusion related only. Ward et al. have observed, since 1944, that factors different from the diffusion coefficients determine the passage of long-chain compounds from a solution compartment into an interface compartment. Later on, this has been further confirmed, also for proteins, by Varoqui et al. in 1986, Schaaf et al. in 1987, and Clark et al. in 2007.

Although, the exact chronology of the steps of protein adsorption has not been fully clarified yet, it may be supposed that by the time that the changes in interface tension take place, the adsorption energy minimum of the adsorbing ensemble has occurred already. That is, progressive local alterations of the protein conformations (and solvent, or co-solute structuring) would occur within the interface compartment. These would induce different local chemical potentials and, thus, local decrements in interface tension. During heterogeneous nucleation, the solution factors (such as the solute concentration, solution pH and ionic strength) might, alone, induce local chemical potentials in the interface solution compartment and reduce the cluster surface tension by the solid-liquid interface before it actually adsorbs. Differently, the compartmented volume at the solid-liquid interface might become thinner during the adsorption onto the above interface and this might induce increased protein concentration. This could, alone, induce the passage of the monomer from its natural form into an intermediate form, or other clustering dynamics. According to Creighton, the above passage is an extremely slow step, which may also contribute to determining the delayed changes in interfacial tension. These local changes in interfacial tension have been, also, thermodynamically parameterized in the following equation (Gibbs J.W. et al., 1876; Guggenheim et al., 1967).

$$d\gamma = -\left[\Gamma_2 - \left(\frac{\eta_{B_1}}{\eta_{B_2}}\right)\Gamma_1\right] d_{\mu_2} \qquad (3.4)$$

in this equation, the time factor is not directly regarded. However, the change in interfacial tension ($d\gamma$) is regarded as being proportional to the local molarity (Γ), which is, also, associated with time dependent local mass fluctuations at the inter-phase. That is, $d\gamma$ is proportional to the number of moles of solvent (1) and solute (2) per unit area, while the terms (η_{B1} and η_{B2}) are the number of solute moles within the different sections of the inter-phase.

It is also well known that proteins may crystallize in a bulk (i.e., give homogeneous crystallization) or at an interface (i.e., give heterogeneous crystallization). Moreover, it has been mentioned in the previous sections that proteins may cluster in the bulk according to diverse pathways. One of these is the templated aggregation, where monomers add onto a pre-existing aggregate (Kelly, 2000). It may be supposed that, during the adsorption at the solid-liquid interface, the latter clustering mechanism is, especially, favoured over all the other possible structuring dynamics. Accordingly, Guggenheim suggests that the adsorption at the solid-liquid interface would be determined by a controlled passage of the solvent and the solute molecules from the bulk solution into a well-compartmented volume at the solid-liquid interface. In the latter ordered structuring might, also, be facilitated. Also, computing simulations have demonstrated that homo-polymers aggregate and crystallize when these have different conformations (that is, at different conformational transitions), while copolymers aggregate or crystallize with exactly the same conformational transition (Junghans et al., 2008). That is, environmental factors might facilitate amorphous aggregation and nucleation likewise. Since protein monomers are copolymers, it may be supposed that their molecules nucleate when the environmental conditions, within the well-compartmented interface volume, favour an elected conformational pathway. That is, the solution conditions such as the ionic strength, or pH, and the presence of a template surface, may favour conformational equilibria that favour ordered structuring within the above compartment (Kaulmann et al., 2003). Hence, the nucleation of proteins may be probabilistically induced either by the protein monomers that assemble in a three-dimensional structure (as a result of solution factors, alone), or by a pre-existing substrate that is made either of the adsorbed monomers, or inorganic material.

This would, certainly, contribute to understanding as to why specific surface roughness (or porosity) and chemistries, or topographically, and chemically, designed surfaces enhance protein nucleation.

The increased structuring of proteins onto rough or chemically favourable surfaces is a well-known phenomenon. So far, the effect of surfaces with variable topography and chemistry on the structuring of proteins at the above interface has been, in fact, reported in several experimental works (Sanjoh et al., 1999/2001; Stolyarova et al., 2002; Van Der Veen et al.; 2004, Chayen, 2006; Ying-Xin Liu et al., 2007). With respect to this specific topic, it is worth emphasizing the study by Rechendorff et al., 2006, where the adsorption of fibrinogen on nano-rough tantalum films increases of 70 ± 10 % for only a 20 % increase in surface area. Very probably, since the free energy at the solid-liquid interface decreases following adsorption, favourable conformational pathways might become statistically significant and enhance also the protein structuring dynamics.

Until now, different growth modes have been modelled for the structuring dynamics at the solid-liquid interface. These have been categorized into the layer-by-layer deposition (i.e., the Frank-van der Merwe mode), the 3D island deposition (i.e., the Volmer-Weber mode), and the 3D island-on-wetting-layer deposition (i.e., the Stranski-Krastanov mode), (Chambers S. A., 2000). The contending dynamics between the solute (or solvent-mediated) interaction forces, and the solute/solid-substrate binding forces is well expressed in these models. Indeed, the solute/solid-substrate binding forces are weaker in the Volmer-Weber mode, which is the main reason why a 3-dimensional island pattern is observed in this model (Volmer et al. 1926). An advanced model, where atoms tend to form rafts with a specific configuration and free energy, has been, recently, developed by Abraham et al.. This is described in the 3.5 equation:

$$\mathrm{E}(\Gamma) = \tau L(\Gamma) + (\tau - \varepsilon^0)\,\mathrm{A}_1(\Gamma) \qquad (3.5)$$

where the term $\tau A_1(\Gamma)$ represents the surface energy of the upper surface, that is, $A_1(\Gamma)$ is the total area of contact with the surface and τ is the surface tortuosity, while the term $-\varepsilon_0 A_1(\Gamma)$

represents the binding energy with the surface. The term $\tau L\ (\Gamma)$ represents the total surface energy, where $L\ (\Gamma)$ is the total length of the intersection between the rafts and the substrate (Abraham et al. 2009). The hydrophobicity of a surface, in fact, is a direct indicator of its interfacial tension (i.e., free energy), and it is one of the different factors (possibly, the main factor) that contribute to defining the chemical potential of the solid-liquid interaction ensemble. It has been, indeed, mentioned in the previous paragraphs, and it is well reiterated in the above model, that the decrease in the interfacial tension locally favours the adsorption dynamics at solid-liquid interface. That is, the structuring at the interface is most favoured where the surface features induce high values of contact angle and, therefore, where, after adsorption, the interface chemical potential (i.e., energy) is most decremented.

It has been also recalled in the previous paragraphs that one of the most common amorphous aggregation (or nucleation) initiation steps is the misfolding of a protein monomer and that some mechanical or chemical stresses may well induce misfolding. Also, it has been said that proteins nucleate via polymerization-like reactions, when all the energy minima within the adsorbing ensemble are close enough to those typical of aggregation. This would also mean that since protein monomers are folded into different shapes by the solvent (i.e., water) and its co-solutes, these both might play a major role in controlling the overall structuring process. Nevertheless, the monomers of some proteins may adsorb to the interface while misfolding. That is, similarly to any other environmental perturbation, the phase change by an interface, alone, may trigger misfolding equilibria and initiate amorphous aggregation, or nucleation. The above-mentioned phenomena have been both experimentally observed, and computationally described. However, so far, a direct relationship between the misfolding/unfolding step and the aggregation (or nucleation) dynamics at the solid-liquid interface has not been proved yet.

Nevertheless, it is well known that water molecules promote the shape of proteins and DNA molecules. Hence, its role in determining non-specific intermolecular contacts among molecules that group in the bulk (or by the solid-liquid interface) is, certainly, implied. It has been, recently, demonstrated that the arrangement of peptides at an interface is directly related

to the water-water hydrogen bonding properties. That is, interaction forces of different nature occur among the protein molecules in solution, or between these and the solvated solid-solution interface, and govern orientation. Also, the role of water in the lysozyme crystal structure has been proved. That is, there is, also, an intra-crystalline solution that maintains globular proteins in their native configuration when these are part of a crystal structure (Forciniti et al., 1991; Lu et al., 1999; Dennis et al., 2000; Goyne et al., 2002; Zhao et al., 2009).

Gibbs et al. (1876) and Guggenheim et al. (1967) have suggested that both the solvent and the protein gather at the interface where they dynamically coexist. Also, it has been stated, earlier in this report, that these dynamics induce changes in interfacial tension. Though, (according to the observations by Clark, 2007) the amount of adsorbed mass is not influential on favouring the protein adsorption process. That is, for an ideally homogeneous surface, the local changes in free energy would be directly proportional to the solution chemical potential gradient only. This would mean that non-specific solvent-mediated forces, alone, might govern the overall adsorption dynamics. Though, the solvent-mediated interaction forces are restrained by factors that are either intrinsically induced by the type of solid-liquid interface and protein, or externally imposed (such as the solution pH, ionic strength or composition).

3.1.3 The classical crystallization theory in comparison to the recent models

According to McPherson (1991), the homogeneous crystallization of proteins has been performed since 1840. Indeed, historically, more proteins have been, progressively, crystallized by different scientists: hemoglobin (1840 – 1860); globulin (1880 – 1900); hen egg albumin (1890 – 1900); horse serum albumin, concanavalin A and concanavalin B (1910 − 1920); urease and insulin (1920 − 1930); trypsin, trypsinogen, trypsin inhibitor pancreas, soybean, pepsin, pepsinogen, chymotrypsm, chymotrypsinogen, ribonuclease, hexokinase and diptheria toxin (in the 1930's); carboxypephdase, ferritin, catalase, GPDH and lysozyme (1930 − 1940). That is, the crystallization dynamics of proteins have been investigated for years now. At present, it is believed that the protein intermolecular interaction, primarily, originates from

the intimate structure of their monomers. This would also mean that the protein tertiary structure, and the anisotropy of its surface chemistry, might play a major role (Sommer et al., 1982; Wuthrich et al., 1984; Salemme, 1988; Mc Elroy et al., 1992; Guo et al., 1995; Qi et al. 2007). Also, it has been, often, inferred in the literature that, thermodynamically, the protein nucleation dynamics occur at those solution conditions that make some elected conformations statistically significant (Cacioppo et al., 1991; Shoichet et al., 1991; Muschol et al., 1997; Penkova, 2002; Nanev et al., 2006; Nanev, 2007). Indeed, according to these observations, the protein crystallization process may be visualized as a statistically initiated phenomenon. That is, this would occur at those solution conditions that allow each molecule to rapidly establish specific intermonomeric interactions while performing reversible (or irreversible) conformational equilibria within the local solution energy minimum. Subsequently, the protein monomers would keep englobing into repeatable units and generate different geometries depending on the favoured conformations (Oki et al., 1999).

The study of nucleation (or crystallization) in proteins is a challenging topic of research and, so far, most of the work in this specific field has been approximately advanced. That is, this is a complex topic and only a thorough understanding of all the different pathways to nucleation (or crystallization) may allow for a certain control over the relating dynamics (Chayen, 2004). Simplistically, clustering phenomena (and, therefore, nucleation) lead molecules, which are subjected to Brownian motion, towards amorphous aggregation (or structuring), (Northrup et al., 1992). That is, supposedly, immediately after clustering the slow Brownian motion dynamics (which are typical of oligomers) should arise at the expenses of the fast Brownian motion dynamics (which, instead, are typical of monomers), and this is well shown in Fig. 5.7. Proteins, indeed, are very peculiar solutes, since they are subjected to Brownian motion, conformational activity, folding and unfolding, and all these features might become extremely significant, especially, when the nucleation conditions varied within a wide range of values. Nevertheless, according to Anfinsen (1973), it is well known that the folding of a protein monomer is mainly driven by hydrophobic interactions. Also, the Brownian motion does not apply within the energy

minimum of the critical cluster. That is, all the factors that induce solvent structuring in the clustering ensemble (such as the temperature, solute types and their nominally defined concentrations) still play a primary role during nucleation. Indeed, the solvent structuring potential would reveal, especially, when the protein local volume fractions increase. That is, right before nucleation the locally structured solvent and the monomer conformational activity might compete in controlling the rearrangement of the cluster molecules. Moreover, although, generally, the solute conformational activity is primarily regarded to control the initiation of the nucleation dynamics, at a certain stage, solvent induced dynamics may, instead, govern the molecular rearrangement within the cluster. That is, the solute molecule hydrophobic core might reveal, as a result of the reduced solvent content, and generate new leading forces that, previously, were hidden by the natural pattern of hydrophilic residues.

According to the above description, before nucleation the active protein monomers are subjected to Brownian motion and these have native-like conformational transitions that evolve over the grouping process. In the literature, these arrangements have been modeled according to the following four stages: a first stage during which there are local conformational transitions only, a second stage where the protein monomer gains a compact structure and two final stages where the protein monomers gain their native structure (Chan et al., 1994). This might also imply that the role of the solvent becomes progressively more important. Nevertheless, the classical nucleation theory, simplistically, describes three phases only: the nucleation stage (that is, the formation of a new phase and its interface); the growth stage (that is, further phase conversion at the interface); the ripening stage (that is, the growth of large domains of at the expense of the smaller ones). Accordingly, the following equations have been reported to define the nucleation variables and relate these to the free energy of nucleation:

$$\Delta G_n = A\gamma + n\Delta_\mu = 4\pi a^2\gamma + \frac{4\pi a^3\gamma\rho}{3}\,\Delta_\mu \qquad (3.6)$$

in the above equation ΔG_n is the free energy of nucleation, A is the surface area increase, n represents the number of molecules that make the cluster, γ is the interfacial tension, a is the

cluster radius and Δ_μ is the change in the ensemble chemical potential. Also, the nucleation rate may be described according to the following additional equation

$$\frac{\mathrm{dN}}{\mathrm{dt}} = K^{+}(n_{crit})e^{-\Delta G^{*}/kT} \qquad (3.7)$$

where ΔG^* is an energy parameter that is proportional to the ratio $16\,\pi\gamma^3/\rho^2\,\Delta_\mu^2$, and $K^+(n_{crit})$ is the formation rate of the critical size cluster. According to this equation, when $\Delta G^* > kT$ the phase is metastable, while when $\Delta G^* < kT$ the phase is unstable. That is, the nucleation occurs in the metastable phase when the cluster radius exceeds a critical radius (a_{crit}), which, in turn, is defined here below in a last equation:

$$a_{crit} = \frac{2\gamma}{\rho\Delta_\mu} \qquad (3.8)$$

On the other hand, following the simulation by Chan et al., different models have been developed to define the initiation of the crystallization process with a completely new approach. According to these models, the metaphase shows spatial fluctuations of mass concentration that form clusters. That is, the nucleation may initiate with a mass fluctuation and progress according to a classical-like theory, which would be in agreement with the above equations (Lutsko, 2012). Recent modelling has proven that ordered structuring could, also, evolve from a liquid critical cluster (Lomakin et al., 2003). Furthermore, additional simulations would reveal that the inter- and intra-monomeric structuring evolves, progressively, and defines a critical number of tertiary contacts that induce the native state of the molecules within a preformed cluster. As a result of this preformed cluster, different secondary structures (or parallel conformational pathways) may be favoured. The latter simulation data have, also, been compared to experimental data (Radford et al., 1992; Guo et al., 1995).

Conventionally, lysozyme has been observed in different studies under different conditions (such as temperature, pH, different additives and different concentrations) and phase diagrams with two lines delimiting the metastable region of its solution have been plotted (Muschol et al., 1997; Manno et al., 2003).

Nevertheless, recent experimental studies have better detailed the lysozyme metastable region. The coloured plots in Fig. 3.3 show the effect of a solution multifactorial variable (ε) on the nucleation times of lysozyme and other proteins, which, indeed, are affected by nominally controllable solution factors. The normalized nucleation times have, then, been plotted against the solution ε values. The plot of the protein normalized nucleation rates and a predefined master curve define a critical region where the thermodynamic instability and the spontaneous demixing compete.

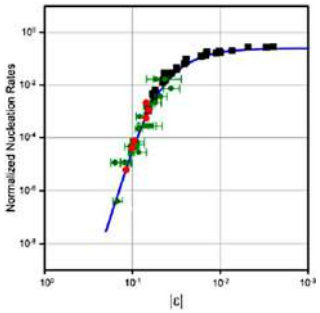


Fig. 3.3 *The normalized nucleation rates have been plotted against the ε parameter, which expresses the effects of all the controllable parameters (such as temperature, buffers, salts, pH, concentrations or additives).* ***Green****: the lysozyme crystallization induction times from the literature, (Pullara et al., 2005).* ***Red****: the data on lysozyme crystallization; these data have been produced in different studies at different pH, temperature, and solute or salt concentrations.* ***Black****: sickle hemoglobin (HbS) fiber initiation kinetics, (Vaiana et al., 2005). In* ***Blu****: data derived from the universal scaling properties of critical fluctuations, (Pullara et al., 2005).*

That is, different zones of fluctuating concentrations are characterized by a specific lifetime at a specific amplitude and these both are inversely power dependent on the temperature dependent parameter ε, which is also defined in the following equation (3.9):

$$\varepsilon=(T-T_s)/T_s \qquad (3.9)$$

where T is the temperature and T_s is the reference temperature on the derived spinodal line (Pullara et al., 2005). Also, Debenedetti (1996) well describes a spinodal line in a temperature-concentration phase diagramme. This line separates the region in which the protein solution is unstable from the region in which the protein starts demixing without nucleating (that is, a spinodal decomposition line). All the above guidance and the 6.1 equation, may provide a conceptual description of the protein mass gradient that forms immediately before nucleation. Hence, conformational dynamics and solvent-mediated (non-specific) forces (that is, hydrophobic and hydrophilic interaction forces) might, very probably, compete in forming the aforementioned fluctuating pattern of infinitesimally different protein mass concentrations.

It has been mentioned in the previous paragraphs that, generally, depending on specific environmental solution (or surface) factors, the nucleation of proteins may be regarded as an homogeneous or heterogeneous process. Also, it has been said that, according to the most recent studies, the homogeneous nucleation of proteins is triggered by a metaphase that shows spatial fluctuations of mass concentration, which, in turn, form clusters. That is, nucleation and crystal growth develop when the clusters restructure and assemble further, respectively. Indeed, the most important stages for crystal growth are the nucleation and the stage immediately before ripening. In these both, the same set of parameters may orchestrate both nucleation and crystal growth. Nevertheless, the critical nuclei form via homogeneous nucleation (with highest rates well before ripening), while the pathway for crystal growth via ripening (i.e., the Ostwald ripening) occurs at a later stage only. During ripening, indeed, the larger crystals grow further at the expenses of both pre-nucleated crystals and smaller crystals. Furthermore, once the ripening has started and new crystal surfaces have formed, these surfaces themselves may become sites for nucleation. This also has, often, been defined as heterogeneous crystallization.

As a result of this, it is often difficult to understand if the nucleation event has taken place via an homogeneous or an heterogeneous pathway. It is even more difficult to understand whether the different supersaturation values may favour homogenous nucleation over heterogeneous nucleation or vice versa. Recently, the protein heterogeneous crystallization on inorganic surfaces has been characterized also by Tosi et al. 2011. In this study two different protein concentrations have been defined C_{lim} and C_{crit} (that are the lowest and the highest concentrations below and above which nucleation takes place, respectively, on charged or non-charged surfaces only). While, at concentrations that are between C_{lim} and C_{crit}, nucleation occurs on both surfaces. In another study by Tsekova et al. (1999) it has been observed, again, that the heterogeneous nucleation dynamics of lysozyme are, thermodynamically favoured over those that are typical of the homogeneous nucleation. As suggested earlier in this chapter, the above dynamics may result from multifactorial correlations that generate random entropy values within the adsorbing ensemble. In other words, the relative importance of the different

adsorption chemical potentials may evolve and induce time-dependent dynamics so that the energy contribution by the solid surface and the solution chemical potentials compete while governing the whole nucleation process. That is, the surface chemical potential may play a major role during heterogeneous nucleation only for a specific set of conditions, which may locally arise. Indeed, Abraham et al. have attempted to model how the surface features may locally favour the structuring phenomenon. That is, according to the 3.5 equation in section 3.1.2 of this chapter, the presence of a substrate with specific features does induce the formation of locally adsorbed pattern with energetically favoured configurations.

Historically, there are few milestones relating to the study of protein heterogeneous crystallization. McPherson et al. (1987) first introduced the use of mineral substrates to crystallize proteins. Then, Hemming et al. (1995) used lipid layers. Later, Fermani et al. (2001) observed that charged surfaces enhance the crystallization of certain proteins. In the same year, Sanjoh et al. (2001) observed that silicon surfaces facilitate the crystallization of proteins. Finally, D'Arcy et al. (2003) used natural substrates for the same purpose. Nevertheless, at present, the theory of heterogeneous crystallization is currently poorly understood and the classical theory for homogeneous nucleation is often used to elucidate also the heterogeneous phenomena. Though, according to this theory, the clustering of protein monomers is driven, primarily, by the nominal protein concentration.

Nevertheless, although proteins may assemble via a first order phase transition, certainly, their clustering dynamics are not determined by the solute concentrations at supersaturation only. That is, nucleation may, only, apparently follow the classical theory, while a multifactorial equilibrium might, in fact, induce also the homogeneous nucleation processes. Indeed, a fluctuating pattern of local concentrations before nucleation in the bulk has been, more recently, modelled. In this new model the work for the nucleus formation and the local solute concentrations might still be correlated with integrated forms of the conventionally regarded parameters, such as the nucleus critical radius and the nucleation rate. Accordingly, also the structuring of proteins at an interface would be locally determined. Though, additional

factors, such as the interface potential energy and the protein monomer chemical stericity or conformational activity, would, also, be highly influential. That is, these alone might govern the adsorption, and interfacial structuring, kinetics. In the most recent studies, indeed, different additional nominal, or local, factors (which include the solute concentration, solution ionic strength, solid-liquid interface energy and the relative energy of interaction with the protein surface) have been taken into account to describe the enhanced heterogeneous nucleation dynamics of proteins, (Nanev, 2007).

The free energy of heterogeneous and homogeneous nucleation have been conventionally compared in the following equation:

$$\Delta G_{heter} = \Delta G_{homog}(1 - E_{adhes}/2\gamma) \qquad (3.10)$$

where the free energy of heterogeneous nucleation (ΔG_{heter}) is favoured over that of homogeneous nucleation (ΔG_{homo}) by the surface specific adhesion energy (E_{adhes}) and the free energy (γ) ratio. Nevertheless, it has been also observed that, in the specific case of lysozyme, although the homogeneous nucleation might occur according to the classical theory, the growth of very small lysozyme crystals depends on the nucleation rates only. That is, the nucleation and growth stages seem to occur independently from each other only when the crystal linear size increases. This would mean that solvent mediated non-conventional solution factors influence nucleation. During crystallization, in fact, crystals are surrounded by a solute gradient, which is comparable to the one that is generated at a solid-liquid interface. The above binary phenomenon is expressed by a boundary layer theory in the following equation:

$$U = \frac{\nu}{L}^2 \sqrt{\frac{G_r}{S_c}} \qquad (3.11)$$

in the above equation U is density gradient around a crystal, v is the kinematic viscosity, L is the characteristic linear length of the crystal, and G_r and S_c are the Grashof and the Schmidt numbers, respectively. G_r has been defined as:

$$G_r = gL^3 \frac{\Delta_\rho}{\rho} \frac{\Delta_c}{\nu^2} \qquad (3.12)$$

where Δ_c is the local bulk concentration, g is the acceleration due to gravity, ρ is the density, v is the kinematic viscosity. Also, S_c has been defined as:

$$S_c = \frac{\nu}{D} \qquad (3.13)$$

where D is the diffusion coefficient of the solute. According to the above theory, a diffusion related convective transport occurs in the boundary layer, that is, the solute gradient at the crystal-solution interface. Indeed, according to the data by Pusey et al., 1985, flows that are driven by the solute gradient (and, thus, the viscosity of any structured solution) may induce the crystal growth rates of very small crystals only. Similarly, more recently, Lutsko et al., 2012, have modelled that, only during the post critical growth phase of the protein solution, a depletion zone surrounds the cluster.

3.2 Applications

There are two major applications of the protein crystallization process: the crystallization of proteins in the pharmaceutical and bioprocess industries, and the crystallization of proteins in the food industry. In both industries there is still poor control over the growth of protein crystals or their nucleation. In the pharmaceutical industry, especially, the main factors that induce the adsorption of proteins and that control their purification (via crystallization or precipitation) have been, so far, poorly understood.

The crystallization process has been often used to purify and classify several compounds including proteins. Proteins are extremely complex copolymers and crystallization techniques have been, often, used to purify a specific protein from a mixture or to produce high-quality protein crystals for x-ray diffraction. That is, these techniques may be used to detail the protein native structure for practical applications such as drug discovery studies or enzymology recognition processes. Indeed, drug discovery techniques use structure based drug design and, therefore, necessitate the detailed molecular structure of the protein of interest.

An example of this is Captopril, which is a drug that is used to relieve hypertension. This drug is an angiotensin converting enzyme inhibitor and the research on the structure-based design of this drug in connection with the above-mentioned enzyme has been well reported in the literature (Cushman et al., 1991; Bugg et al., 1993). In addition, as a result of the recently developed recombinant DNA technology, most of the next generation pharmaceuticals will be proteins that need purification, and crystallization is one option.

Similarly to other drugs the production of proteins via crystallization needs optimization during scale up. Generally, proteins tend to crystallize only at very high supersaturation concentrations while forming highly solvated and fragile crystals. It is well known that during a pharmaceutical production process, the crystallization conditions affect the morphology and the particle size distribution (PSD) of the crystals. This becomes extremely important in pilot-scale manufacturing, as the use of crystallization can notably reduce the production yield. The most common problems that are observed when crystallization is used in the pharmaceutical industry are: the control of supersaturation, the efficient use of seeds (or multiple solvents) to improve the production (or purification) yields, and the identification (or selection) of the best polymorphic form.

As previously mentioned, the crystallization of proteins is also important in food industry. The stability of proteins in food is necessary to guarantee the texture, the quality and the shelf-life of the product. Protein crystals, emulsions or other structures may influence important product performance parameters. Also, during production, there is a continuous correlation between the product composition (such as the presence of certain types of proteins), or the processing conditions, and the performance of the product. In many emulsified food formulations, the structural properties of the emulsion define product key performance indicators, such as the stability and sensory properties. Emulsions are by definition thermodynamically unstable. The addition of emulsifiers including proteins (or thickening agents) to food formulations prevents physical changes such as flocculation (or coalescence) of O/W (i.e., oil in water) emulsions. Consequently, the control over the crystallization of proteins

in food formulations is, primarily, required to control their stability, (Relkin P., et al. 2003).

Given that food formulations are extremely complicated, at present, there is no clear understanding of, or control over, the phase behaviour of complex protein crystallizing systems. A better understanding of the different factors that may affect the crystallization of a protein in food product formulations, and the selection of special ingredients, may enable control of food degradation processes. That is, although some protein crystals may provide structure, the crystallization of proteins in food formulations is, generally, regarded as an unwanted separation process. An example of food where proteins are the primary ingredients is the soybean where the protein component (which is 80 % of the raw food) is made of two main types of protein: conglycinin and β-conglycinin. There is currently an increasing interest in health and diets. Indeed, in the literature (describing clinical trials) it is inferred that soy helps to prevent several diseases (such as coronary heart disease, cancer, and osteoporosis) and that, as a result of this, soy is, now, one of the most commonly produced processed food, (Yada, 2000).

3.3 Techniques for Detecting and Measuring Crystallization

Historically, the hanging drop (or sitting drop) method has been one of the most accredited crystallization techniques for proteins. This vapour diffusion technique consists of a drop of the crystallizing protein solution hanging from the lid (or sitting on a pedestal in the side compartment) of a sealed container, which contains a reservoir of the same precipitant solution. Initially, the precipitant concentration in the droplet protein solution is not sufficient to induce protein crystallization, however, as water evaporates from the droplet (which is in equilibrium with the reservoir of the precipitant solution) the optimal crystallization conditions are achieved and nucleation is initiated as a result of this. Nevertheless, the droplet, aside from sitting on a chosen surface, is also surrounded by air, which, in itself, might trigger nucleation and, thereafter, crystallization. The hanging drop apparatus is shown in Fig. 3.4.

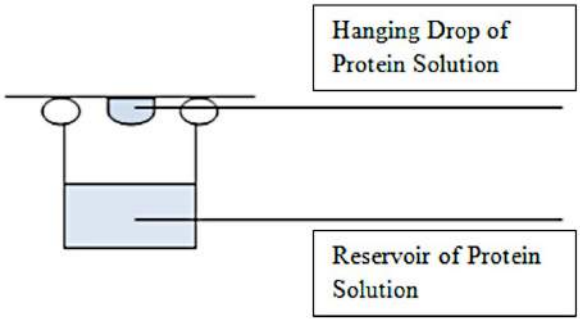


Fig. 3.4 *The hanging drop method.*

This set up was used for the first time in microgravity experiments in 1985, and, to further facilitate the use this method, commercial screening kits or commercial crystallization robots have been produced in 1990. According to the Hampton research corporation (1999), the above method may be used to crystallize proteins by:

- decreasing the temperature,
- applying evaporation,
- increasing the concentration of the protein,
- directly mixing these with a precipitant and creating a supersaturated condition,
- increasing the precipitant salt concentration, that is, salting the protein out,
- altering the pH or the dielectric properties of the solvent,
- adding a ligand that changes the solubility of the protein,
- inducing volume exclusion while adding a polymer such as PEG (polyethylene glycol),
- adding cross-bridging agents,
- decreasing the concentration of the solubilizing agents.

At present, the crystallization of proteins is a highly regarded research topic in the biomedical industry. As a result of this, the development of novel crystallization methods (such as high-throughput protein production, targeted screening and tagged crystallization) has become a primary research activity in most of the modern pharmaceutical laboratories.

As stated in the previous section the crystallization of proteins is a highly regarded research topic. Indeed, the development of new drugs is often performed using structure-based designs, which necessitates the detailed molecular structure of the target protein (i.e., the structure of the relating crystal). Also, therapeutic proteins (such as insulin from recombinant E. Coli) make use of precipitation, or crystallization, as key purification stages of their downstream processing. Furthermore, also common industrial enzymes (such as proteases, amyloglucosidase and glucose isomerase) are, generally, purified via crystallization, (Datar et al.1996).

Most of the protein crystallization protocols yield roughly only 30 % of the input proteins. Not all the yielded crystals, however, are well structured. As a general rule, the structure of protein crystals may be determined using two different types of techniques: nuclear magnetic resonance and x-ray crystallography. The nuclear magnetic resonance technique, which is a noninvasive determination of the protein structure, has quite low sensitivity and it cannot be used for proteins with a molecular weight greater than 30 kDa, (Branden et al. 1991). On the other hand, although, these limitations do not apply to x-ray crystallography, the use of x-ray, for this purpose, necessitates good size crystals with ordered structure. The crystals that are usually tested in x-ray crystallography are 0.1 mm size or larger, that is, large and well-structured crystals only can be tested by x-ray crystallography.

Currently, there are no rules that ensure the growth of "perfect" crystals, however, it is, generally, advisable to follow some guidelines. Firstly, crystals must be formed with a continuous process. That is solvents that permit an homogeneous solubilization and reduce the formation of impure crystals should be used. Also, the input protein must be at least 75 % pure to avoid the growth of mixed crystals. Nevertheless, the solution conditions that are necessary to thoroughly control the growth of protein crystals, often, seem unpredictable. That is, these are still actively researched on, and expertise from biology, biochemistry and biophysics, has been combined with that from mechanical engineering and computing for this purpose.

The crystallization in high-throughput laboratories is a good example of technique that is currently used to enhance protein crystallization yield rates. Also, the use of recombinant proteins, that is, proteins that are provided with an affinity tag (i.e., a polypeptide fusion partner), is an alternative method to aid purification. Although this method may, also, be used to improve solubility, the use of fusion proteins to facilitate purification is mainly advantageous. After that the affinity tags (such as DsbA, glutathione S-transferase, SBP-tag, FLAG-tag, HAT-tag, and arg-tag) are in place, the ligand bound proteins, or a modified version of these, are the new crystallization targets for the following screening research activities. Therefore, a protein may be coupled with a ligand or modified, and its structure might be, even, determined directly from a particular organism. Aside from adding an N– or C–terminal tag or a fusion protein, or altering the protein sequence, there are other additional ways to tag a protein (that is, truncating the protein molecule or chemically modifying specifically chosen residues). At present, the activities for the amelioration of high-throughput, and targeting, techniques makes the investigations in protein crystallization research primary in several pharmaceutical laboratories (Stevens, 2000; Heinemann et al., 2003).

Chapter 4

Surfaces with Controlled Roughness

4.1 Nano-patterned Surfaces

Experiments with proteins are often difficult to reproduce, and this is especially true when protein crystallization is regarded. That is to say, the use of surfaces with highly controlled features in protein research is of primary importance to resolve the above repeatability issue and allow good data interpretability. This chapter, firstly, presents an introduction listing a variety of techniques that are commonly used to prepare nano-patterned surfaces (4.1.1). Secondly (4.2), it will provide an exhaustive description of the procedures that have been used to prepare and characterize the nano-patterned substrates for this project. While chapter 5 will explain how the fabricated substrates were used as test surfaces to induce the heterogeneous crystallization of lysozyme in an air-depleted micro-batch environment.

4.1.1 Techniques to produce nano-patterned surfaces

Over the past few years, new nanotechnologies for biomedical applications have been developed, and the potential applications in relation to this have been concisely explained in chapter 3. The most recent applications consist of investigating the effects of sub-micron- and nano-roughness on protein nucleation rates and, ultimately, ameliorating their purification as well as production. Nowadays, the production of substrates with controlled micro-features is, in fact, a well-established field of research in biomedicine. NEMS (Nano-Electro-Mechanical Systems) and MEMS (Micro-Electro-Mechancial Systems) are commonly used as substrates with controlled features, since these present patterns that are below the 100 nm size and on the μm length scale, respectively. Currently, the production of NEMS and MEMS covers 14 % of

the nano-technology sector, and their use is concisely summarized in Fig. 4.1.

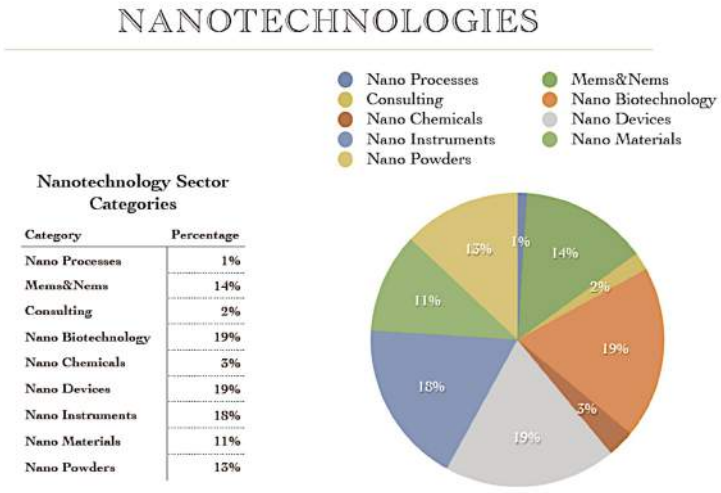


Fig. 4.1 *The diverse applications of MEMS within the nanotechnology sector. The data have been reported from the Loadpoint website.*

Historically, Carter fabricated inorganic nano-substrates by CVD (chemical vapour deposition) and performed the first experiments with bio-MEMS in 1967. Later, Manz and Widmer suggested the use of MEMS to make chemical sensing systems. Around the same time (i.e., in the 1990's) a number of microfluidic experiments were performed in the American military departments, and the manufacture of oligonucleotide chips was then performed. Nevertheless, the application of MEMS and NEMS in biology has remarkably grown since 1993, when Whitesides introduced the utilization of PDMS (i.e., Polydimethylsiloxane) to fabricate MEMS (Urban et al., 2006; Whitesides et al., 1993). To date, NEMS have been used for a broad range of specific applications, such as bio-sensing, drug delivery, electronics and imaging. The ultra-sharp tips, which are regularly used in the atomic force microscopy probes, are an example of application that has reached the market already. Furthermore, NEMS have been used, also, for other applications such as nano-resonators, integrated piezoresistive detectors and nano-accelerometers. The employment of MEMS & NEMS is predicted to, rapidly, grow especially within the three most common applications, that is, microelectronics, biochips and nano-sensors. The market growth rate has been estimated to be faster for microelectronics, while it has been estimated to be slower for biochips and nano-sensors.

Nevertheless, the most novel applications for MEMS & NEMS are those relating to biochips and nano-sensors. Biochips consist of biomolecules that have been immobilized on patterned surfaces or bead arrays, and in micro-channels or micro-wells. Biochips may be used for very different applications such as bioinformatics, bioassays, clinical diagnostics and monitoring equipment. A new range of nano-chips (such as DNA chips, carbohydrate chips and protein chips) has been recently developed. Specifically, DNA probes, that is, biochips that allow the identification of nucleic acids, are being developed already. DNA biochips might be used to diagnose genetic diseases, or predispositions, and implement fast clinical screenings. Moreover, antibody probes have been developed to detect the blood levels of pathologic proteins such as the p-53 protein (which is a tumour protein), (Atha et al., 2012). Nano-sensors, instead, might be used to detect chemical vapours (such as nitrogen dioxide and carbon monoxide), bacteria or viruses. Indeed, nano-cantilevers are nano-sensors that can detect even a single molecule (Nongyue, 2009). Definitely, the use of nano-sensors to detect bacteria in hospitals is a particularly promising application.

Nano-patterned surfaces are also used to investigate the behaviour of cells. The surfaces that are used for this purpose are, generally, highly ordered surfaces with low adhesive properties. That is, these surfaces have high chemical potential as a result of their chemistry as well as topography. Nevertheless, quite large template surfaces are, necessarily, manufactured for this purpose. Nowadays, indeed, research in this specific manufacture field, mainly, focuses on making larger areas of nano-patterned surfaces, and different methods are in use, already, to mass-produce materials with the above detailed features (Gadegaard et al., 2006). Some of the most common techniques that are used to prepare nano-surfaces with controlled features are: natural nano-lithography, electron beam lithography, colloidal lithography, polymer phase separation and metal deposition. Although the research in this field is actively advancing, in 2007, the techniques that are currently available to prepare large, and reproducible, patterned areas have been grouped into different categories, according to Wood. These categories sort the nano-patterning techniques out and are listed here below:

- Techniques for primary pattern definition;
- Techniques for primary pattern transfer;
- Techniques for secondary pattern transfer.

Techniques for primary pattern definition

Colloidal lithography: colloidal lithography consists of the self-assembly of colloidal microspheres in the periodical array of a close-packed monolayer. This lithographic technique is a simple technique that was first introduced in 1798 by Alois Senefelder. In the 1950's, it was further developed to fabricate micro- or nano-structures for integrated circuits. However, the importance of this technique increased towards the end of the last century, when its products were also used as masks for replication (Fischer et al., 1981). Around the same time, Deckman et al. (1982) extended the use of this technique to pattern large area surfaces. More recently, the Van Duyne research group (2002) has used colloidal crystals as masks for metal vapour deposition. That is, similarly to Fischer, additional surface modification steps (such as vapour deposition, ion etching or chemical modification) may be used to modify colloidal-derived nano-topographies (or their chemistries). Also, Devereaux et al. (2002) used the Langmuir-Blodget method to deposit self-organised di-block copolymer micelles and make patterned surfaces. Similarly, Liu et al. (2004) dip coated a functionalized surface in colloidal solutions. That is, planar nano-structures of colloidal gold particles were deposited from a colloidal solution onto a silicon substrate by means of terminal amino functionalities. Resolutions as high as 10 nm have been attained by means of the above method (Iovan et al., 2012). However, it is worth mentioning that, hardly, colloidal lithography techniques permit the manufacture of defect-free and uncontaminated substrates, (Ginnai T. M., 1980).

Phase separation: this is also a technique that is used to form nano-patterned surfaces. Historically, Kern et al. (1991) have shown that atoms may diffuse on a solid surface and organize into ordered nano-scale patterns. Specifically, a sub-monolayer of oxygen on a

copper (Cu;110) surface forms 10 nm wide stripes of an oxygen over-layer. Still, Pohl et al. (1999) have fabricated an ordered lattice of sulfur (S) rich substrate with dots of ≈ 3.4 nm size, by depositing silver (Ag) and sulfur (S) on a ruthenium (Ru; 0001) surface. Similarly, Umezawa et al. (2001) have fabricated temperature dependent ordered arrays of silver (Ag) sub-monolayers on copper (Cu; 111). Finally, Plass et al. (2001) have demonstrated that different concentrations of lead (Pb) may form droplets, stripes, or vacancy islands on a copper (Cu; 111) surface.

Scanning probe lithography: this is a direct or photoresist writing technique where the tip of a scanning tunnelling microscope (STM), or an atomic force microscope (AFM), is used to fabricate nano-scale patterns. These tips generate an electric field and induce direct patterning (which occurs as a result of the direct contact or the heating that is induced). These techniques may produce patterned features with size down to a single atom.

Focused ion beam lithography: this lithography is a direct writing technique, and it uses a focused beam of ions to scan a surface and to create nano-patterns of sizes down to 50 nm or below (Wanzenboeck et al.).

E-beam lithography: this is a photoresist writing technique where a beam of electrons is emitted towards a surface that has been previously covered with a layer of resist. Although this technique was developed for manufacturing integrated circuits, this is now also used to make nano-patterns for bioscience. Poly-methyl-methacrylate (PMMA) is the most commonly used e-beam resist, since it gives the highest resolution. The PMMA is, usually, first dissolved in a solvent, then spread over a surface and, finally, it is exposed. Once it has been exposed, it has a lighter molecular weight and it is developed in a suitable solvent. A resolution down to about a10 nm size has been achieved with this technique (Craighead, 1984).

Laser writing: this is a photoresist writing technique and it produces feature sizes of about 200 nm or greater. In laser direct writing, a chosen photo-resist (such as SU-8) is transparent to a specific laser beam, that is, on exposure to a laser with a specific wavelength

there are no one-photon absorption processes. Indeed, the laser spectrum is, generally, broadened. That is, ultra-short laser pulses are applied, since these broaden the laser spectrum and induce absorption. The multi-photon absorption phenomenon, two-photon absorption most probably, induces local polymerization. Finally, a development step is, usually, implemented after laser writing.

Laser ablation: this is a direct writing technique. It consists of removing material from a solid surface using a laser beam, while, directly, converting the removed material into plasma. Usually, this is, also, performed using a pulsed laser. Though, when the laser had a high enough intensity, a continuous wave laser beam may be used instead. That is, when the laser flux is low, the material is only heated as a result of the absorbed laser energy, while, when the laser flux is high, the material will be converted into plasma and, as a result of this, the surface becomes instantly nano-patterned. The laser ablation method can reach very high resolution with period sizes of less than 40 nm (De Oteyza et al., 2012; Hendrickx et al. 2005).

Techniques for primary pattern transfer

Nano-imprinting mask lithography: this technique (which includes photolithography, x-ray lithography and ion etching) transfers the pattern from a resist onto a substrate. The pattern is first transferred to the resist with a soft mask and then from the resist to the substrate by exposure to light, x-rays or ion etching. Line-patterns with width down to 5 nm can be fabricated by means of this technique (Austin et al., 2004).

Etching: this technique consists of the selective removal of material from a surface to form a specific pattern. The etching agent may be a solution, gas or plasma.

Chemical vapour deposition: this is a solvent-free, and gas-phase, deposition technique. Indeed, it is commonly used to vapour deposit very thin films with different roughness onto substrates bearing very fine patterns, such as patterns featuring 15 nm wide structures (Oshinowo et al., 1994).

Techniques for secondary pattern transfer

Hot embossing: the pattern is transferred from a mold onto a "solid", since heat and a force compressing the mold onto a rubber-like solid are applied under vacuum.

Nano-molding and casting: this technique consists of transferring a pattern from a mold (which generally is an elastomer, such as PMMA) onto a fine liquid layer. The latter solidifies once it has been put in contact with the mold.

Polymerization: the pattern is formed via surface initiated polymerization. That is, the polymerization takes place on a surface that has been previously activated.

4.2 MEMS & NEMS: substrates for the characterization of protein adsorption and crystallization

4.2.1 The use of MEMS and NEMS substrates to adsorb & crystallize proteins: repeatability issues

It has been said in the previous paragraphs, already, that highly ordered surfaces are, generally, preferred to investigate the behaviour of proteins (or cells). That is, these are necessary to ensure good data repeatability and, hence, interpretability. Secondly, it has been explained that the surface hydrophobicity is synonymous with the corresponding chemical potential, which is, yet, defined by the surface energy function. Also, in a previous sub-section (3.1.2), it has been observed that high values of solid surface energy at the solid-liquid interface may generate a stress-stimulus factor that initiates the heterogeneous structuring of protein molecules. Also, it has been mentioned that the dynamics at the solid-solution interface depend on both the protein local diffusion (which is entropy driven, i.e., Brownian motion related) and the local protein (or co-solute) concentrations. Subsequently, it has been reported that the adsorption, or structuring, of protein monomers by a solid-liquid interface occurs when the probability (p) that their, almost certainly Brownian-motion-related, bounces result in

adsorption is high. That is, when there is low probability (1– p) that the protein molecules drift away from the solid-liquid interface compartment. Almost certainly, this is a multifactorially-determined probability, as it is directly proportional to the energy barrier of adsorption (or nucleation). This barrier might, in turn, stem from the parallel (or consecutive) steps of the overall clustering pathway. Also, since the governing parameters for clustering are highly interrelated, a gradient of different factors may favour one or more of the above steps at the same time. Indeed, some proteins tend to adsorb indistinctively at surfaces having very different chemistry, as the energy barrier for adsorption is, not only, affected by the solid surface chemical potential, but also, by the protein intrinsic structure and the local solution factors that shape it. These factors, almost certainly, trigger more or less broad conformational fluctuations in the protein monomer and, therefore, alter the pattern of functional groups at the protein molecular surface as well as the related dynamics of interaction with the solid-liquid interface. Furthermore, the grouping of protein monomers at this interface may, in itself, induce alterations in the interfacial energy and, hence, govern the following dynamics of adsorption.

Having said this, it is further observed that although an increase of the surface area (i.e., energy) arises when the roughness at the solid-liquid interface increases, there might not be 100 % contact between the solution and the hydrophobic rough surface. That is, air droplets may, well, become entrained by the solid-liquid interface and induce non-controllable alterations of the local surface energy. Hence, additional uncontrollable dynamics might arise and overcome the regular adsorption (or heterogeneous nucleation) behaviours. It may be, therefore, supposed that, unless the above interference had been removed first, the effect of the solid surface features on the protein dynamics at the solid-liquid interface would be hardly detectable and, almost certainly, blurred. Indeed, since air droplets are hydrophobic, the more hydrophobic the surface is the more probably air droplets will be embodied in its sub-compartments. That is, this would, very probably, determine non-controllable alterations of the surface features and form a substrate with unknown features, i.e., a surface bearing a matrix-style pattern that is newly available for adsorption, or nucleation (Shang et al., 2005; Martines

et al. 2006). As a result of this, the above interference phenomena might well alter the experimental data describing the adsorption (or nucleation) of proteins at the solid-liquid interface and, hence, aggravate repeatability as well as interpretability issues. Subsequently, the control, or elimination, of the above interference factors becomes crucial when the protein adsorption, or heterogeneous nucleation, dynamics are researched on.

It has been said, already, that controlling the experimental data repeatability is indispensable, when the surface adsorption (or nucleation) of proteins is researched on. That is, by the time any characterization work on protein heterogeneous dynamics is started the procedures to manufacture the substrates and prepare, or test, the protein solutions should have been fully defined. Deceiving repeatability issues would be, thus, satisfactorily eliminated. Highly sophisticated automated equipment, and particle free laboratories are the common measures that are, generally, available to follow valid experimental procedures and ensure data repeatability in bio-nano-technology. Clean rooms, for example, are particle-free laboratories that are used to drastically control the air particle content while working in nano-technologies. These type of laboratories are usually classified according to the number, and size, of particles that are allowed per air volume. The most common clean rooms are the Class 100 clean laboratories, where no more than 100 particles (of 0.5 μm, or larger, size) are allowed per cubic foot of air.

4.2.2 The fabrication of MEMS-substrates for protein adsorption & crystallization by nano-imprinting

The substrates for the crystallization of lysozyme were fabricated from a submicron-patterned silicon (100) wafer. Silicon (Si) is not a conducting element and it is ideal for the construction of semiconductor devices. Silicon wafers are manufactured from mono-crystalline ingots by slicing these into unrefined wafers. The substrates for this work have been manufactured from a processed 6 inch large and 600 μm thick wafer. The clean silicon wafer has been first spin coated with an epoxy-polymer solution, which was prepared according to the

Obducat procedure, and, thereafter, sub-micron patterns have been shaped on it by another validated imprinting procedure in the Obducat clean rooms (Obducat ltd ©, 2010). Epoxy resins are thermosetting polymeric materials that cure irreversibly after exposure to heat (i.e., at temperature values that are characteristic of each polymer), chemical reactions, or radiations (such as UV). These materials are, generally, liquid before curing and are commonly used in microelectronics to fabricate different components (such as laminated circuit boards, carbon fibre composites, encapsulations, adhesives and other electronic components). The hardening of the epoxy resins, after curing, results from the cross-linking among the polymeric molecules in the resin. When epoxy resins are chemically cured, their flexibility and fracture resistance is tuned by calibrating the concentration of curing additives (such as, aliphatic components or other catalytic salts for cationic polymerization). Also, curing may take place by radiating the polymer only. In so a case the glass transition temperature of the cured material may be lowered by reducing the concentration of the polymer, i.e., its cross linking is limited this way (Carfagna et al., 1997).

The spin coating of silicon wafers (which, in this specific case, was performed with an Opticoat spin coater by SSE, Sister semiconductor equipment) allows the deposition of fine layers of resin. This process starts with dispensing a certain resin volume to deposit it onto the centre of the wafer. Following this, high-speed spinning and drying steps are performed. The amount of the dispensed resin is proportional to the viscosity of the resin solution and the layer thickness that is aimed for. That is, if the viscosity of the resin solution is higher than average, larger amounts may be necessary to make sure that it spreads to the whole wafer, and the spin-coated layer would be also thicker. On this occasion, few millilitres of an epoxy resin solution were spread at 500 rpm and the spin-coated layer was about 56 nm thick (1). The nano-imprint lithography was performed with a PDMS soft stamp in an Obducat Eritre 6 system, which is computer controlled and situated within a Class 100 clean room. The PDMS stamp had been previously embossed from a patterned silicon mask. A silicon mask is a wafer presenting

(1) An NDA (i.e., a non-disclosure-agreement) is in place between the college and the company. As a result of this, no further details can be disclosed on the Obducat patented processes or on the exact chemical structure of the resin-polymer.

a specific pattern (the pattern of this mask had a180 nm pitch, 126 nm height and 55 nm width). Before use, the silicon mask was covered with an anti-adhesion layer via CVD (chemical vapour deposition). This layer is a very thin hydrophobic film, which is made of a Poly-trifluoro-(trifluoro-methyl)-chained silane, and it reduces the interface adhesion between the mask and the PDMS soft material during embossing.

Indeed, given the size of the area to be imprinted, if the above-mentioned solid mask had bee used to imprint the pattern straight into the spin coated epoxy-polymer, almost certainly, this would have induced several non-uniformities within the imprinted patterned layer. As a result of this, the pattern of the silicon mask was, first, replicated onto a PDMS support and cured to form a soft stamp, and, later, the soft PDMS stamp was used to imprint the pattern onto the wafer bearing a spin-coated layer of epoxy-polymer. The flexibility of the soft stamp had been previously calibrated. Indeed, although the flexibility of the stamp primarily depends on the type of polymer that has been used to make it (Viheriälä et al., 2009), the geometric features (or dimensions) of its pattern may also affect this parameter (Schmid et al., 2000). That is, only if an embossing-imprinting procedure has been previously defined the stamp with rubbery consistency can ensure full compliance with the waviness of the silicon wafer. Finally, according to the Obducat procedure, the curable resin was allowed to harden for a few hours (1) at a constant temperature within a previously defined range. That is, a patented two-stage (UV/heat) curing process was, thereafter, used to consolidate the pattern that had been, first, imprinted from the soft stamp onto the spin-coated epoxy-polymer.

The characterization of the nano-patterned wafer before dicing it into MEMS-substrates

The nano-patterned 6 inch silicon wafer was, thereafter, characterized. This characterization was initiated with a Veeco atomic force microscope (i.e., a Dimension 3100) operating in tapping mode. A first set of characterization tests was performed, immediately after fabrication, (that is, in the clean rooms of Obducat ltd), while a second set of tests was

(1) An NDA (i.e., a non-disclosure-agreement) is in place between the college and the company. As a result of this, no further details can be disclosed on the Obducat patented processes or on the exact chemical structure of the resin-polymer.

recorded at a later time in the clean rooms of Toshiba Research Europe ltd. in Cambridge.

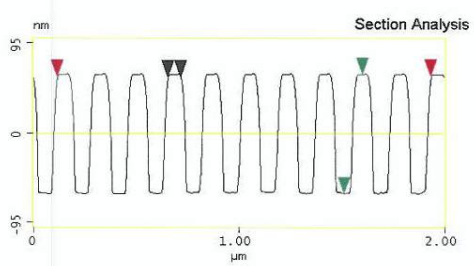
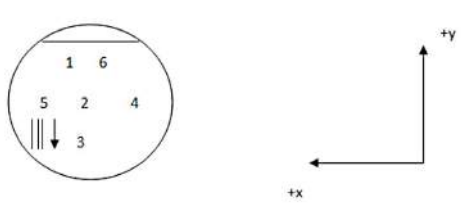


Fig. 4.2 *The pattern of the UV-curable polymer presents a 180 nm pitch, 126 nm height and 55 nm width after the AFM analysis from the Obducat clean rooms, (Obducat ltd ©, 2010).*

This second set of AFM measurements was, also, performed with a Veeco Dimension 3100. The measurements have been performed while sampling 6 (2 × 2 µm) areas in the 6 positions that are described in Fig. 4.3.



File	position	Depth/nm	Period/nm	Average Depth/nm
Snh.000	1	58.35	173.8	58.8
		57.27		
		60.74		
Snh.002	2	62.19	174.2	63
		61.02		
		65.68		
Snh.003	4	61.56	175	61.92
		60.75		
		63.46		
Snh.004	6	59.02	175	61.92
		61.60		
		57.13		
Snh.005	5	59.20	176	59.03
		58.77		
		59.13		
Snh.006	3	53.84	175	53.99
		54.21		
		53.92		

File	Position	Location X/um	Location Y/um	Area/Size	Resolution/lines	Scan Rate (Hz)	Z range (nm)	Set Point (V)	Drive Amplitude (mV)
Snh.000	1	-934	289088	2X2	512X512	1.28	100	1.54	
Snh.002	2	3837	337853	2X2	512X512	1.28	100	1.54	
Snh.003	4	-53386	335324	2X2	512X512	1.28	100	1.39	
Snh.004	5	25443	312221	2X2	512X512	1.28	100	1.40	
Snh.005	6	56376	336641	2X2	512X512	1.28	100	2.52	
Snh.006	3*	3457	278284	2X2	512X512	1.28	100	1.5	

* In this position the wafer was rotated 180*to take the measurement.

Fig. 4.3 *The data relating to the AFM analysis (in tapping mode), from the Toshiba Research Europe limited clean rooms, show that the pattern of the UV-curable polymer has a 175 nm pitch, "60 nm" height and 55 nm width grooves, (Agnese Zicari ©, 2010).*

The AFM equipment is composed of a laser and a cantilever (which is located just above the sample and reflects the laser beam). The reflected laser beam is collected by a position sensitive photo-diode, which transmits the amplified signal to a detector. The detector is in turn connected to a piezoelectric element that holds the sample. A picture of the Veeco Dimension 3100 atomic force microscope may be also observed here below in Fig. 4.4.

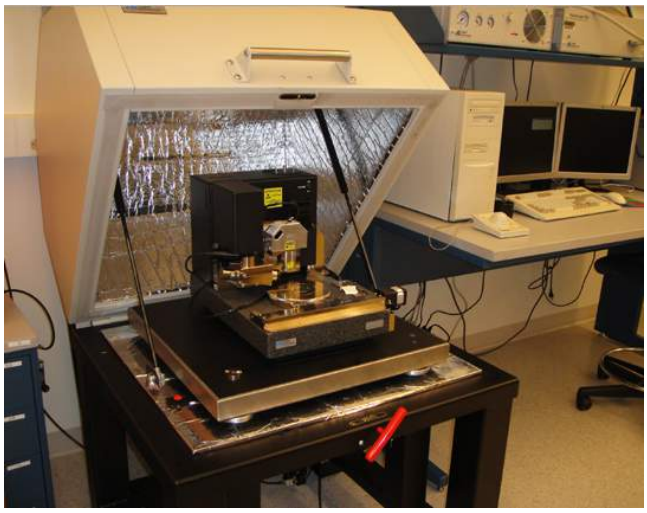


Fig. 4.4 *The Veeco 3100 atomic force microscope.*

The cantilever tips may be of very different shapes and chemistries and, when possible, different types of cantilevers should be used depending on the nature of the sample that is going to be tested. In the first set of measurements focused ion beam probes (FIB-probes) for high resolution tapping mode were made available, whilst in the second set of tests a tapping mode etched silicon probe (model.TESP) was available for use. Hence, a disagreement between the two different sets of experiments was, necessarily, observed for the feature height dimension only. Indeed, the latter was recorded as 60 nm in the second set of experiments. This is, almost certainly, an artefact due to the shape (or chemistry) of the cantilever tip, as cantilevers with different shape (and chemistry) were used in the above experiments. This is well explained in Fig. 4.5.

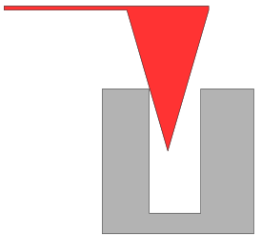


Fig. 4.5 *The height of the features, which was recorded in this second set of experiments, was 60 nm. That is, there is a disagreement between the 2 different sets of experiments for the height dimension only. This different value stems from an artefact of the cantilever tip that was used in this second set of experiments. That is, its geometry (and, possibly, its chemistry) did not allow a real measurement of this dimension. There is a full match, indeed, for all the other dimensions.*

In other words, the AFM tips that have been used in the second set of experiments, probably, did not allow to thoroughly measure the height of the features.

Therefore, surface profilometry was used to ensure the feature height homogeneity all over the wafer while testing the regularity of the wafer bow and polymer layer (Lindroos et al., 2010). The mapping was performed with a mechanical profiler (that is, a Kla-Tencor, P15 surface profiler) in the clean rooms of the Science and Technology Facilities Council in Oxford. Profilometry is an easy-to-perform and quite fast mechanical technique that may be used indistinctively on all types of solid films. However, this technique is not designed for film thickness measurements, and it might present poor repeatability. That is, it is satisfactorily used for approximate measurements on large areas only. On this occasion, all the different scans were performed with a 2 μm size diamond stylus tip (with 45° angle) and forces as low as 20 mN were applied while scanning the wafer. Most of the scans were performed over a 9,000 × 9,000 μm area. Also, the arrangement and coordinates (the centre position coordinates were set to x = –28074.87 and y = + 28636.36) are described in Fig. 4.6.

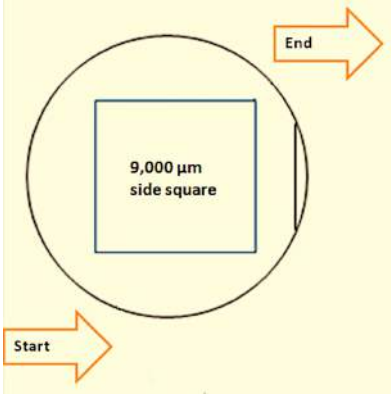


Fig. 4.6 *The scanning pattern that was performed with the Kla-Tencor, P15 surface profiler. The centre position coordinates were x = – 28074.87 and y = + 28636.36, (Agnese Zicari ©, 2010).*

Indeed, 3 series of mapping scans were run in total and 2 of these series were performed on 4 lines each (at a 5000 μm/sec scan speed and a 2000 sampling rate). Given their high sampling rate, these are the lowest resolution scans. The lines have been strategically located to cover most of the surface and the results have been summarised in Fig. 4.7.. In this figure for each scanned line there is a picture with a red arrow indicating its position, while the relating pattern analysis is shown in the picture below it. The scanned lines from the series in (a) show some imperfactions while those from the series in (b) have no detectable imperfections.

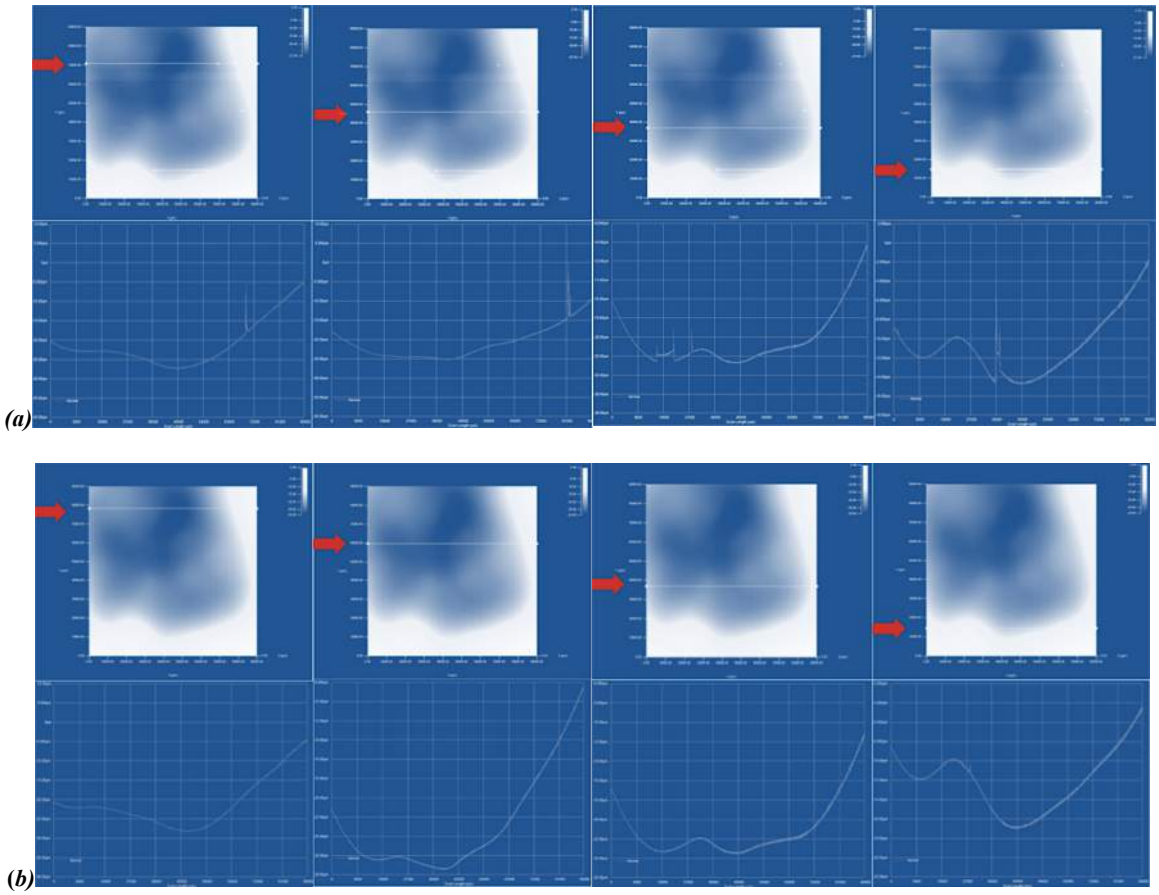
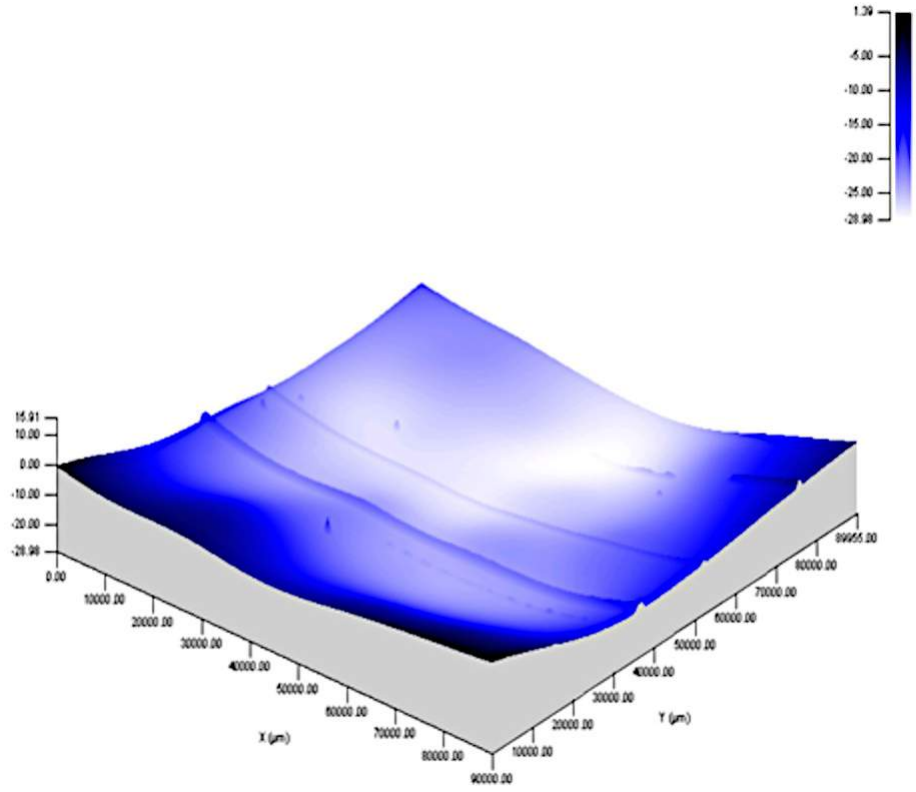
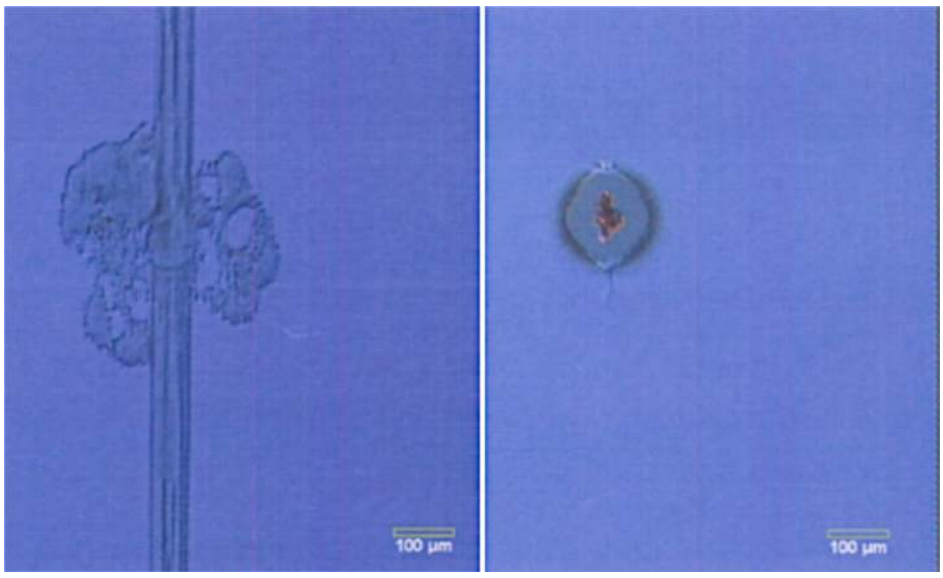


Fig. 4.7 *The 1st series* ***(a)*** *and 2nd series* ***(b)*** *of the 9000 µm line scans. The wafer scans were mapped on four lines each (a red arrow indicates the position of each line).* ***(a)*** *The 1st scan series from left to right: the 1st to 4th line positions (at the top) & relating analyses (at the bottom).* ***(b)*** *The 2nd scan series from left to right: the 1st to 4th line positions (at the top) & relating analyses (at the bottom), (Agnese Zicari ©, 2012).*

The third series of 9000 µm line scans were run on 2000 lines at lower sampling rate (that is, at a 5000 µm/s speed and a 100 sampling rate). That is, this was the higher resolution set of scans and the results relating to it are described in Fig. 4.8 (a). Also, the local wafer imperfections that were observed during profilometry were further characterised by means of a higher resolution technique (i.e., light microscopy). Some microscopy pictures, relating to the imperfections that were observed also via profilometry, have been reported in Fig. 4.8 (b). Additional profilometry tests were thereafter, performed. Indeed, 2 orthogonal single line scans of the wafer were performed to approximately ensure the feature height homogeneity all over the wafer while testing the regularity of the wafer bow to identify any waviness. The latter, indeed, would imply that there is a deformation of the patterned layer.



(a)



(b)

Fig. 4.8 (a) *The 3rd 9000 µm × 9000 µm scan, which is mapped on 2000 lines.* ***(b)*** *The imperfections in the mapped areas were observed also under light microscopy, (Obducat ltd ©, 2010).*

The above-mentioned orthogonal line-scans were performed at a 200 µm/s speed and 50 Hz sampling rate over a 14000 µm length. These were performed in two directions oriented at 90°

to each other. These scans have demonstrated that the wafer has a regular bow in both directions. That is, no irregular waviness of the patterned layer was this way inferable. The scan arrangement and results (i.e., normal) are shown in Fig. 4.9.

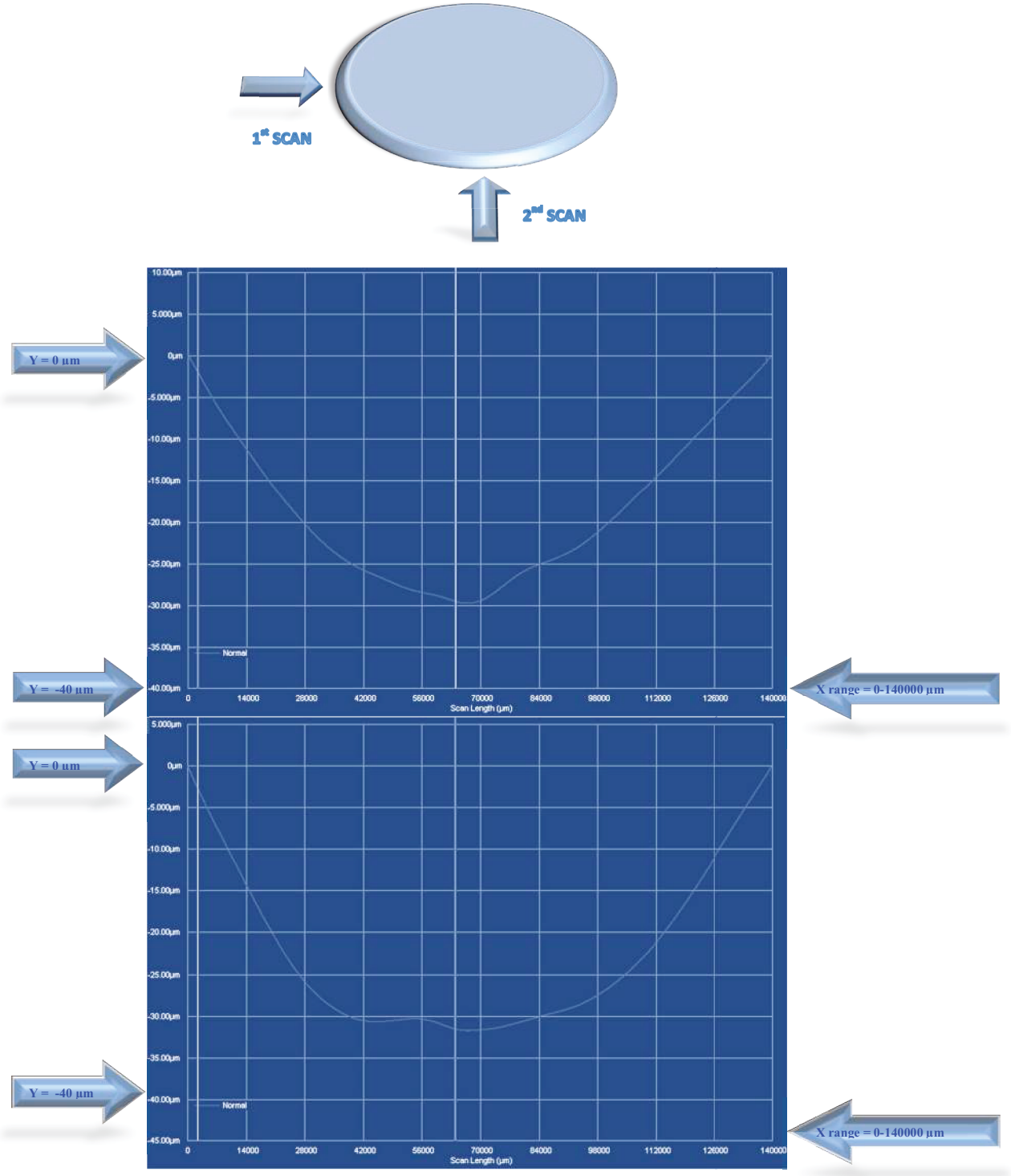


Fig. 4.9 *The measurement of the wafer deformation: no thickness variation or warp were observed. That is, the wafer bow shows regular. The top and bottom profiles represent the 1st and 2nd scan, respectively.*

Stealth-dicing of the patterned wafer into MEMS-substrates

The use of lasers, including the control of its parameters (such as beam power, focal length and cutting speed) to process materials of different nature has been well known since the end of the last century (Tam et al., 1992). Laser dicing techniques are commonly used to cut silicon wafers and produce MEMS. However, this method is subject to a number of concerns such as the possibility that it might cause temperature-induced surface delamination of the MEMS' patterned layer and produce excessively contaminating debris (Kim et al., 2007). A number of studies have been performed to minimize the above issues. These have shown that Nd:YAG lasers permit the accomplishment of stealth-dicing (i.e., heat induced) cutting methods. Indeed, these methods have proven uniquely efficacious to reduce both damage and contamination due debris, (Izawa et al., 2004).

Hence, after manufacture and characterization of the patterned silicon wafer, a specific dicing technology was used to dice it into 5 × 5 mm square substrates. Before leaving the clean rooms, the wafer was mounted on a flat 7 inch side and 5 mm thick glass sheet by means of an anti-stick tape. A stealth dicing method was, therefore, performed in the laboratories of the Manufacturing Engineering Centre in Cardiff, and the above pre-dicing procedure has been performed to avoid the contamination of the patterned surface. An HM1400 laser equipment by GSI Lumonics (Nd:YAG, 75, 40 or 20 W power, and $\lambda = 1064$ nm) was used to perform the wafer cut. The above-mentioned equipment while in use and the calibration procedure, which was accomplished right before starting the dicing, are shown in Fig. 4.10.

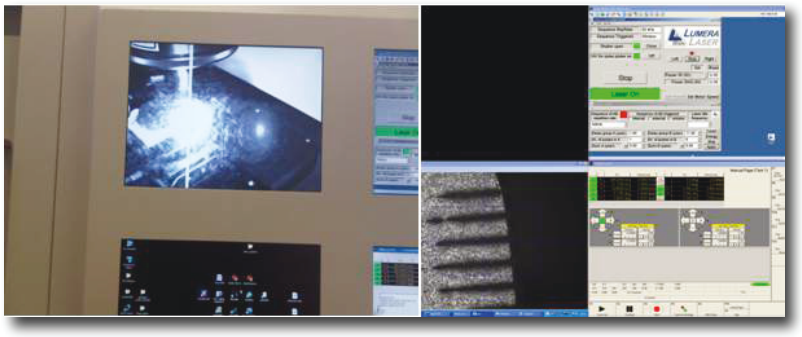


Fig. 4.10 *The HM1400 by GSI Lumonics, in the manufacturing engineering centre in Cardiff, (left). The method calibration lines, that were performed on a 600 μm thick spare wafer, are shown (right).*

The design for dicing the master wafer is shown in Fig. 4.11.

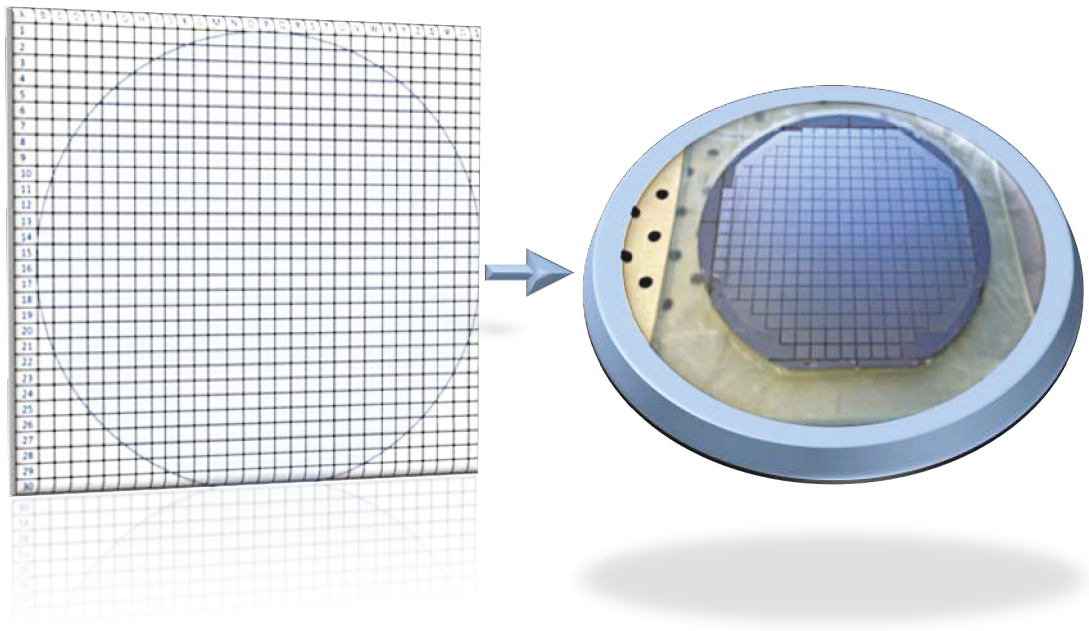


Fig. 4.11 *The dicing arrangement to detect the defective sections (left). A picture of the diced wafer is also shown (right), (Agnese Zicari ©, 2010).*

The laser cut was performed from the back side of the wafer down to 2/3 of its thickness. This, also, has permitted to minimize the delamination and hold the debris. The appearance of the different cut sections, which includes the polymeric layer visible on the top of it, is shown in Fig. 4.12.

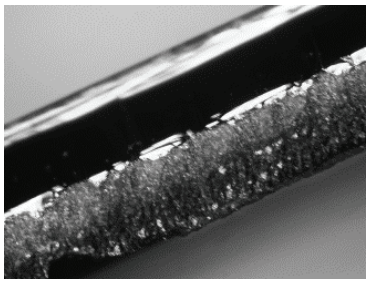


Fig. 4.12 *The edge of the silicon wafer chips after dicing, (Agnese Zicari ©, 2010).*

After stealth dicing the substrate stability to delamination was also tested after O_2 plasma activation and exposure to saline wet conditions. Indeed, the samples were, first, treated with very mild O_2 plasma and exposed to the new precipitant solution for 24 hrs, afterwards. The

samples were then examined with a ZEISS scanning electron microscope, and the results are displayed in Fig. 4.13. In the picture (a) of this figure it is observed that, after manually splitting the substrates from the diced wafer, one sample shows some interruption of the patterned polymeric layer before reaching the edge of the sample. Though, the pattern has no alteration. Moreover, in the picture (b) a different sample, which, instead, has been tested after that both the above-mentioned stress conditions have been applied, presents no change in the features of the polymeric pattern.

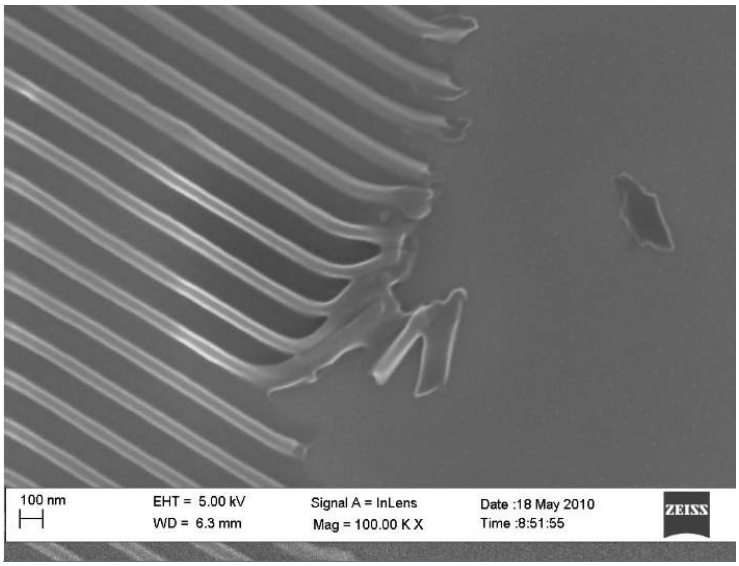


Fig. 4.13 (a) *The top scan was taken on the sample a without treating it with the oxygen plasma.* ***(b)*** *The bottom scan was taken on the sample b after treating it with both the oxygen plasma and the precipitant solution, (Agnese Zicari ©, 2010).*

4.2.3 The fabrication of NEMS-substrates for protein adsorption & crystallization by interference lithography

As a general rule, the "writing rate" of direct writing techniques on large areas is too slow if the fabrication of very narrow patterns is aimed for. As a result of this, the fabrication of wide narrow-patterned areas in nano-patterning research becomes non-feasible or impossible unless step & repeat lithography techniques are used to overcome this major problem. Indeed, step & repeat lithography methods, generally, consist of repeating a small area into larger areas. The method in this work starts with an interference lithography step that involves the use of a patterned diffraction grating system and two or more coherent light beams. That is, a beam of EUV (i.e., extreme ultraviolet) coherent light is generated from a synchrotron radiation source, which produces wavelengths down to about 10 nm, and it is split into two or more beams by means of a diffraction grating system. The diffracted coherent light beams recombine, thereafter, to produce an interference pattern on a spin coated layer of a silicone-based photoresist (which is similar to those that are commonly used in optical lithography), (2). Thanks to this method the interference pattern, which is produced on the photoresist and presents very fine features, may be straightforwardly repeated into larger areas (Hesch et al., Moser et al., and Dattoli et al., 2001).

In this work the NEMS substrates were prepared in the clean rooms of Eulitha ltd. (Paul Scherrer Institute, Switzerland) using transmissive type diffraction gratings, (2). Each diffraction grating has been manufactured from a 100 nm-thick silicon nitride (Si_3N_4) membrane after, first, covering it with a thin film of chromium (Cr) via CVD and, then, spin-coating it with a 40 nm-thick layer of poly-methyl-methacrylate (PMMA). After e-beam lithography and development, the pattern was etched to form diffraction transmissive gratings with ≈ 140 nm period grooves. These gratings were, thereafter, used to form EUV (that is, 13.4 nm) exposed patterns of about 45 − 52.5 nm periods into the layer of silicone-based negative resist. The EUV exposure was performed in the clean rooms of the EUV station

(2) An NDA (i.e., a non-disclosure-agreement) is in place between the college and the company. As a result of this no further details can be disclosed on the Eulitha ltd. step & repeat lithography processes.

in the Swiss Synchrotron Radiation Centre, (Solak et al., 2002; Auzelyte et al., 2009). NEMS, with the specifications in Fig. 4.14, have been fabricated accordingly.

Material	*silicon*
Slide thickness	*675 μm*
Slide size	*25x25 mm²*
Slides/Fields	*9 slides with 9 fields per slide*
Field size	*each filed of 200 x 200 μm² with ≈ 53nm dots*
Feature size	*half-pitch: 53nm* *dot size: 45-65nm*
Feature height	*50 nm*
Feature uniformity	*+/- 5%*
Fields' distance	*about 2 mm*

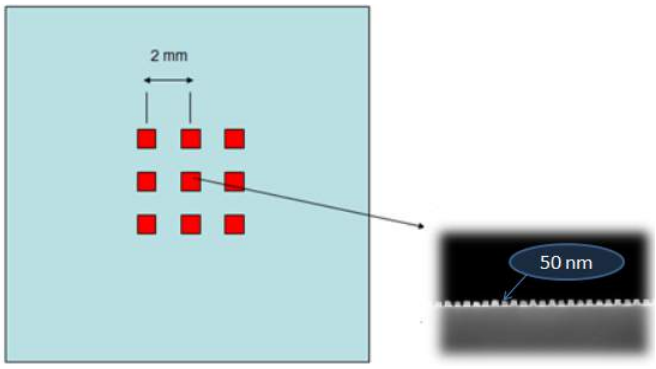


Fig. 4.14 *The description and representation of the pattern specifications, (Eulitha ltd ©, 2010).*

4.2.4 The modification and characterization of MEMS & NEMS surfaces

Hydroxyl-terminated surfaces, such as silicon surfaces, are ideal substrates for surface chemical modification reactions. Indeed, these, after activation of their hydroxyl groups, may be reacted with silanes of different chemistries to form an organic monolayer of Si–O–Si–C bonds. Further, the intrinsic topographical structure of the surface is, usually, retained when the above-mentioned reaction is performed via vapour phase techniques. Generally, this is enough to hinder possible polymerization side-reactions. That is, silanization via CVD is often regarded as the most suitable method to modify the surface chemistry of the nano-patterned (or submicron-patterned) surfaces of NEMS (or MEMS) substrates. In this work, CVD equipment was not available and wet surface reactions were performed, instead, on both the MEMS and plain silicon surfaces. Different silanes (such as 3-aminopropyl-triethoxy, 3-mercaptopropyl-trimethoxy, trimethoxy-trifluoro-propyl, methyl-trimethoxy and 3,4-epoxy-cyclohexyl-ethyl-trimethoxy substituted silanes) were used to modify the substrate surfaces. Indeed, some of these surfaces are commonly used for different purposes, such as the induction of protein adsorption or crystallization, and the manufacture of biomaterials. Biomaterials, in fact, are, generally, manufactured by immobilization of proteins onto silanized surfaces.

The MEMS in section 4.2.2 were silanized with the 3,4-epoxy-cyclohexyl-ethyl-trimethoxy substituted silane, after activation. The activation and the silanization reactions were accomplished on these substrates by combining wet and vapour phase activation methods together with wet and vapour phase silanization methods. It has been pointed out in the previous paragraph, already, that, although no chemical vapour deposition (CVD) equipment was available for this work, vapour phase techniques are strongly recommended to chemically modify MEMS & NEMS substrates. Nevertheless, surface wet activation protocols were investigated, first. Indeed, in order to reduce the relating surface roughness increase, specially formulated piranha solutions and suitably ranked activation protocols were utilized. These are both well described in Tab. 4.1, (Angermann H. et al., 2000).

Tab. 4.1 *The description of the piranha activation protocol, (Agnese Zicari ©, 2009).*

Activation Protocol	**Solution**	**Conditions (Temperature °C/Sonication)**	**Time (min)**
Step 1	Mixture of 30 % hydrogen peroxide (30 % water solution) and 70 % sulfuric acid (concentrated solution)	60 / Yes	30
Step 2	Hydrochloric acid (37 % water solution)	RT	60
Step 3	Mixture of 10% hydrochloric acid (37 % water solution), 10 % hydrogen peroxide (30 % water solution) and 80 % distilled water	80	30
Step 4	Mixture of 10 % ammonium hydroxide (28 % water solution), 10 % hydrogen peroxide (30% water solution) and 80 % distilled water	80	30
Step 5	Ammonium hydroxide (28 % water solution)	RT	15
Step 6	Drying	RT	2 – 3

After wet surface activation the surface silanization reaction was tested, either with an in-house CVD (using a furnace at 340 °C and a Petri dish) or a high-speed mixed wet reaction (which was performed at 40 °C instead). Curing after reaction, was, also, performed for 10 hrs at 120 °C in a vacuum oven. Nevertheless, the in-house CVD method did not produce homogeneously distributed surface chemistries. Indeed, contact angle measurements (CA), which were taken with a Kruss Drop Shape Analysis System DSA (and 10 – 12 μl drops), did not produce similar values over the different surface sections of the same sample. That is, average contact angle values in the 40 – 80° range were recorded.

On the other hand, a second protocol, which involved the use of an oxygen plasma treatment followed by a high-speed-mixed wet reaction, was also investigated. This protocol, also, involved a silanization reaction at 40 °C and a 10 hr post-reaction curing at 120 °C. The latter protocol, by contrast, produced fairly homogenous average values of internal contact angles (i.e., ≈ 80°). Almost certainly, the advantage of the above-mentioned protocol is the plasma surface activation step. That is, plasma is a stable vapour phase and it homogenously activates all the surface hydroxyl groups, without changing the surface roughness. Indeed, plasma is made of oxygen molecules that become ionized after that these have been exposed to UV radiations under vacuum. Also, the plasma equipment is usually arranged so that the ionization takes place in a different compartment. Indeed, since the freshly ionized oxygen molecules are, often, unstable, and over-reactive, free radicals may damage the sample surface. The above equipment arrangement, allows the ionized oxygen molecules to recombine in the ionization compartment before diffusing onto the sample surface. In this work, different types of equipment were used to investigate this effect, that is, a K1050X plasma asher and a Diener plasma cleaner & etcher. Since the asher was not made available by the Imperial College department of physics, the plasma cleaner by Diener electronics-DE (40 kHz, 100 W, operating at 0.6 bar) was used in the end. Also, AFM analyses of the activated samples were conducted in contact mode (with MPP silicon probes) before and after surface plasma activation and no significant increase in the surface roughness was observed. This was, especially, observed when the sample surfaces had been activated with the K1050X plasma asher.

After activation, the silanization reactions were performed in a specifically designed reactor where the reactive silicon surface was supported upside down and high-speed mixing was applied from below the sample with a regular magnetic stirrer. This arrangement has ensured no significant increase in roughness and an homogeneous degree of substitution. Indeed, post-reaction characterization tests, which were performed with an AFM Veeco diInnova in contact mode (with silicon nitride triangular probes) and Kruss equipment, have confirmed this. As shown in Fig. 4.15 (a), after reaction, a typical average contact angle (CA)

of 80.3° was recorded over the different epoxy-surface sections. Also, some of these samples were treated again with oxygen plasma, after reaction, as shown in Fig. 4.15 (b), and cured, once more, in a vacuum oven (for 2 hrs at 120 °C). In this instance, there was not a recovery of the original value (i.e., 80.3°). Very probably, this is due to the corrosion of the silanized layer.

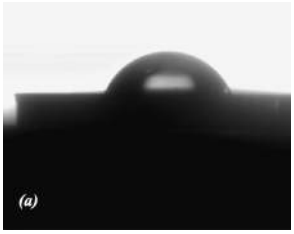


Fig 4.15 (a) *The CA (80.3°) of the epoxy-surface after reaction, on the left, while, on the right* ***(b)****, the silanized epoxy-surface has been treated, once more, with oxygen plasma (CA 9.8°). When the latter was stored in a vacuum oven (for 2 hrs at 120 °C) there was not a recovery of the original contact angle in (a), (Agnese Zicari ©, 2009).*



Also the patterned epoxy-surfaces were cleaned and activated via oxygen plasma according to the above protocol. The average contact angle values before and after the oxygen plasma treatment were of 72.9° and 13.6°, respectively. This is, also, shown in Fig. 4.16.

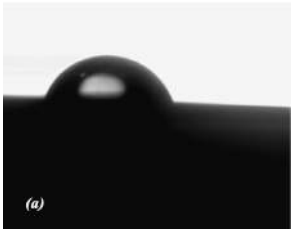


Fig. 4.16 (a) *The patterned epoxy-surface on the left (CA 72.9°) and* ***(b)*** *the patterned epoxy-surface after plasma treatment on the right (CA 13.6°), (Agnese Zicari ©, 2009).*



Also, the epoxy-patterned surfaces were further tested for stability (i.e., delamination), that is, these were exposed to different cleaning protocols and wet conditions (that is, the precipitant solution for 24 hrs). After cleaning, plasma treatment and exposure to the precipitant solution, the patterned epoxy-surface was cured again under vacuum (for 2 hrs at 120 °C). Subsequently, the average contact angle value reverted to a value that is close to the original value (i.e., 80.8°). The reversibility of the contact angle value would indicate that the above protocol has no irreversible effect on this surface. One of the CA measurements is shown in Fig. 4.17.



Fig. 4.17 *The surface was treated under vacuum (and temperature) after cleaning, plasma treatment and exposure to the precipitant solution. The contact angle was found reverted to a value close to the original value (CA 80.8°), (Agnese Zicari ©, 2009).*

The epoxy-patterned samples were also tested under optical microscopy. Optical microscopy makes use of a set of lenses to magnify and resolve images, and its resolution may go down to about a couple of hundred nanometres. In optical microscopy the magnification depends on the number of lenses, while the resolution depends on the ability of these lenses to gather light. Signs of delamination were observed only at the edge of a patterned sample. Indeed, the DiInnova AFM analysis and SEM analysis (JSM-6400-fixed with Oxford Instruments INCA energy dispersive system) of the above samples confirm that, after plasma treatment, the pattern, apart from its edge, is still intact and this is shown in Fig. 4.18.

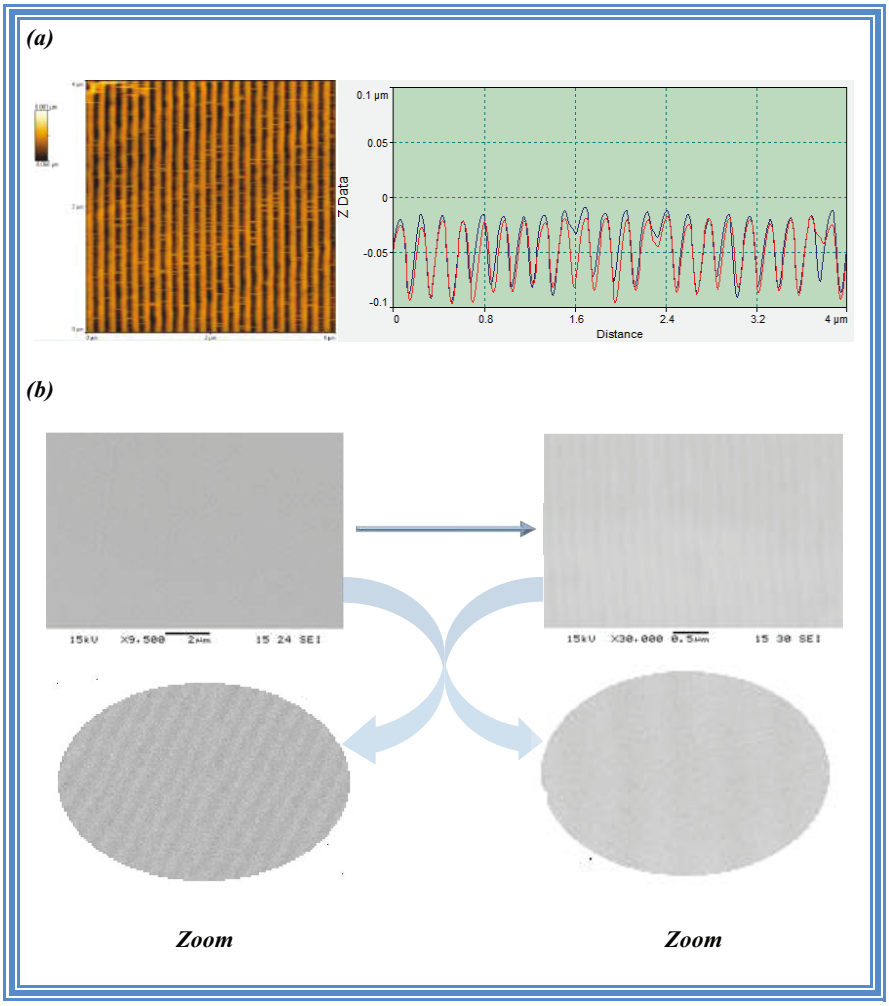


Fig. 4.18 *The AFM & SEM analysis of the sub-micron pattern after cleaning, oxygen plasma treatment and exposure to the precipitant solution.* ***Top (a)****: the AFM analysis. Left; the analysis of a 4µ square area. Right; the Z-axis values showing the intact pattern (the height dimensions show altered due to the tip size).* ***Bottom (b)****: the SEM Analysis. On the left; the picture of the pattern after plasma treatment only. On the right; the picture the pattern after performing all the 3 above steps, (Agnese Zicari ©, 2010).*

With respect to the previously mentioned NEMS, some of the silanization reactions (i.e., those with the 3-aminopropyl-triethoxy, 3-mercaptopropyl-trimethoxy, methyl-trimethoxy and 3,3,3-trifluoropropyl-trimethoxy substituted silanes) were, first, validated on plain silicon surfaces. After reaction with the above-mentioned silanes, some of the samples presenting contact angle values discrepant from those in the literature, were also characterized by means of x-ray photoelectron spectroscopy (XPS) and ellipsometry techniques. In 1978, Brundle and Baker described XPS as a quantitative technique that is primarily used to measure the elemental composition of a solid surface. This can be used to measure the chemical composition and the electronic state of the elements that exist within the surface of solid matter (i.e., up to 10 nm away from the surface). In this technique, the surface is irradiated under high vacuum with an x-ray beam that causes the ejection of electrons. Once the electrons have been ejected from the irradiated surface, their kinetic energy provides information about the surface atomic composition. Indeed, the binding energy (E_B) of the photoelectrons can be, indeed, obtained from the measured kinetic energy (E_K) according the Planck-Einstein equation (4.1).

$$E_K = h\nu - (E_B + \varphi) \qquad (4.1)$$

where h is the Planck constant, ν is the linear frequency and φ is a work function (which depends on the spectrometer and material). Fig. 4.19 shows a sketch of the XPS phenomena.

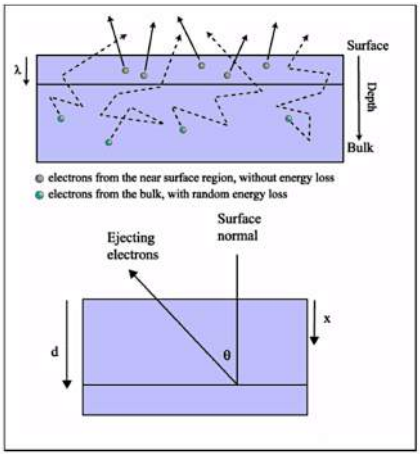
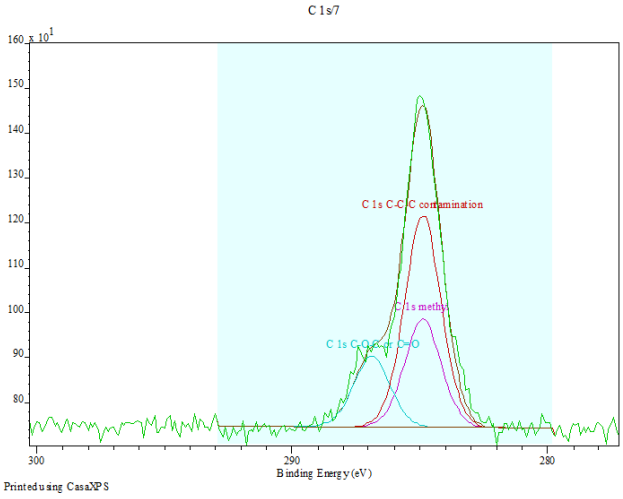


Fig. 4.19 *The XPS technique measures the kinetic energies of the emitted photoelectrons. After that the photoelectrons' energy has been measured, the binding energies of the photoelectrons are calculated according to the Planck-Einstein equation. This in turn allows to, quantitatively and qualitatively, describe the atomic composition of the sample surface, (http://www.phy.cuhk.edu.hk/course/surfacesci/mod3/m3_s1.pdf).*

Nevertheless, the XPS technique is a partially destructive analysis, as damages may well occur during x-ray exposure. Indeed, it is not advisable to reuse the sample, after that it has been exposed to x-rays (Baer et al., 2003).

The x-ray photoelectron spectroscopy measurements, for this work, were performed by means of a Kratos AXIS ULTRA x-ray photoelectron spectroscopy instrument. The XPS measurements relating to the samples that have been prepared according to the procedures from chapter 6 are displayed in Fig. 4.20. That is, in this figure, the XPS measurements relating to the samples that have been reacted with the 3,3,3-trifluoropropyl-trimethoxy and methyl-trimethoxy silanes samples are compared. It is, thus, observed that the degree of substitution for the fluoro-propylated surface, is less than that for the methylated surface. Also, it is supposed that this is, mainly, beacuse of the highly hydrophilic nature of the reaction solution that was used to perform the silanization reactions according to the procedure β, which is described in section 6.3.4. Indeed, in the specific case of the 3,3,3-trifluoropropyl-substituted silane, given the highly hydrophobic nature of its fluorinated side-chain, no further reaction in wet conditions occurs once the surface hydrophobicity has increased up to a certain value. That is, once the substitution has progressed up to a certain degree, there is no more sufficent contact between the reacting silane solution and the remaing hydroxil groups on the solid surface.



	Sample 1	Sample 1
O 1s	30.9	29.6
C 1s methyl	5.0	13.5
C 1s contamination	12.4	11.9
Si 2p	51.7	44.9
Na 1s	0.1	0.2
	Sample 2 Dark	Sample 2 light
O 1s	26.2	27.1
C 1s methyl	2.9	4.8
C 1s contamination	21.7	20.1
Si 2p	49.1	47.9
Na 1s	0.2	0.1
	Sample 3 Dark	Sample 3 light
O 1s	21.3	21.5
C 1s methyl	34.1	34.3
C 1s contamination	24.4	19.7
Si 2p	18.4	22.6
Na 1s	0.1	0.1
F 1s	0.5	0.9
Ca 2p	1.2	1.0

Fig. 4.20 *The XPS analysis of some silanized substrates. Sample 1 and 2 have been methyl-trimethoxy silane treated, while sample 3 has been 3,3,3-trifluoropropyl-trimethoxy silane treated. Sample 3 shows very little fluorine content, that is, it shows very little degree of substitution when it is compared to sample 1 and 2.*

Ellipsometry, on the other hand, is a non-distructive surface technique which is commonly used to measure the change in light polarization when this reflects and transmits from a solid surface. For optically isotropic structures, ellipsometry is performed at oblique incidence. In an oblique incidence setting, if the incident light is linearly polarized with the electric vector (*p*) parallel and the magnetic vector (*s*) perpendicular to the plane of incidence, the reflected light will, also, be *p* and *s* polarized. The reflected light is, usually, elliptically polarised and the parameters that are used to define its degree of polarization are the amplitude ratio (Ψ) and the phase difference (Δ). The change in these two parameters depends, not only, on the intrinsic optical properties of the solid material (which constitutes the solid surface), but also, on the thickness (and type) of film, which this surface has been previously coated with. Ellipsometry data are usually expressed by means of the ratio of two different reflection parameters R_p and R_s. Their ratio can be also correlated to the wavelength shift according to the following equation.

$$\rho = \frac{R_p}{R_s} = Tan\psi \, e^{j\Delta} \qquad (4.2)$$

where ρ is the ratio of the complex reflection coefficients, ψ is the relative amplitude attenuation and Δ is the differential phase shift.

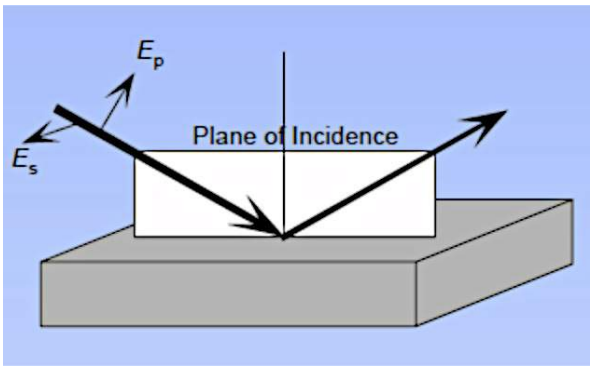
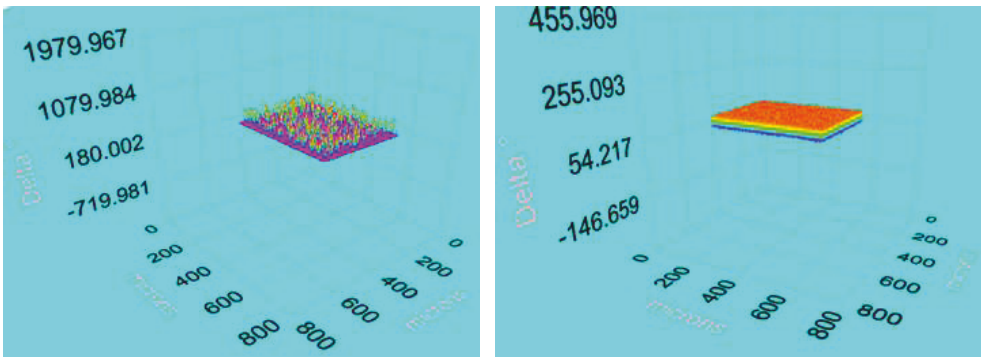
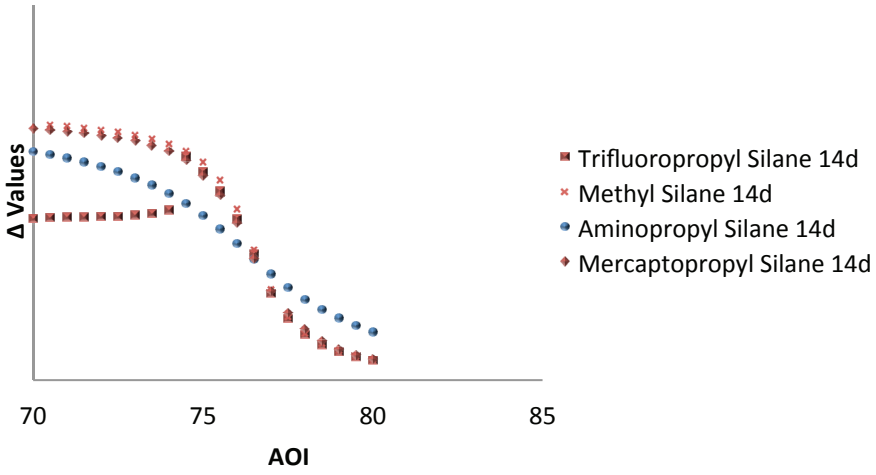


Fig. 4.21 *A representation of the ellipsometric analysis: it measures the change in the polarization state of light after reflection from the surface of a sample. The polarized light, once this has been measured, can provide information relating to the substrate material optical properties or the thickness of any layer that has been deposited on it, (http://www.aps.org/units/fiap/meetings/presentations/upload/tompkins.pdf).*

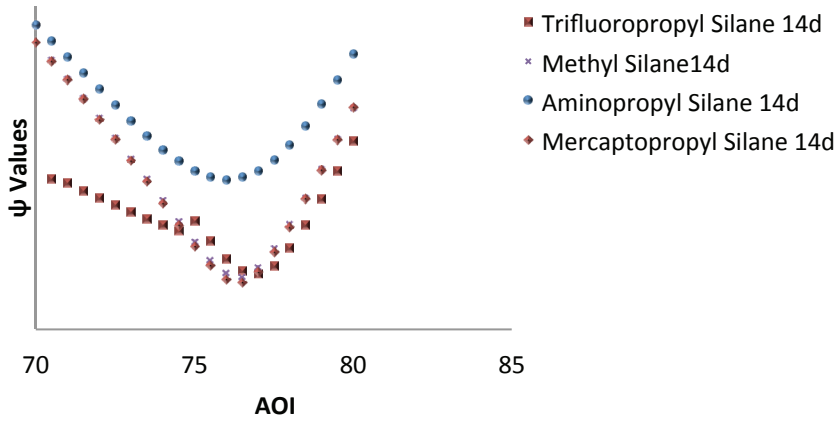
The ellipsometry tests were performed with an ellipsometer EP3-v230, provided with a 532 nm laser source and white light source. An initial *AOI* (angle of incidence) of about 60° was set in these tests. The left picture of Fig. 4.22 (a) shows the ellipsometric analysis of the amino-silane treated surfaces, while the right picture of Fig. 4.22 (a) shows the ellipsometric analysis of these surfaces after 14 day exposure to the sodium chloride solution with the crystallising precipitant concentration. The latter shows a certain surface layering, which suggests that the above-mentioned precipitant solution is not suitable to characterize the adsorption and crystallization of lysozyme. That is, the surface adsorption of the precipitant salt may interfere with (and alter) the adsorption, or heterogeneous nucleation, of the lysozyme molecules. Indeed, both the plots in Fig. 4.22 (b) show that the Ψ and Δ values of the tested surfaces look extremely similar after 14 day exposure to the precipitant solution.



a)



b$_1$)



b₂)

Fig. 4.22 *Ellipsometric analysis of the delta (Δ) and psi (Ψ) parameters at different angles of incidence (AOI).* ***a)*** *The profile of the delta values for the 3-aminopropyl-triethoxysilane treated surfaces at Time = 0 (left) and after exposure to the original precipitant solution, Time = 14 days (right).* ***b1) & b2)*** *The profiles of the Δ and Ψ values for the 3-aminopropyl-triethoxysilane, the 3-mercaptopropyl-trimethoxysilane, the 3,3,3-trifluoropropyl-trimethoxysilane and the methyl-trimethoxy silane treated surfaces after exposure to the original precipitant solution for 14 days (Agnese Zicari ©, 2009).*

The contact angle analysis has confirmed that the surface modification via wet chemistry can produce a satisfactory surface coverage only when silanes, such as the 3-aminopropyl-triethoxy silane, 3-mercaptopropyl-trimethoxy silane and methyl-trimethoxy silane, are contemplated. While, this is more difficult with silanes such as the 3,3,3-trifluoropropyl-trimethoxy silane, as this forms much more hydrophobic surfaces, when the same degree of surface substitution as other silanes' has been reached. In the literature the 3-aminopropyl-triethoxy silane monolayer has a typical contact angle value that lies between 38° and 44° (Zeng et al., 2011), while the 3-mercaptopropyl-trimethoxy silane's lies between 57° and 70° (Kurth et al., 1993; Li J.et al. 2009). In these experiments average contact angle values up 80° were obtained for both the 3-aminopropyl-triethoxy and the 3-mercaptopropyl-trimethoxy silane treated surfaces. On the other hand, while in the literature a contact angle of 153° has been obtained, after CVD reaction, on 3,3,3-trifluoropropyl-trimethoxy silane surfaces, in this work an average contact angle value that lies between 80° and 100° was, necessarily, obtained via wet chemistry. Most of the above-mentioned contact angle values have been averaged and summarized in Tab. 4.2.

Tab. 4.2 *This table summarizes the average CA values for the different silanized surfaces, (http://www.gelest.com).*

Silane	CA by Literature	CA produced
3-aminopropyl-triethoxy-silane	**38° – 44°**	**80°**
3-mercaptopropyl-trimethoxy-silane	**57° – 65°**	**80° – 90°**
3,3,3-trifluoropropyl-trimethoxy-silane	**153°**	**80° – 100°**
methyl-trimethoxy-silane	**90° – 100°**	**80° – 90°**

As previously stated, some of the above average contact angle (CA) values have been recorded differently from the literature. That is, the hydrophilic and acidic silanizing solutions do not allow the reaction to proceed further on surfaces with a given degree of hydrophobicity. Indeed, no real amelioration of the degree of substitution was observed, even, after the use of an effective mixing method, which would confirm that once the surface degree of hydrophobicity has increases up to a certain value no more amelioration of the surface degree of substitution is obtainable. Nevertheless, the use of mixing, during wet chemistry reactions, has, proven to ameliorate the surface roughness homogeneity. More homogeneous roughness values were, in fact, observed over the sample surfaces, once simple high speed stirring had been applied (some of the measurements relating to this have been concisely summarized in chapter 6).

As a result of this, it has been concluded that only the use of CVD (i.e., anhydrous silane reaction via chemical vapour deposition) can systematically reduce any unwanted inter-sample or intra-sample variability. The sketch in Fig. 4.23 explains the advantage of performing anhydrous silanization reactions, instead of wet reactions, on silicon surfaces.

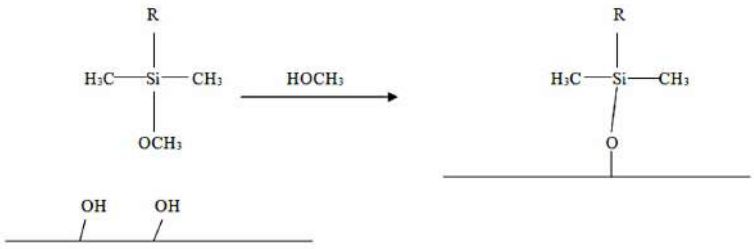


Fig.4.23 *A representation of the anhydrous deposition of silanes, (Agnese Zicari ©, 2010).*

CVD methods are, commonly, used to deposit compact solid coatings. The deposition of chemicals is often used to modify semiconductor surfaces in the semi-conductor industry or produce other industrial high performance coatings. The deposition of chemicals on active surfaces is usually performed in a modern reaction chamber. This looks very similar to an oven, where one or more volatile compounds react with the activated substrate, at specific conditions, to form a layer of a well-defined thickness. Also, a number of specific parameters are controlled by means of a computer interface to tune the thickness of this layer. Moreover, volatile (and, often, toxic) gases are usually produced during a CVD process and these must be disposed of through an appositely designed outlet. More specifically, the equipment, which is used to perform this type of experiments, is, usually, made of a closed chamber, to place substrates, and a reservoir for the chemical that is going to react with the functional groups of the activated substrate surface. The reservoir is heated and the chemical is allowed into the chamber only once a certain vapour pressure value has been reached. Generally, the use of CVD to react silanes with an activated surface, requires silanes with vapour pressures greater than 5 torr at 100 °C. This ensures that the monolayer deposition is favoured over any other possible polymerization side reaction. However, suitable conditions to vapour-apply other silanes may be further defined also for most of those silanes that, usually, are not commercially used to perform surface deposition reactions.

Chapter 5

Crystallization Trials

5.1 Introduction to the Crystallization Trials: heterogeneous adsorption and nucleation

It has been specified already in section 3.1.3 that proteins, differently from small molecules, are subjected to misfolding and unfolding. The latter, very probably, induces high interrelations among all the factors that govern protein adsorption or nucleation, and complicates the understanding of the related molecule grouping dynamics. Indeed, as the initial stage of monomer folding is mainly driven by hydrophobic interactions, all the solution conditions that influence the solvent structuring dynamics may indistinctively, or at turns, become the driving force to their amorphous clustering or nucleation. Indeed, in the above-mentioned section, the nucleation initiation stage has been conceptually described with a meta-stable phase model. According to this model, the solution forms a fluctuating leopard pattern of locally fluctuating concentrations with a characteristic lifetime and amplitude. That is, just before nucleation, unstable and metastable behaviours critically compete in generating a broad range of energy minima. Consequently, solution parameters (such as pH, temperature, protein and co-solute types as well as their nominal concentrations) may be calibrated to favour some of these energy minima over the others. This model may be regarded as a fair representation also of the hen egg white lysozyme (HEWL) metastable region as, in section 3.1.3, this has proved to promptly depend on nominal, or local, solution factors (Debenedetti, 1996). Similarly, the ripening and heterogeneous nucleation phenomena at the protein crystal (or inorganic) interface, may well generate from the above-mentioned fluctuations under the influence of local solution factors (including the presence of a solid-liquid interface, or its features). It is, in fact, well known that the presence of a solid-liquid interface enhances

the protein nucleation dynamics and, very probably, favours some of the bulk solution energy minima over the others. It is well known, in fact, that protein heterogeneous processes are thermodynamically favoured over homogeneous', (Tsekova et al., 1999).

According to the classical theory, the clustering of proteins has been often described as a thermodynamically and statistically driven first order phase transition. Nevertheless, this transition is proportional, not only, to the local solute concentrations, but also, to the local values of other nominally defined factors. In fact, while according to the classical theory, nucleation, primarily, occurs when the solution supersaturation is at equilibrium, according the recent metastable phase model, structuring occurs once a specifically defined pattern of fluctuating concentrations (and, therefore, local energy minima) has been achieved. This is, probably, also where the local mass fluctuations' lifetime, or amplitude, values are close enough to each other to allow for specific intermolecular interactions.

The classical models for homogeneous nucleation have often been used, also, to explain heterogeneous nucleation phenomena. However, the adsorption or structuring processes at the solid-liquid interface are, also, governed by additional factors such as the solid-solution interface energy and the molecule anisotropic chemistry or conformational activity. That is, the conventionally regarded factors (i.e., the nominal solute concentrations and solution ionic strength) might be, periodically, blurred by the local interactions among the protein monomers, the interface and the solution. In fact, for small crystals, the growth rate has been regarded as distinctly proportional to the local solute concentration gradient in the boundary layer (that is by the crystal-liquid interface). Nevertheless, this effect tapers off when the crystal linear size increases (Pusey, 1986). That is, for small enough crystals it is observable that local concentration fluctuations may combine to govern the crystal growth. Differently, when the crystal size increases, the non-combined local fluctuations can, only, locally define the nucleation dynamics, and pattern, at the crystal-liquid interface. In other words, the heterogeneous and homogeneous dynamics would be highly interrelated.

Similarly, in section 3.1.2, it was reported that the thermodynamic energy barrier for surface aggregation (or nucleation), results from the combined effect of the protein monomers' diffusion to the solid-liquid interface, and their actual adsorption onto it. That is, one or both stages may be rate limiting for the whole surface aggregation process, as it has been experimented and modelled that protein adsorption kinetics do not depend on local concentration gradients only. That is, this is not a diffusion related process only. A possible explanation for this is the solution-dependence of the conformational structure of the protein monomers, since the protein molecule conformations respond, more or less broadly, to the solution environment. Also, the anisotropic chemical structure, or morphology, of protein molecules may promptly trigger additional responses to local solution factors (especially when these have steric features too). A surface, for example, has steric features. Moreover, the adsorption of the protein monomers onto an interface may determine a series of local changes in the interface chemical potential and form a pattern of chemically active patches within the adsorbed layer. These patches may either trigger new governing parameters or alter the relative importance of the parameters that have initiated the adsorption process. That is, the adsorption of protein monomers is, mainly, driven by the evolving interplay of local factors, such as the type of protein molecule, solid surface, solvent (or other co-solutes), and their concentration.

The above dynamics are a possible explanation for the delayed changes in interface tension that are observed after adsorption. Indeed, these are initiated well after that the protein monomers have diffused to the interface. As previously stated, protein monomers present a dynamically inhomogeneous chemistry (i.e., conformational activity) and this might, further, evolve during adsorption. As a result of these conformational changes, which occur before (or during) adsorption, the chemistry of the adsorbing ensemble evolves with respect to time. Very probably, a wide range of surface aggregation mechanisms occur simultaneously and a statistically probabilistic scenario of different local areas forms within the adsorbed layer. That is, the local conformational energy minima that coexist and slowly evolve within the adsorbing layer might also determine local decays in surface tension.

In this work a number of different methods have been investigated to approximately characterize the adsorption (and nucleation) of lysozyme onto surfaces with different chemistries. The introductory trials were performed with a conventional lysozyme formulation (i.e., 50 % of a 0.1 M acetate buffer, at pH 4.7, and 50 % of a 6.5 % w/v sodium chloride solution). This formulation has been tested on plain silicon surfaces (for 4 hrs) and its adsorption has been observed with a Veeco Wyko optical profilometer (with resolution of about 160 nm). Similarly, the adsorption of lysozyme on the methyl, trifluoro-propyl, aminopropyl and mercaptopropyl substituted surfaces, has been observed be means of infrared-reflection-absorption spectroscopy (IRRAS). That is, a grazing angle IR analysis was performed by means of a Bruker Tensor-27 with a 75° angle of incidence set. IR spectroscopy is a well-established technique, which is used to detect molecular vibrations. Each molecule has an IR vibrational spectrum, that is, molecular vibrations that are associated with any changes in the molecule electric dipole moment. Homonuclear diatomic molecules do not exhibit IR vibrational spectra. Conversely, the IR spectrum, of all other molecules, contains information about the different types of bonds within a molecule, that is, it gives their structural analysis. The vibrational modes are usually categorised as arising from either stretching or deformation vibrations. Stretching modes tend to display bands between 4000 – 1500 cm^{-1}, while the deforming vibrations tend to be in the range 1500 – 500 cm^{-1}. Although, during these experiments this technique has been used as a guideline only, (Guyt et al., 2002), the results relating to the above-mentioned experiments have demonstrated, on all the surfaces, that the surface-adsorbed layer may well present some salt in it. The salt excess was observed also in UV microscopy trials. These were performed with a Leica TCS-SP (at the UCL Wolfson institute of biomedical research). As shown in Fig. 5.1, the fluorescence of the lysozyme tryptophan residues was hard to observe, after adsorption from the conventional formulation.

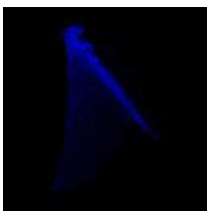


Fig. 5.1 *The picture shows some of the UV microscopy exploratory observations. That is, it shows a lysozyme solution after a few hours crystallization on a silicon slide. The fluorescence signal is much weaker than predicted and the technique was non utilizable as a result of this.*

As a result of the aforementioned trials, a set of new experiments was planned to lower the concentration of the precipitating agent at the interface. That is, a screening to formulate a new precipitant solution was finally accomplished. Notwithstanding that an ideal precipitant formulation was successfully formulated, it was noticed that also air intrusions (in the solution or by the solution-solid interface) might well alter the adsorption, and clustering or nucleation, of lysozyme molecules. Following additional crystallization experiments, and the understanding of the literature on the structuring of lysozyme at the air-water interface, it has been concluded that, despite its extremely hydrophobic nature, the air-water interface would enhance the ordered structuring of lysozyme rather than its adsorption (or amorphous clustering).

It can be, certainly, asserted that the presence of unwanted air droplets in a crystallising protein solution is a non-controllable and physically-chemically active factor for nucleation. This has been well recognised for globular proteins such as lysozyme. Indeed, in some neutron reflectivity experiments from the literature the distribution of HWEL (i.e., hen white egg lysozyme) monomers at the air-water interface has been characterized and a bilayer structure has been detailed. This bilayer structure would present an ordered layer closer to the air (i.e., closely packed monomers) and a second layer with features that are intimately related to the protein bulk concentration. Differently from serum albumin (which unfolds despite its globular structure), the structure of lysozyme monomers at the air-water interface remains unmodified. In fact, in the literature, adsorption tests with HWEL variants presenting monomers with destabilized structures (that is, with greater hydrodynamic radius and lower diffusivity) show enhanced adsorption kinetics at the air-water interface (Lu et al., 1999; Podhipleux et al., 1999). In the specific case of non-destabilized lysozyme the presence of air droplets may facilitate the formation of ordered structures and, therefore, heterogeneous nucleation at the solution-solid (or gas) interfaces. As a result of this, the presence of air droplets entangled by the solution-solid interface may well blur the repeatability, and interpretability, of lysozyme heterogeneous nucleation data.

5.2 Optimization of the HEWL Crystallising Formulation

Lysozyme may crystallize in different forms: cubic, hexagonal, tetragonal, orthorhombic, monoclinic and triclinic, and these have been, also, listed in Fig 5.2.

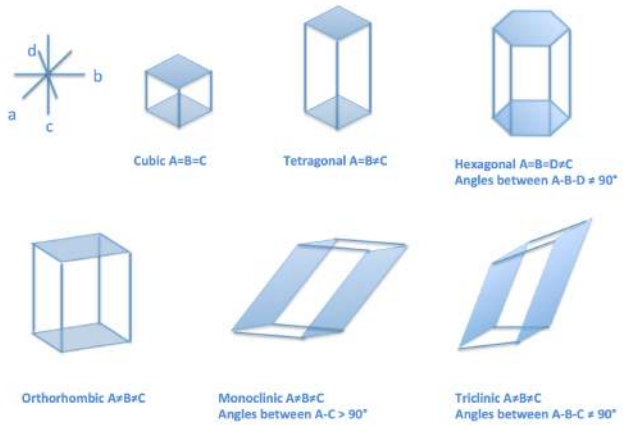


Fig. 5.2 *The representation of the crystal forms from the seven crystal systems.*

Each lysozyme monomer is a single chain polypeptide of 129 amino acids that are cross-linked with four disulfide bridges (and its molecular mass is 14.3 kDa). Lysozyme is an enzyme and it hydrolyzes the β-linkages of peptidoglycan and chitodextrin structures of bacteria (Gram-positive bacteria are, indeed, affected by this enzyme). Lysozyme is active over the 6 – 9 pH range (and it has maximal activity at pH 6.2). More specifically, it is active over the 0.02 – 0.1 M ionic strength range at pH 6.2 and over the 0.01 – 0.06 M ionic strength range when higher pH values are set. Lysozyme has been conventionally crystallized at pH 4.8 from a 0.1 M sodium acetate (NaAc) buffer by adding a 10 % – 7.5 % w/v sodium chloride (NaCl) solution. Indeed, it has been described in section 5.1, already, that the solution dynamics of protein monomers are, primarily, governed by the electrokinetic potentials of the protein solute and other co-solutes. In the literature, the electrokinetic potential values of acidic sodium chloride solutions have been observed to decrease on increase of the electrolyte concentration. In fact, it has been mentioned above, that, conventionally, the salting-out of lysozyme and other proteins (that is, their amorphous aggregation or nucleation) has been, induced from highly

concentrated and acidic sodium chloride solutions. Nevertheless, lysozyme has, also, been crystallised from other electrolyte solutions such as magnesium sulfate ($MgSO_4$) solutions at pH 7.8, calcium chloride ($CaCl_2$) solutions at pH 7.8 and magnesium chloride ($MgCl_2$) solutions at pH 7.8, (Broide et al., 1996; Forsythe et al., 1999; Fritz et al., 2002).

It has been, in fact, demonstrated in the previous sections that protein monomers may adsorb, or structure, on hydrophobic surfaces such as the air-water interface. As the latter, according to section 4.1.2, is of a hydrophobic nature, air droplets (or air-filled cavities) do generate hydrophobic surfaces. Also, it has been mentioned that the more a solid surface is hydrophobic the higher is the percentage of air that may become trapped by its solution-solid interface (Shang et al., 2005). That is, the presence of air droplets at the solution-solid interface is a blatant phenomenon (Martines et al., 2006) and this may become an unwanted interference factor, especially, when protein dynamics at interfaces were regarded. Also, this interference may become a real problem, especially, when the nucleation patterns of lysozyme at interfaces were researched on. Moreover, unwanted contaminants (such as air droplets) may aggravate the already well-known repeatability issues. Indeed, as a result of this, protein crystallizing solutions are, usually, handled with extreme care (that is, for example, a degassing procedure may be too aggressive or it may trigger unwanted phenomena). Furthermore, out-layers may well be observed in the experimental results, even when the crystallization experiments had been performed after filtering with cut-offs well below the μm threshold.

This work aimed to prove, and investigate, the effect of surfaces bearing different nano-patterns or chemistries on the nucleation rate of lysozyme. Also, these experiments have been, especially, planned to prompt reveal the effect of the surface chemical, or topographical, features on the protein nucleation pattern. That is, finally, the factors (such as the salt excess, air content or pre-nucleated protein material) that may interfere with the protein dynamics at the solid-liquid interface have been detailed and, to a certain extent, controlled. Lysozyme from chicken egg white crystalline powder (70000 U/mg by Sigma Aldrich) was used during the first trials of this work, however, this has been, thereafter, replaced with lysozyme from chicken

egg white lyophilised powder (by Sigma Aldrich, cat. number 62970). The latter type of lysozyme preparation (which is extracted from chicken egg white by, first, crystallizing it three times, then, dialyzing it, and, finally, lyophilizing it) was used as received. Additional (lower cut-off) filtration trials were, necessarily, performed, as most of the commercially available lyophilized hen-egg white lysozyme preparations may contain significant populations of pre-nucleated protein particles. These particles, indeed, may have size well below the filter cut-off (i.e., 0.22 μm) that is, generally, used to filter protein solutions before crystallization, (Parmar et al., 2007). The above filtration trials are thoroughly described in chapter 6.

Also, in this work, the crystallizing lysozyme solutions were formulated to minimize the concentration of all the solutes and, especially, to minimize the interference due to air droplets. That is, the classical drop vapour-diffusion crystallization method has been replaced with an air-depleted micro-batch method, in order to minimize the structuring effects of unwanted air intrusions on the heterogeneous nucleation of lysozyme. This method, indeed, involves the use of a crystallization device. A design of this device is introduced at the end of this section, and a full description is given in chapter 6. It has been previously mentioned that, several trials were performed to obtain a suitable crystallizing solution. Indeed, originally, the screening procedure was performed on two different proteins. Nevertheless, only the preparation work relating to lysozyme has been concisely reported in the following paragraphs. Indeed, lysozyme was, first, crystallized from its conventional formulation and, finally, it was crystallized from a newly formulated low-salt solution. Specifically, after screening, a 50 mM borate buffer and a solution of 0.6 % w/v sodium nitrate ($NaNO_3$) were used to prepare the new low-salt crystallizing solution. The 50 mM borate buffer had been prepared from a 50 mM solution of disodium-tetra-borate-deca-hydrate ($Na_2B_4O_7 \cdot 10H_2O$) by adding a boric acid (H_3BO_3) 0.04 % w/v solution up to pH 7.8. Two different sets of precipitant concentrations have been defined, those that gave lysozyme crystallization in two days at room temperature and those that did not give any evident crystallization of this protein within the above time range (all these concentrations fall in the range 4.58 – 7.44 % v/v of the precipitant solution).

Also, 4 different lysozyme concentrations have been tested (5, 10,15 and 20 mg/ml).

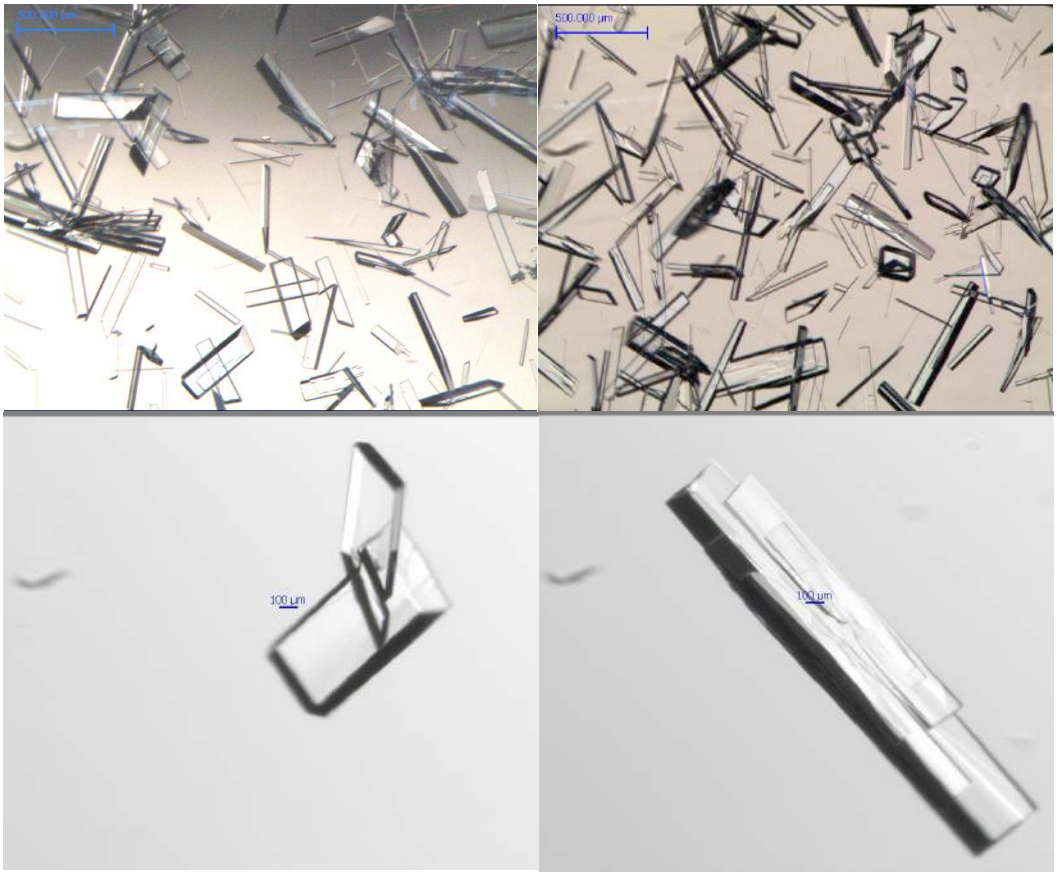


Fig. 5.3 *The crystallization of lysozyme after 24 hrs is shown in these pictures (top pictures), and the details relating to the crystal forms are shown below these (bottom pictures). The pictures have been taken with a Leica Microscope M165C, (Agnese Zicari ©, 2009).*

The initial bulk crystallization trials produced crystals with a broad range of specifications. Monoclinic and triclinic crystals may be observed in the pictures of Fig. 5.3. A crystal from the newly formulated lysozyme solutions, which is shown in the picture of Fig. 5.4 (a), was tested under x-rays and this is shown in Fig. 5.4 (b). A Rigaku Micromax 007HF-M high flux generator in a "double headed" configuration (i.e., featuring a left hand port with high flux optics and a ≈ 100 µm spot size, a right hand port with high flux optics and an MAR345 image plate detector with a ≈ 200 µm sample spot size, and a beam divergence of 4.8 – 0.1 mR) was used to generate the data that are shown in Fig. 5.4 (b). Also a gel electrophoresis test, which is shown in Fig 5.4 (c), has confirmed the absence of contaminating proteins. The x-ray analysis diffraction patterns shows that there is some other crystal lattice content within that of the lysozyme crystal. As, on average, 40 % of each protein crystal is made of water & co-solutes, the above content might be due to the precipitant. Nevertheless, the above x-ray results

might only confirm the very poor symmetry of that lysozyme crystal.

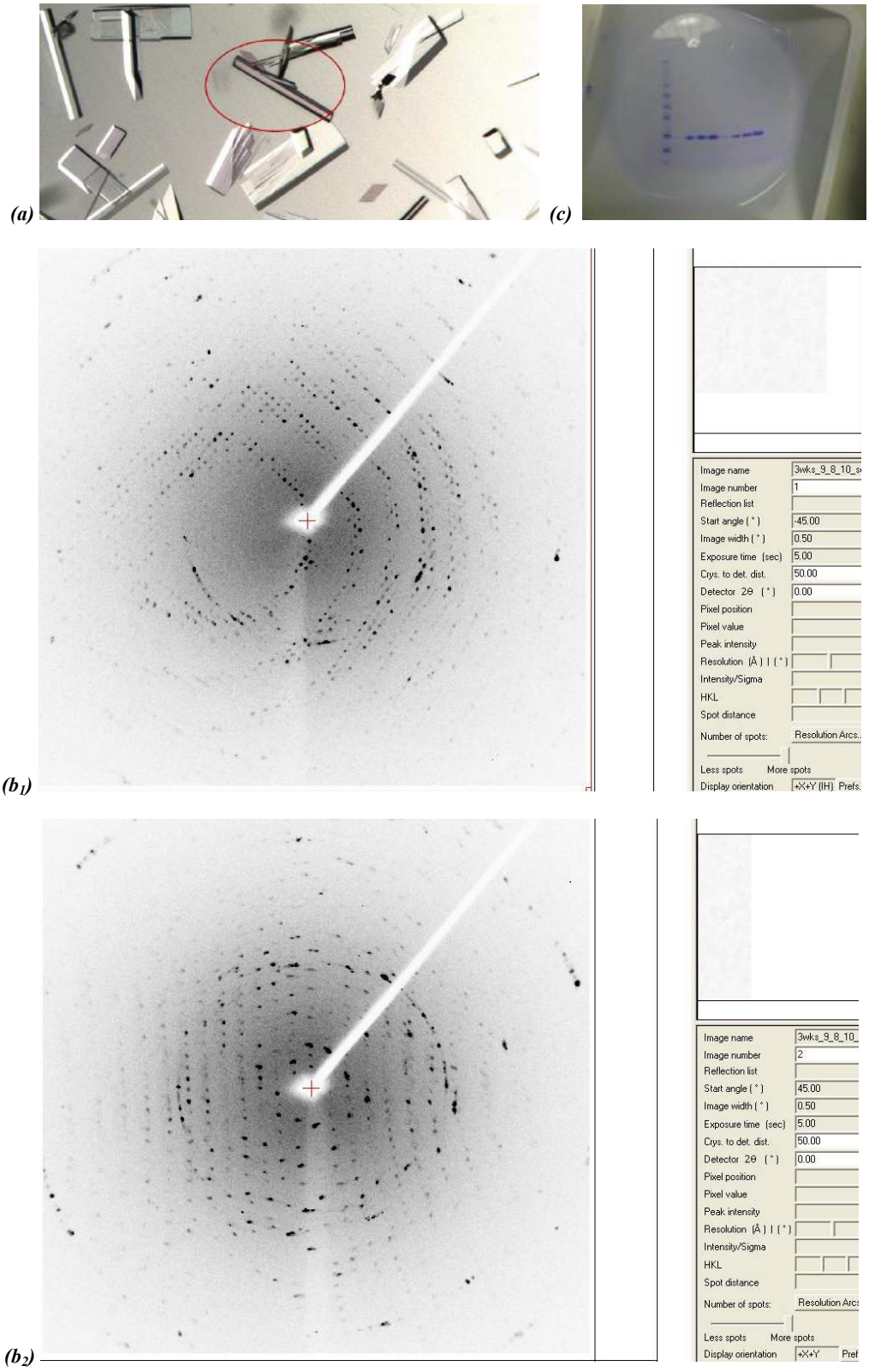


Fig. 5.4 (a) *A chosen lysozyme crystal has been tested under x-rays.* ***(b_1 & b_2)*** *The diffraction patterns of the crystal from picture (a) are shown.* ***(c)*** *This picture shows the gel electrophoresis of the crystallizing solution, where the crystal in (a) formed.*

The crystallizing formulation was further ameliorated. Indeed, hanging-drop-type screening trials were performed in order to better define the precipitant and protein concentrations. These trials were performed on a PTFE porous membrane. Following the above tests, the concentration of the precipitating salt has been reduced down to values in the range of 6 % v/v of the whole solution. Moreover, other analytical techniques, such as UV spectroscopy and PCS, have been used, contemporarily, to further characterize the new formulation. PCS, especially, was also used to evaluate the benefit of using different cut-off filters.

PCS (photo-correlation spectroscopy), which is also known as DLS (dynamic light scattering), is commonly used to size small particles including proteins. Simplistically, this measures the fluctuations of the scattered light intensity that are determined by the Brownian motion of all the particles with size below an entering beam wavelength. With respect to proteins, very probably, the recorded intensity values strongly depend on, not only, their cluster size (or geometry), but also, on locally induced maculae of density and polarizability. As a result of this, different co-solute types (kosmotrope or chaotrope) at different concentrations may differently enhance the formation of solvent-mediated polarizablity (and viscosity) maculae, which might also locally decrement the diffusion coefficients of the primary solute particles. Conventionally, when an irradiating beam hits particles with size below its wavelength, the Rayleigh scattering theory applies. That is, the scattered frequency is polarizability-related and it is originated when the electric field of the entering beam irradiates the electrons of the differently assembled solution chemical entities. Indeed, the beam that has been scattered by each entity (i.e., a particle or structured macula) maybe subjected to constructive or destructive interferences by other surrounding polarizability maculae. The above scatterings would reinforce, or compete, with each other and appear as polarizability fluctuations that might be regarded as representative of the primary particles only. That is, the solution chemical entities differently contribute to originating infinitesimal volumes of polarizability that are registered as time-dependent spatial fluctuations of the system dielectric constant. This phenomenon has been conventionally described with the equations 5.1 and 5.2:

$$\boldsymbol{\varepsilon}(\boldsymbol{r},t) = \varepsilon_0 \boldsymbol{I} + \delta\boldsymbol{\varepsilon}(\boldsymbol{q},t) \qquad (5.1)$$

$$I_{if}(\boldsymbol{q},\omega_f,R) = \left[\frac{I_0 k_f^4}{16\pi^2 R^2 \varepsilon_0^2}\right] \frac{1}{2\pi} \int_{-\infty}^{+\infty} dt < \delta\varepsilon_{if}(\boldsymbol{q},0)\delta\varepsilon_{if}(\boldsymbol{q},t) > \exp i(\omega_f - \omega_i)t \qquad (5.2)$$

where the local dielectric constant, $\boldsymbol{\varepsilon}$ ($\boldsymbol{r}$, t), is a function of the dielectric constant fluctuation tensor, $\delta\boldsymbol{\varepsilon}$ ($\boldsymbol{q}$,t). In the latter the scattering geometry vector (q) derives from an irradiating infinitesimal volume (d^3r) at a specific position (r) (from the centre of the illuminated volume) and time (t). While I is the second rank unit tensor. That is, any frequency change of the entering beam (I_o) depends only on how $\delta\boldsymbol{\varepsilon}$ ($\boldsymbol{q}$,t) varies with time. The recorded intensity I_{if} ($\boldsymbol{q}$, ω_f, R) is, therefore generated by an infinitesimal geometry $\boldsymbol{q}=\boldsymbol{k}_i - \boldsymbol{k}_f$; where $\boldsymbol{k}_i$ (which points in the direction of propagation of the incident beam) and $\boldsymbol{k}_f$ (which points in the direction of the beam that reaches the detector at a distance R), form a scattering angle and generate an associated frequency change $\omega_i - \omega_f$ (Berne & Pecora, 1975/2000). In this work, a Malvern Zeta-Sizer-Zen 3600 (λ = 532) was, used to define the most suitable lysozyme concentration and filter cut-off. The Zetasizer calculates the particle size (in the range 0.6 nm − 8.9 μm), zeta potential and molecular weight of molecules (or particles) in solution. The particle scattering intensity decay times for the different concentrations that have been tested in this work are shown in Fig. 5.5. While the results from the experiments with lower cut-off filters are shown in Fig. 5.6.

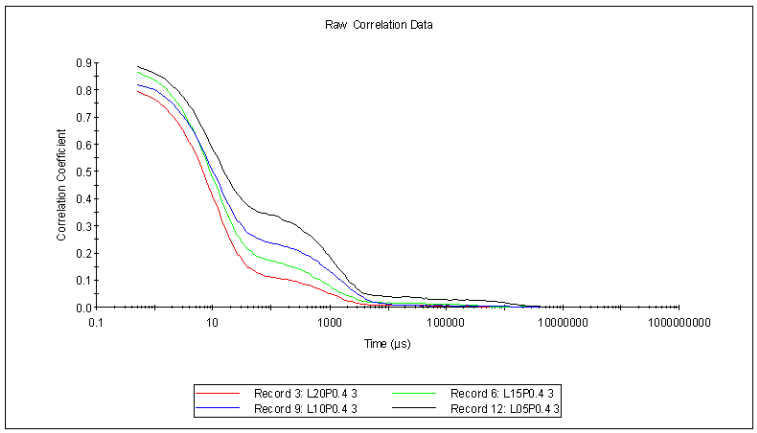
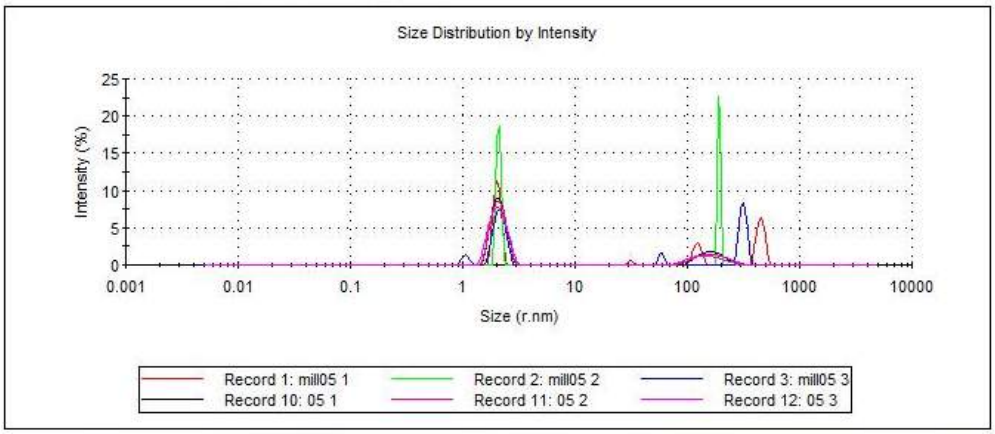
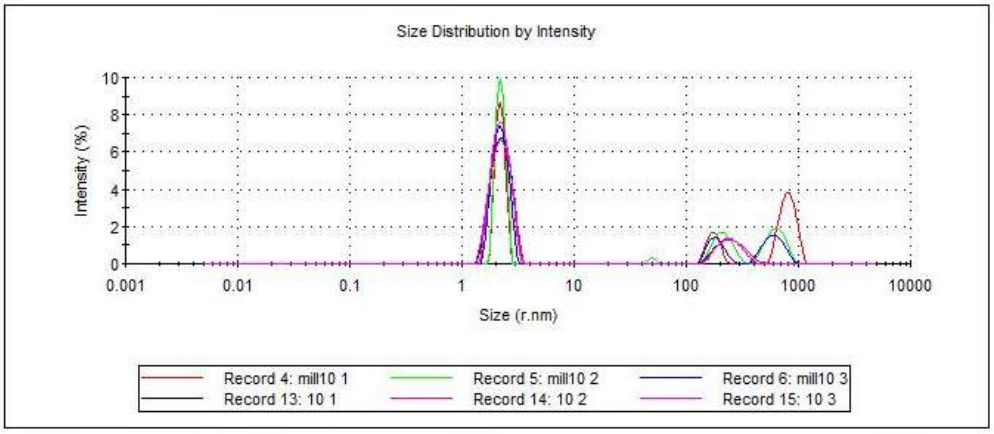


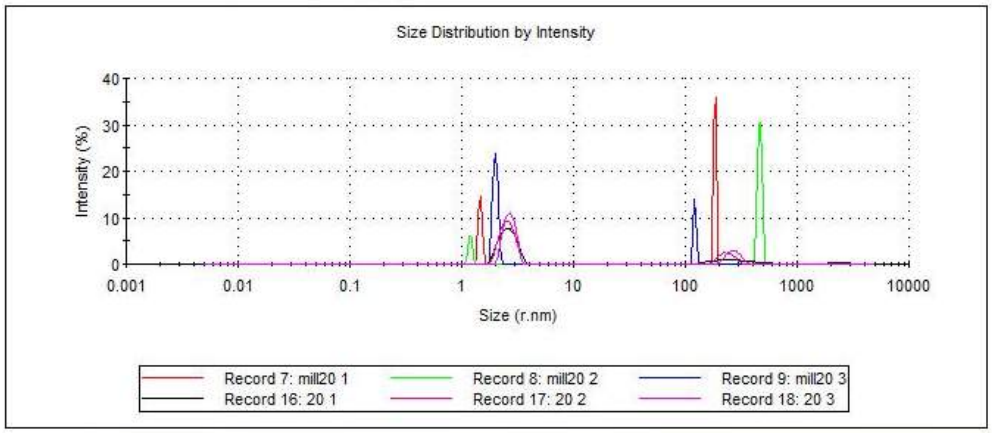
Fig. 5.5 *The correlation coefficients of the lysozyme crystallizing solutions with decreasing concentration (20 mg/ml, 15 mg/ml, 10 mg/ml and 5 mg/ml) have been compared, after 220 nm filtration, (Agnese Zicari ©, 2012).*



(a)



(b)



(c)

Fig. 5.6 *The lower concentration lysozyme solution has been filtered with 5 nm, 10 nm, 20 nm cut-off Millipore syringe filters: from the top: (a) "5 nm", (b) 10 nm and (c) 20 nm; (these data have not been averaged intentionally), (Agnese Zicari ©, 2010).*

The intensity data in Fig. 5.6 might suggest that the multimodal distribution of the different lysozyme solutions is unstable, which seems to be more obvious at lower lysozyme concentrations (Fig. 5.5). Indeed, according to the data in Fig. 5.7 (which refers to a 5 mg/ml lysozyme solution after 220 nm cut-off filtration) the above instability seems to

endure until right before reaching a critical equilibrium. Also, according to the correlation data in Fig. 5.5, within so a dynamically unstable scenario, the contribution from the larger aggregates appears to be statistically more significant as the nominal concentration drops. This is also reflected in an increase of the reported % PD (i.e., % polydispersity) values. That is, the % PD value rises from 64 % to 89 %, while decreasing the concentration from 20 to 5 mg/ml. Moreover, the intensity scattering of the 5 mg/ml lysozyme crystallizing solution has been monitored for 24 hrs. The mean hydrodynamic diameters that have been recorded during the first 4 hrs are summarised in Tab. 5.1. An initial increasing trend, while a slightly decreasing trend afterwards, might be inferred.

hr	**peak 1 mean hydrodynamic diameter**	**peak 2 mean hydrodynamic diameter**
1	4.86 nm	241.02 nm
2	6.43 nm	969.32 nm
3	6.04 nm	604.7 nm
4	5.04 nm	351.6 nm

Tab. 5.1 *This table summarizes the 1st & 2nd peak mean hydrodynamic diameter for the 5 mg/ml solution, in the first 4 hrs, (Agnese Zicari ©, 2015).*

Supposedly, peak1 represents the scattering of lysozyme monomers/oligomers (the monomer diameter is 3.8 nm by the literature) while peak 2 represents the protein clusters'. That is, given the time-dependency of the scattering by peak 2, a broad range of kinetically unstable aggregates must occur.

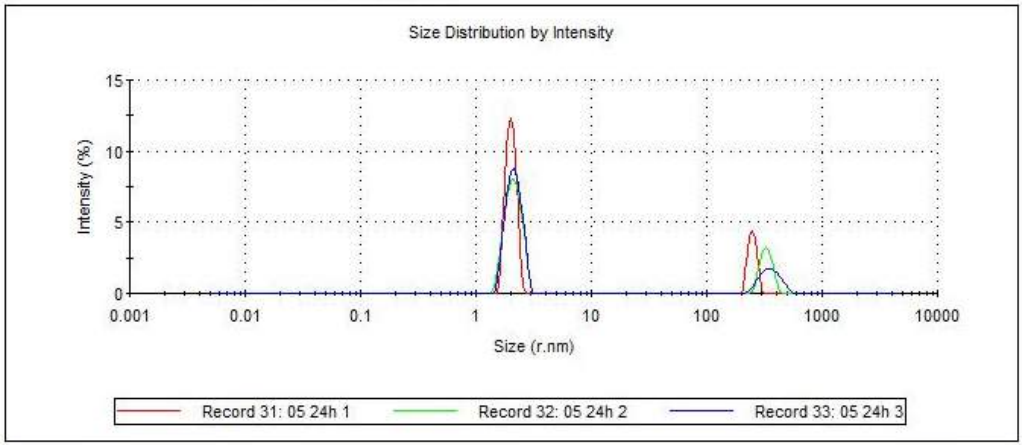


Fig. 5.7 *The 5 mg/ml lysozyme solution has been filtered after 24 hrs with 220 nm cut-off syringe filters (these data have not been averaged intentionally), (Agnese Zicari ©, 2010).*

As stated in chapter 2, the energy minimum within all the different conformational minima along the main axis of the aggregate can generate protein clusters of different morphologies. That is, the local cluster configuration reaches its energy minimum when one of the multiple statistically determined aggregation pathways results in the right combination of different conformational energy values. Hence, the above-mentioned experiments confirm that, probably, there is a kinetically diverse landscape of configurational changes and that, at a certain point, this may generate a thermo-dynamically favoured 3D-pattern. That is, a uniformly layered landscape of energy levels may, probably, arise once certain solution factors and parameters have been nominally imposed.

Following the above-mentioned experiments, the lysozyme solution of lower concentration has been chosen to further characterize it with UV spectroscopy. The Lambert-Beer theory states that the absorbance of a solution is directly proportional to the concentration of the absorbing species in the solution as well as to the solution path length. Usually, the use of UV spectroscopy involves the measurement of the solution absorbance to detect the solute concentration and a calibration curve (i.e., plot) is first generated, if very accurate concentration measurements are necessary. The absorption graph, usually, presents wavelengths of absorption that stem from the different types of bonds, and, therefore, functional groups, within the solute molecules. However, a number of factors, such as the type of solvent, temperature, pH and electrolyte concentration or interferences, may shift the peaks of absorption. Specifically, when the lysozyme molecules are suspended in a solution with pH values in the 7 – 9 range, the absorption values are in the region of 250 – 300 nm. Also, according to the literature, the initial absorption peaks of a lysozyme solution are proportional only to its concentration. However, when the lysozyme in solution starts to crystallize, an absorption peak at 350 nm may be, instead, detected to monitor nucleation (Hua et al., 2001). A single beam Perkin Elmer UV/Vis spectrophotometer (with 190 – 750 nm light source range) was used to perform a number of measurements on different crystallizing lysozyme solutions. Also, quartz cuvettes with 10 mm and 40 mm path lengths were used to run these tests. Some data were, also plotted after

calculating the turbidity values with the following equation.

$$t = \frac{2.303\ A}{d} \qquad (5.3)$$

where t is the turbidity, A is the measured absorbance and d is the path length. The (350 nm) turbidity values of the protein solution with ≈ 3 % v/v precipitant concentration and 5 mg/ml lysozyme concentration are plotted for both the 10 mm (a) and 40 mm (b) path lengths in Fig. 5.8

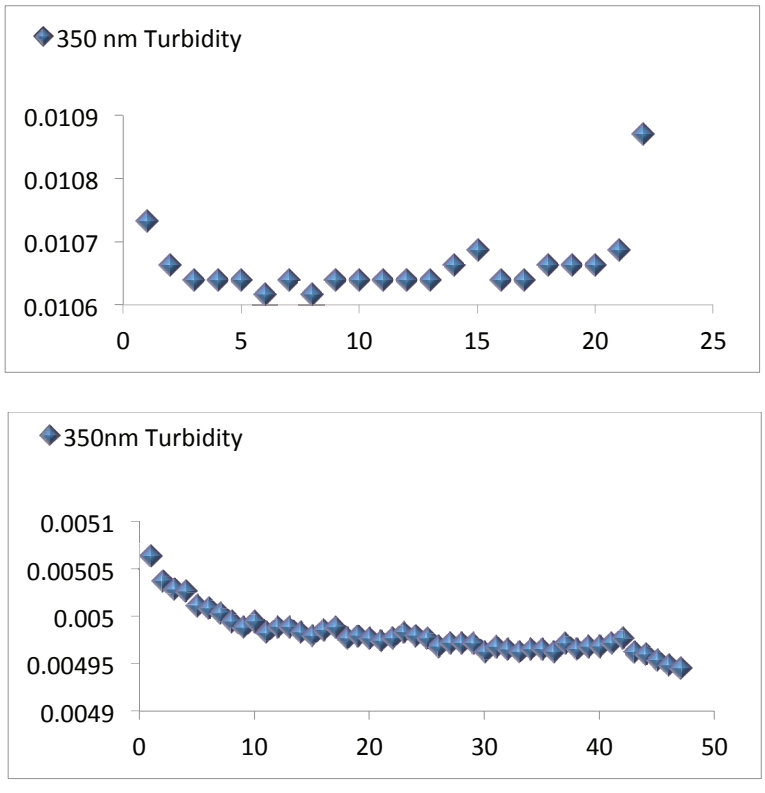


Fig. 5.8 *The (350 nm) turbidity values of the 5 mg/ml lysozyme solution at low precipitant concentration ≈ 3 % v/v:* ***(a)*** *The plot over 24 hrs shows that the nucleation process may start between 20 and 24 hrs (a 10 mm path length was used on this occasion).* ***(b)*** *The plot over 48 hrs reveals that a sedimentation process may blur the nucleation process since time 1 hr (40 mm path length was used on this occasion), (Agnese Zicari ©, 2010).*

Nevertheless, the data reported in Fig. 5.8 do not allow a clear visibility of the nucleation process and this may be due to the overlapping of two contemporary on-going local metaphase equilibria: the nucleation (or "demixing") of the lysozyme in solution and a pseudo-sedimentation phenomenon. These may occur contemporarily or at different times and locations. Possibly, the use of a cuvette with a shorter path length (such as 0.5 mm) might reduce the overlapping of bulk phenomena and ameliorate the understanding of the above data.

5.2.1 Crystallization via an air-depleted micro-batch method

The heterogeneous crystallization trials were performed with an air-depleted micro-batch method. A device was appositely designed to hold the substrate in contact with few hundred micro-litres of the protein solution and to minimize the content of air droplets. The device has an airtight quartz window (which is inserted in the top lid) and an airtight bottom slide holder that is used to place a 25 × 25 mm square slide and hold the substrate. The approximate external and internal cell dimensions are: 20 mm height, 60 mm side, and a 5 mm high × 14 mm wide cylindrical internal "tank". Also the device has a couple of airtight holes that were strategically designed and positioned to allow the transfer of fluid through the inlet and gas through the outlet. A number of devices were designed and tested, and the designs relating to the first and the final device design are illustrated in Fig. 5.9.

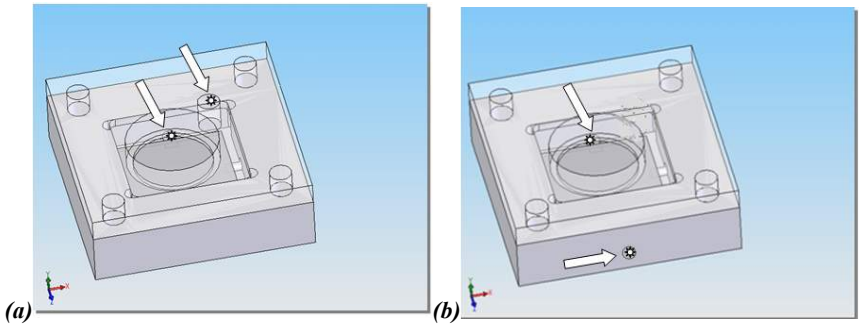


Fig. 5.9 *The crystallization devices with the inlet and outlet (✲): **(a)** The initial design **(b)** The most recent design with internal and external cell dimensions of ≈ 20 mm (height), 60 mm (side), and a cylindrical internal "tank" of 5 × 14 mm, (Agnese Zicari ©, 2009).*

As previously explained, globular proteins such as albumin and lysozyme may adsorb, on its own (or in binary mixtures), on different substrates and this has been characterized in different research studies. Also the adsorption of albumin (which, similarly to human growth hormone, unfolds at the air-water interface) is inversely proportional to its bulk concentration. This would suggest that (depending on the protein type, the type of solid-liquid interface and the solution nominal concentration) the intrinsic nature of the protein monomers may become the primary factor to define the adsorption dynamics at interfaces (Baszkin et al., 1993; Buijs et al., 1998). It may be, therefore, concluded that, although by the literature lysozyme has its own pattern of adsorption, a behaviour similar to that of the above-mentioned

globular proteins may be induced as a result of combining factors. That is, the hydrophobicity of a solid surface (which may be, also, altered by the entrainment of air droplets) together with the aforementioned protein solution factors, may well influence the lysozyme response to (and its structuring at) solid-liquid interfaces.

In the light of this, the experiments were performed while ameliorating the design of the devices to perform air-depleted injection and nucleation. Initially, the protein solution was stored in a beaker and a tubing system (which was made of a protein compatible plastic and equipped with a clip to create vacuum) was used to inject the solution into the device. Although in the above-mentioned experiments the visible air droplets appeared well distant from the tested surface, the air droplets formed easily and poor repeatability was observed. Therefore, a new device (which features a controllable injection system) was designed to minimize the entrainment of air nano-droplets by the interface of interest. The new device has a better designed inlet, and outlet, so that vacuum may be applied while the protein solution is poured in the internal device compartment. During the initial trials with the above device, the solution was injected with an airtight syringe by piercing a rubber sealing cup that covered the cell inlet. However, in the following trials a proper arrangement was, finally, selected. That is, 220 nm cut-off filters were screwed to an airtight syringe on one side and to the device on the other, a full description of this method is given in chapter 6.

The initial crystallization trials, where the interference due to air droplets was first observed, were performed before defining the optimal formulation or cell design (that is, the protein in acetate buffer at pH 4.7 was mixed with an equivalent volume of sodium chloride 6.5 % w/v). In these trials, such as the trial that is described in Fig. 5.10, the presence of abundant air inclusions and catalysis of the crystallization process were observed. Indeed, the trials that are shown in Fig. 5.10 demonstrated that visible lysozyme crystals form after one day only. Though, in other trials with the same crystallization formulation, and where no air droplets had been observed, a crystallization time of about 4 days was, instead, recorded.

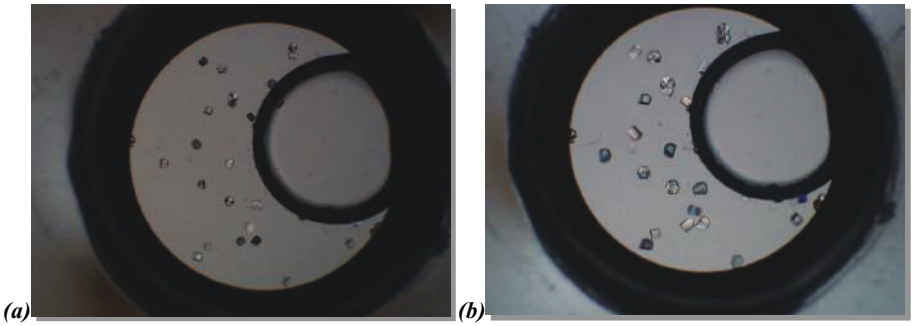


Fig. 5.10 *The crystallization of lysozyme from the original formulation on bare silica in the presence of visible air droplets after: 24 hrs* ***(a)*** *and 48 hrs* ***(b)****. A Wild/Leica M420 photomicroscope provided with an Olympus DP70 camera was used in this instance, (Agnese Zicari ©, 2009).*

It is believed that, the use of the above-mentioned air-depleted method, has reduced the air droplet content and the relating effect on the heterogeneous crystallization of lysozyme. It is also believed that the use of the new precipitant formulation has minimized the effect of the precipitant salt on the adsorption and nucleation of lysozyme. Indeed, further to these tests, additional experiments that involved the use of patterned substrates were, eventually, performed. Specifically, some of the 5 × 5 mm substrates, which had been fabricated according to the procedures in chapter 4, were used to test the heterogeneous crystallization of lysozyme on flat, or patterned, epoxy-surfaces before and after oxygen plasma activation. The substrates were immobilised on 25 × 25 mm glass slides using natural wax and then the slide was sealed into the crystallization device. The newly formulated lysozyme crystallizing solution was prepared according to the procedure δ from chapter 6 and with a final sodium nitrate concentration of 4.58 – 7.44 % v/v of its 0.6 % w/v solution in a 50 mM borate buffer (i.e., at 7.8 pH). The filtered solution was then poured into the crystallization device while applying vacuum by means of an airtight syringe and the device was turned upside down before crystallization. That is, the substrate slide was situated uppermost to minimize the side effects of any sedimentation. The results relating to some of the above experiments are shown in Fig. 5.11 and 5.12. The crystallization process was monitored at Time 1 and Time 2 with a Leica Microscope M165C. The picture showing the crystallization on the patterned epoxy-surface before plasma treatment may reveal a catalytic effect of the surface on the crystallization of lysozyme, that is, after 6 hrs, crystals look bigger on the more hydrophobic surface.



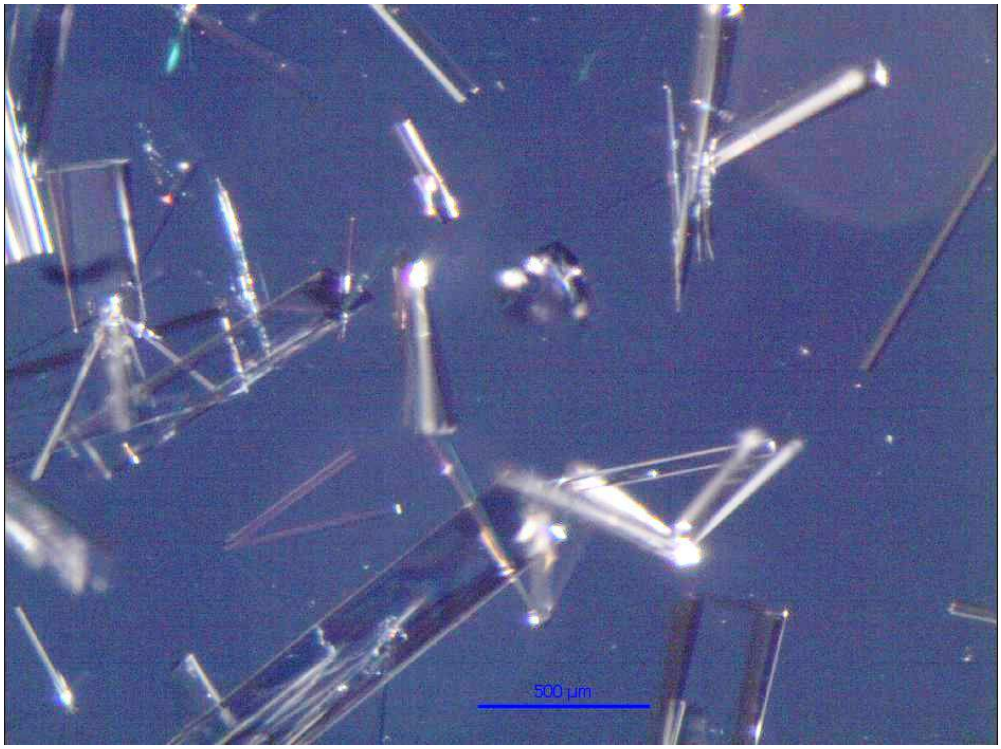
(a)



(b)

Fig. 5.11 *The air-depleted crystallization of the 5 mg/ml lysozyme solution (new formulation) after 6 hrs only:* ***(a)*** *top - the details of the crystal formed on the epoxy substrate;* ***(b)*** *bottom - the details of the crystal formed on the epoxy substrate after exposure to the oxygen plasma. The pictures have been taken with a Leica Microscope M165C under UV light, (a 500 μm scale-bar was set), (Agnese Zicari ©, 2010).*

(a)



(b)

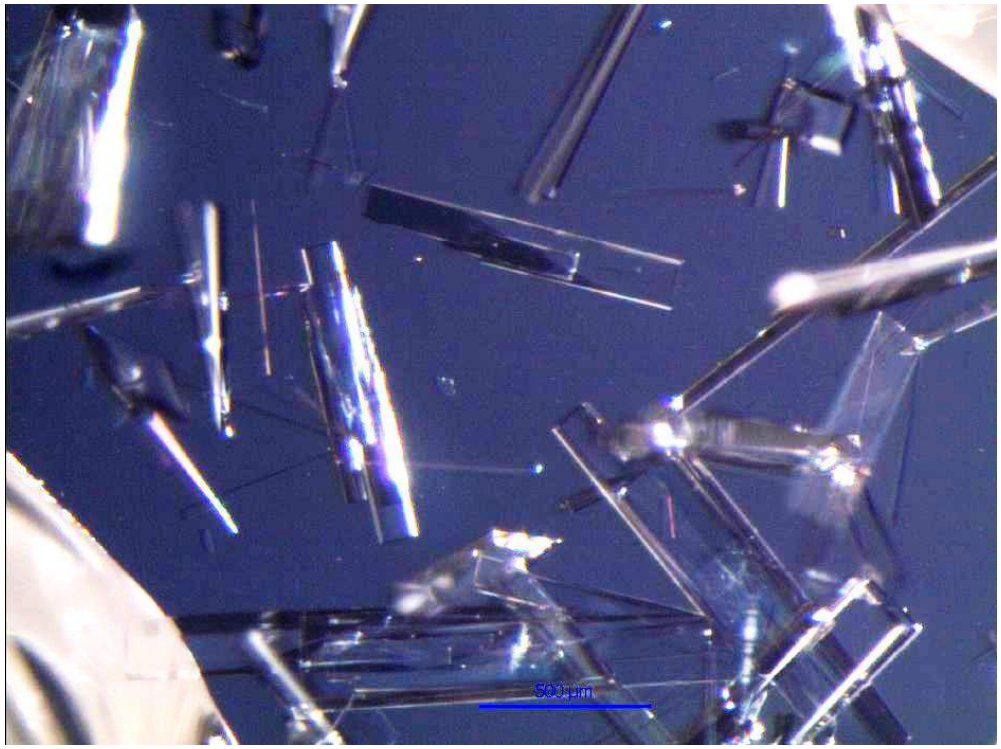


Fig. 5.12 *The air-depleted crystallization of the 5 mg/ml lysozyme solution (new formulation) after 24 hrs:* ***(a)*** *top - the details of the crystal formed on the epoxy substrate;* ***(b)*** *bottom - the details of the crystal formed on the epoxy substrate after exposure to the oxygen plasma. The pictures have been taken with a Leica Microscope M165C under UV light, (a 500 µm scale-bar was set), (Agnese Zicari ©, 2010).*

Chapter 6

Experimental Design & Methodology

6.1 Introduction to the Experiments' Design

6.1.1 Introduction the heterogeneous nucleation of lysozyme

In this work both the protein homogeneous and heterogeneous nucleation dynamics have been parameterised according to the chart in Fig. 6.1. Also, various methods have been used to better discern and control the processes that evolve from the above dynamics.

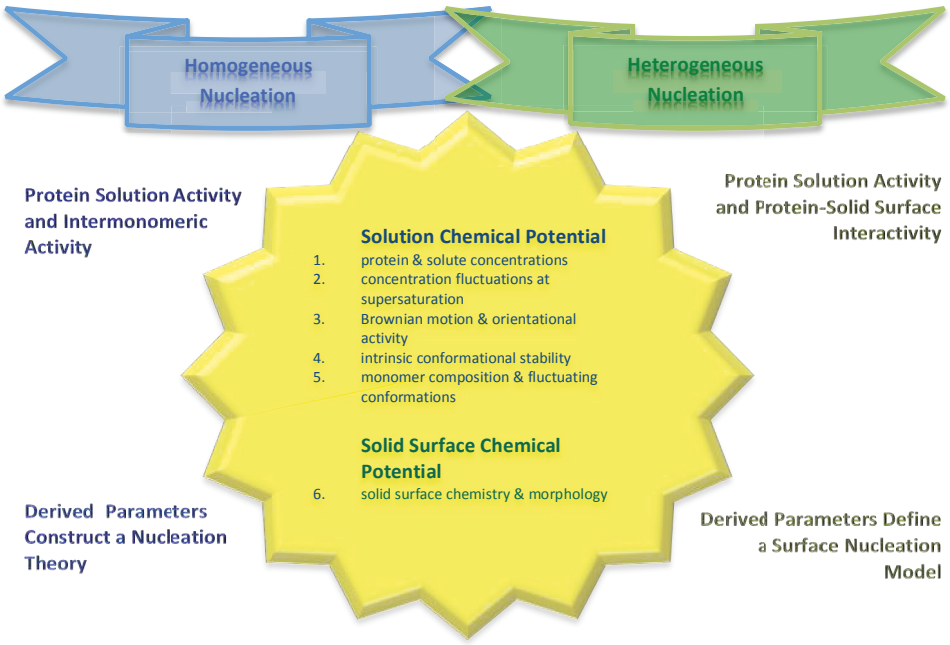


Fig. 6.1 *The protein homogeneous & heterogeneous nucleation dynamics differ in that the latter is affected, also, by the surface chemical potentials.*

Here, 2 main sets of governing factors have been listed in this regard (i.e., solution, and surface, related factors). Also, these have been sorted out according to their degree of controllability.

Protein solution factors:

➔ controllable factors: temperature, nominal protein and co-solute concentration(s), solution preparation procedure.

***

➔ non-controllable factors: chemical anisotropy, conformational activity, Brownian motion (i.e., translational & orientational motion), permittivity, local concentration fluctuations, local protein & co-solute adsorption.

***

Surface factors:

➔ controllable factors: surface chemistry type, surface nominal average roughness, surface nominal degree of substitution.

***

➔ non-controllable factors: local morphology/roughness, local degree of substitution and air droplet surface entrainment.

***

As a result of their interdependency, the above factors do generate an additional set of non-controllable factors at the solid-liquid interface. The latter set has been noted down in Fig. 6.2.

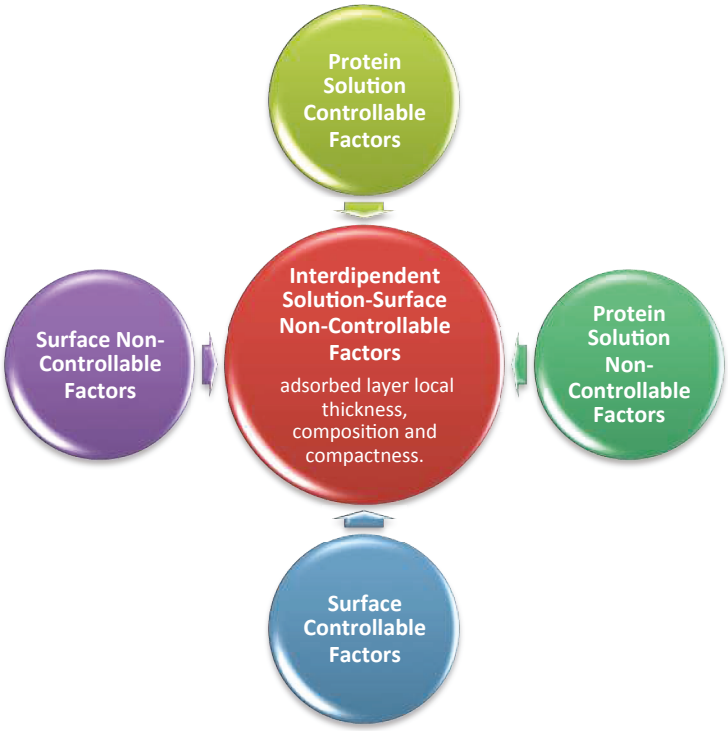


Fig. 6.2 *A flow-chart of the solution & surface controllable & non-controllable factors, (Agnese Zicari ©, 2015).*

6.1.2 Planning experiments with protein solutions

The intra-sample and inter-sample variability, which is regularly observed in the experiments with proteins, might be reduced, or controlled, only once the exact correlation among most of the above-mentioned factors had been satisfactorily clarified. That is, the above variability might, in fact, become an insurmountable obstacle to adequate data interpretability, which, inevitably, necessitates good data repeatability. Furthermore, it is also well known to the scientific community that the higher is the number of experimental steps performed the greater is the chance that errors occur during an experimental procedure. Indeed experimental errors do determine poorly repeatable results. Additional details on this issue, and the reasons why this should be kept under control, are summarized in the flow chart of Fig. 6.3.

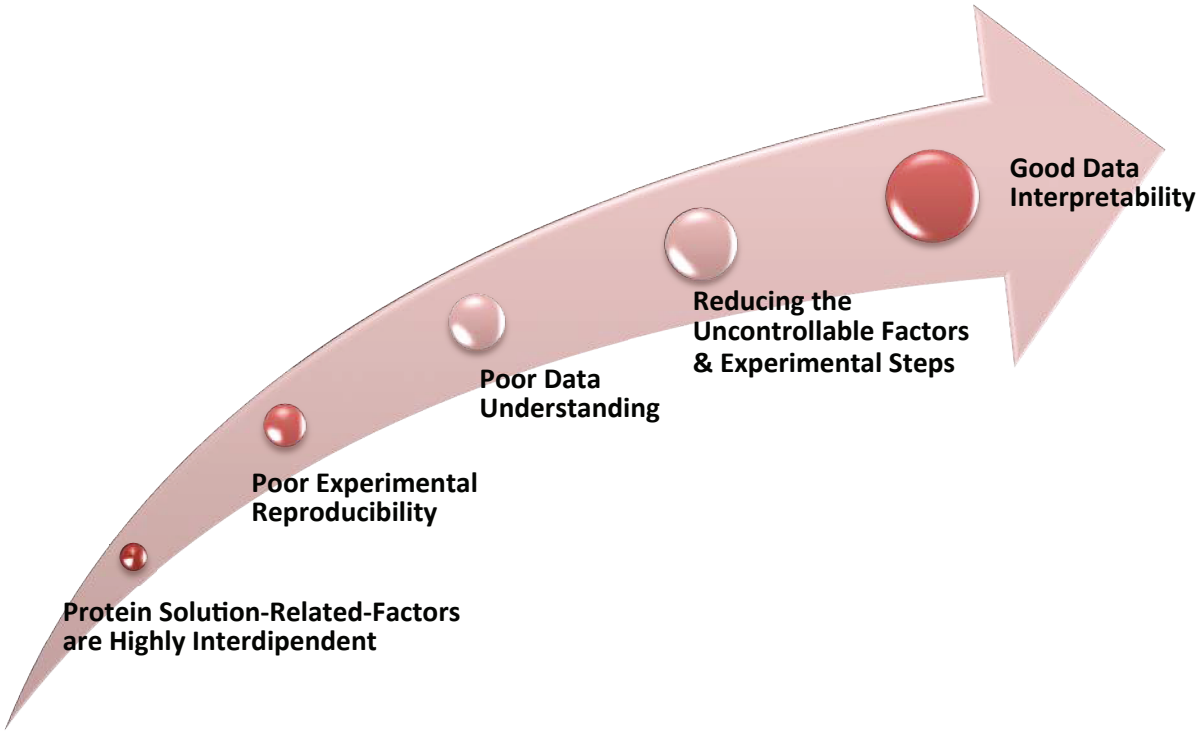


Fig. 6.3 *The repeatability issue is, intrinsically, associated with performing experiments on proteins, (Agnese Zicari ©, 2010).*

6.1.3 Reducing the uncontrollable factors

As a result of the aforementioned repeatability issue, unwanted uncontrollable factors (such as the salt excess, the air droplet entrainment at the solid-liquid interface and the dust contamination) should be carefully regarded before planning any work on proteins. That is, methods and procedures to reduce (and, possibly, extinguished) unwanted interference factors should be developed before starting any experimental characterization work on the lysozyme metastable region and the relating dynamics at the solid-solution interface.

6.1.4 Making simple procedures to manufacture MEMS-type substrates

Hence, as a result of the aforementioned repeatability issue, simple manufacture procedures to make MEMS-type substrates have, also, been outlined in this work. The main scope of these procedures is to permit the manufacture of reproducible batches of nano-patterned substrates. Indeed, it is well known that given the high precision that is necessary to manufacture this type of substrates, the probability of error during their manufacture is quite high. That is, this alone might induce additional repeatability issues during the protein heterogeneous crystallization tests. In fact, the surface pattern manufacture is often part of a broader experimental procedure (since these surfaces are, often, used as substrates for proteins). Subsequently, highly repeatable nano-patterning techniques have been chosen for this work and procedures to reduce the total number of experimental steps have been outlined.

6.1.5 Homogeneous vs. heterogeneous crystallization times

Homogeneous and heterogeneous crystallization times are also investigated. That is, different experiments have been designed to estimate the protein (and precipitant) concentration that is necessary to reveal the effect of the solid surface structure on the protein heterogeneous dynamics. As explained in section 6.1.1, the clustering of proteins in the bulk is, also, governed by highly interrelated and non-controllable solution factors. However, the predominance of one or more factors may impede the discernment of this interplay. Excessive concentrations, for example, might blur the distinguishing of this multi-factorial interaction.

6.2 Reduction of Unwanted Interference Factors

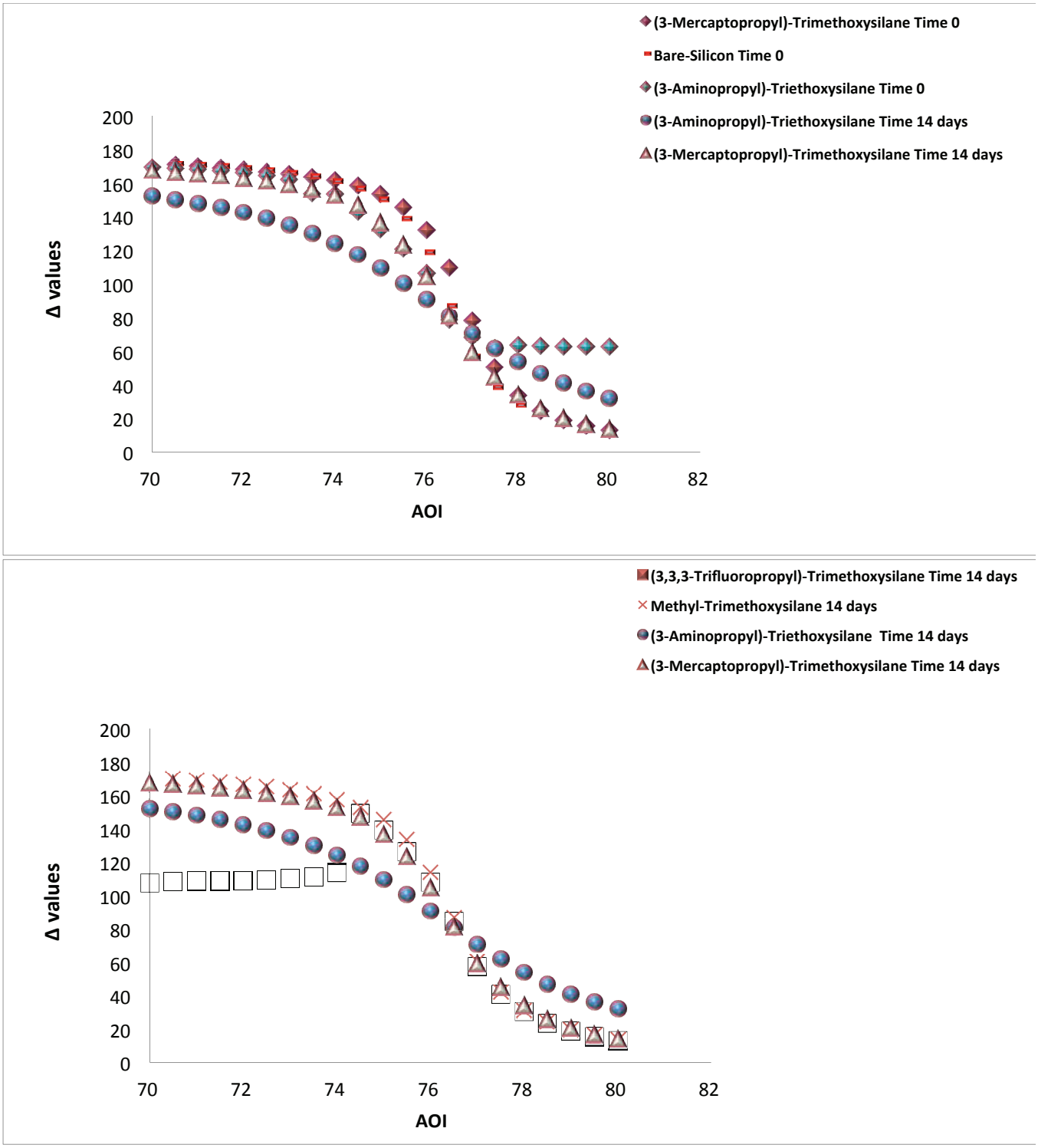
6.2.1 Reduction of the salt interference in the nucleating solution

According to section 2.1.2 lysozyme follows an ideal behaviour only at lower salt concentrations. Also the experiments in this work suggest the interference of the co-solutes from the conventional precipitant solution on the adsorption, and heterogeneous nucleation, of lysozyme. Indeed, after testing the surfaces that had been exposed to the conventional precipitant solution (which is well described in section 5.1) with a broad range of techniques, the formulation proved to be unsuitable for this work.

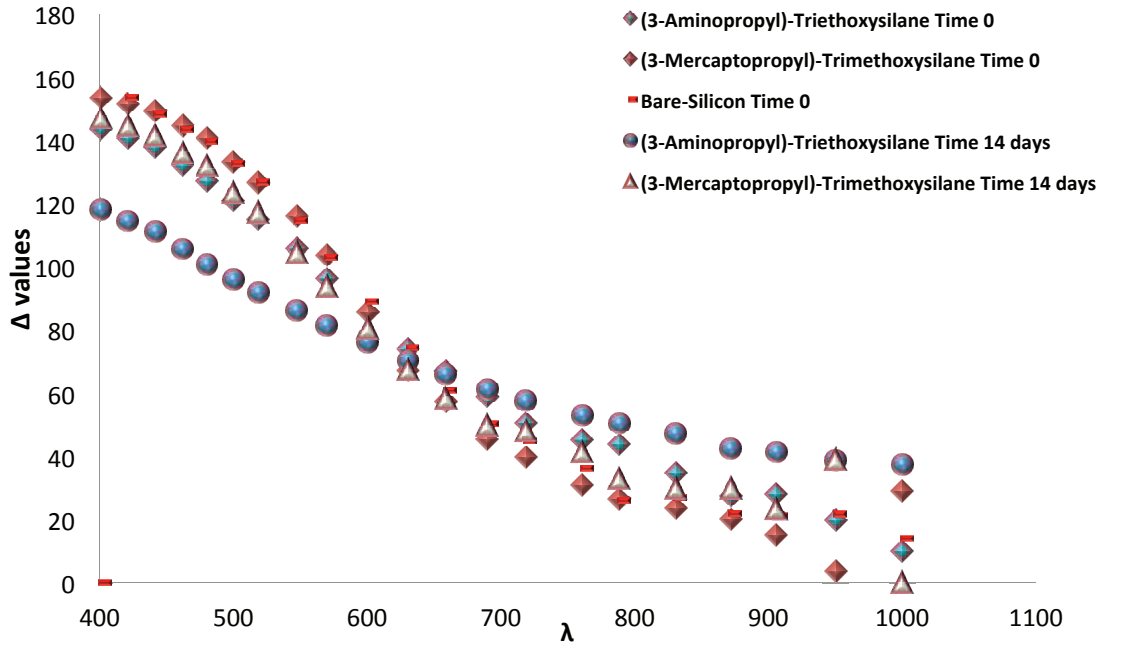
As expected, the results from the above experiments confirm that a number of non-controllable factors often alter the dynamics of protein adsorption (and heterogeneous nucleation) at the solution-solid interface. That is, the interplay between the co-solutes from the conventional precipitant solution and, possibly, other non-controllable factors that might arise at the solid-liquid interface, induce the above alteration. The experimental technique that has, first, suggested the co-solute interference, in this work, is ellipsometry. An ellipsometer EP3-v230, which was provided with 532 nm laser source and a white light source, was used in this work. In these experiments an initial AOI (angle of incidence) of about 60° was set for the linearly polarised laser beam. The surface of the samples was, either made of bare silicon (100) or it had been previously modified by means of activation, silanization, and curing procedures. After curing, the samples were, first, exposed to the conventional precipitant solution in drastic conditions (i.e., 14 days), then rinsed with distilled water and dried in a desiccator for 24 hrs.

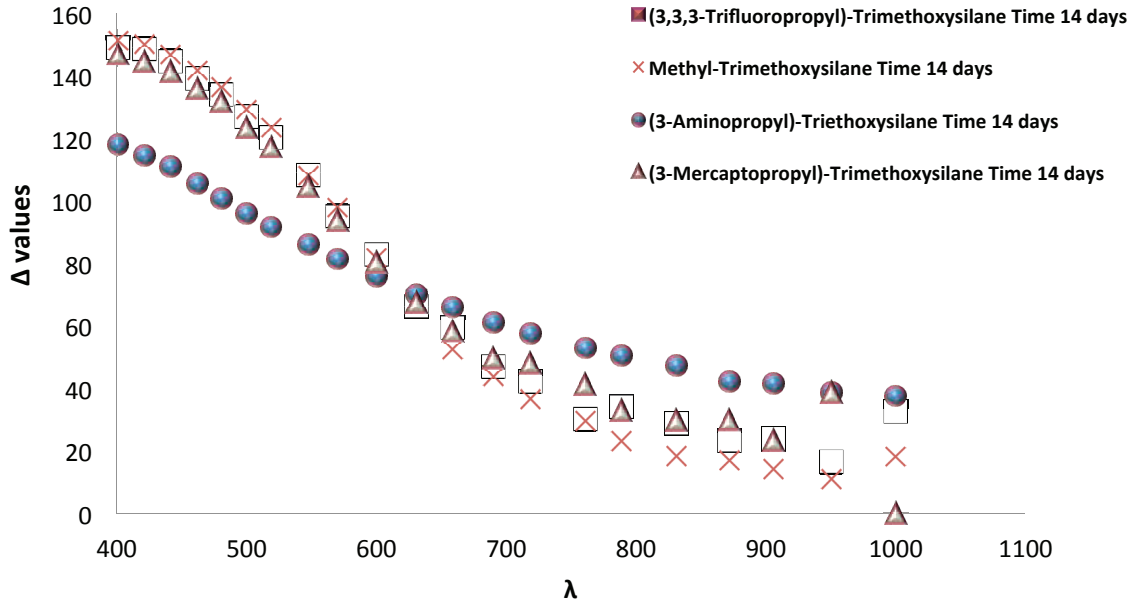
Some of the measurements have been plotted in Fig. 6.4. In these diagrams the delta values before, or after exposure, have been plotted against the AOI, or λ, values. After comparing the results of the different silanized surfaces, it has been inferred that the interference effect that follows the exposure to the precipitant solution also depends on the initial surface energy. Indeed, this effect appears to be more evident on the 3-aminopropyl-

triethoxy (or 3,3,3-trifluoropropyl-trimethoxy substituted) surfaces. Also, this technique is not suitable to test surfaces with nano-structures. All the experiments, which were performed on even surfaces, suggest that the co-solutes may well interfere with surface-induced processes.



(a)





(b)

Fig. 6.4 *The ellipsometric analyses represent the delta values (Δ) against the lambda (λ) or angle of incidence variations (AOI) for the silanized surfaces before & after exposure to the precipitant solution. The 3-aminopropyl-triethoxysilane (◆) and 3-mercaptopropyl-trimethoxysilane (Δ) treated surfaces before exposure, for the samples in* ***(a)*** *and* ***(b)****. The 3-aminopropyl-triethoxysilane (●), 3-mercaptopropyl-trimethoxysilane (◆), 3,3,3-trifluoropropyl-trimethoxysilane (■) and methyl-trimethoxysilane (x) treated surfaces and the bare-silicon (-) surface after 14 day exposure to the precipitant solution, for the samples in* ***(a)*** *and* ***(b)****, (Agnese Zicari ©, 2009).*

Following the above-mentioned observations, additional techniques, and methods, have been used to further test the salt interference on plain, or silanized, silicon surfaces. The substrates for the following tests were prepared according to the here below procedure:

1. exposure to a sodium chloride/acetate buffer solution (4 hrs),
2. rinsing with distilled water,
3. drying in a desiccator for 24 hrs.

These tests were performed on plain silicon (100) surfaces (by means of a Veeco Wyko optical profilometer, with 160 nm resolution, or a Leica TCS-SP UV microscope) and on silanized surfaces (by means of a grazing angle IR Analysis, with the equipment and settings that have been specified in section 5.1). Both techniques have provided additional evidence of salt adsorption at the solution-solid interface, which is, very probably, induced by the elevated salt concentration in the precipitating solution.

As a result of this, a new set of experiments was planned to replace the conventional precipitating formulation (which was used to crystallize lysozyme at the beginning of this work) with an in-house surrogate. The new formulation was prepared to attain ideal bulk nucleation conditions (that is, very low ionic strengths and fast crystal growth rates) and to reveal the effect of solid-liquid interfaces bearing different chemistry and morphology on the lysozyme nucleation rates. That is, according to the sections 3.1 and 6.1.5, the heterogeneous nucleation rates, rather than the crystal growth rate, would be the major variable of interest to determine the aforementioned surface effect. Indeed, also the nucleation pattern at the interface might be monitored in relation to the above nucleation rate.

The preparation of the new formulation involved several trials (with different buffering or precipitants), however, all the salt additives were chosen in accordance with the traditional theory on biomolecule salting-out. After a few screening trials a new precipitant formulation has been prepared by mixing a volume of 50 mM borate buffer, with an equivalent volume of a 9.16 – 14.88 % v/v solution of a 0.6 % w/v sodium nitrate solution in a 50 mM borate buffer solution. Also, it is worth pointing out that the 0.6 % w/v sodium nitrate

solution is at the top limit of this salt solubility. Therefore, although only few ml fractions of this solution are dispersed in the borate buffer before use, this solution has been filtered also before starting the procedure to prepare the precipitant solution, (Agnese Zicari ©, 2009).

6.2.2 Reduction of the air droplet entrainment and dust contamination by the interface

The entrainment of air droplets on the surface nano-patterns has been well observed in the literature (Martines et al., 2006). Furthermore, given the probabilistic scenario that is distinctive for all protein solutions, the conformationally active monomers may, alone, act as surface active agents at the air-water interface. This interface activity may, very probably, manifest as a gradient around each air droplet and induce a Marangoni stress effect at the air/lysozyme-solution interface. That is, according to Takagi et al., 2011, the above-mentioned stress effect well hinders any progression of the air-droplet surface within the solution, and, hence, out of the nano-pattern. This would also explain why the scenario, which is represented in Fig. 6.5, is statistically significant. Hence, the subsequent interference with the interfacial phenomena at the solid-solution interface may well alter the repeatability of the experiments on the protein dynamics at the above interface.

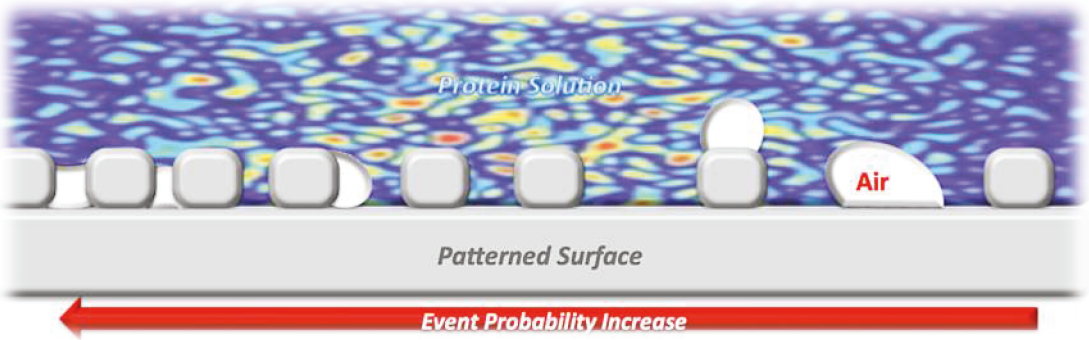


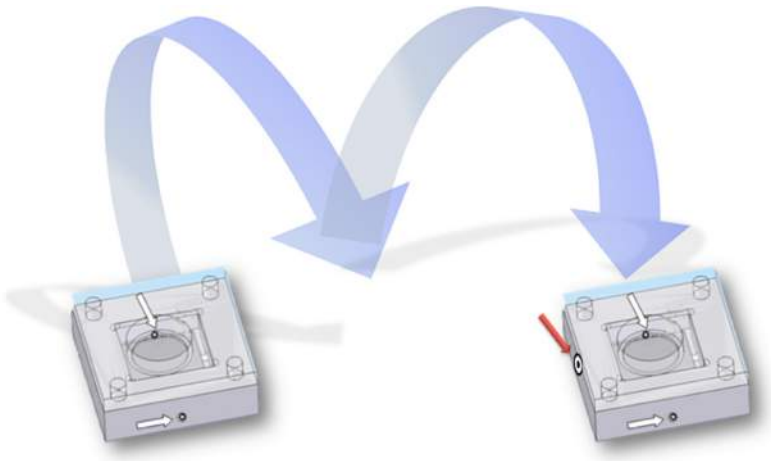
Fig. 6.5 *A sketch representing how air droplets may interfere with interfacial phenomena, (Agnese Zicari ©, 2010).*

As a result of this, the use of conventional protein crystallization techniques has been regarded as obsolete in relation to so specific a project. That is, most of the protein crystallization experiments were performed by means of an air-depleted micro-batch method. Though some initial protein crystallization trials had been simply performed by means of 2

microscope slides holding a seal. The latter had been previously firmed on one slide with an epoxy-resin. This provisional arrangement was difficult to use because of evident repeatability issues. The 3-D-Solid-Works design of different micro-batch devices was performed to build an apparatus that, ultimately, ensured the elimination of any air droplet entrainment by the interface of interest. All the manufactured devices presented:

1. an airtight top quartz window, (component 1)
2. an airtight bottom slide holder (25 × 25 mm holding place), (component 2)
3. an airtight few ml internal tank (if component 1 is mounted on component 2)
4. a couple of airtight (inlet & outlet) apertures

The component 1 and 2 were moulded in PTFE according to the above description. That is, the above-mentioned designs differ, especially, in the type, and the position, of the apertures. The most recent 3D-Solid-Works models are shown in Fig. 6.6. Differently from the previously manufactured devices the proposed new design features 2 inlets and 1 outlet, since this permits the access of vapour through one inlet after creating vacuum by the outlet and the injection of the low-salt crystallizing lysozyme solution through the other inlet.



Latest Design Proposed New Design

Fig. 6.6 *The micro-batch crystallization devices that have been designed and manufactured in-house. The most recently manufactured design is shown on the left and a proposed new design is shown on the right, (Design and model by Agnese Zicari ©, 2009).*

The use of the above device during the crystallization trials was, finally, arranged so that a 220 nm cut-off filter had been screwed to an airtight syringe on one side and to the device on the other side. That is, a syringe with filter was used to inject the protein solution, while a second

syringe with filter was used to apply vacuum from the device outlet. Moreover, dust contamination was, also, prevented before injection by mounting the device in a clean room.

6.3 A Simple Procedure to Manufacture Controlled Surface Features

Following the first use of MEMS & NEMS for bio-applications (Carter, 1967) and the break-through of this use (Whitesides, 1993), any progress in the manufacture of nano-patterned surfaces aims to make larger areas of surfaces with highly controlled features. Indeed, as explained in section 6.1.1 and 6.1.2, substrates with highly controlled features help to ameliorate the intra-sample repeatability of heterogeneous nucleation experiments. However, highly accurate procedures are also necessary to ensure inter-sample repeatability (that is, these procedures should ensure the manufacture of substrates with highly reproducible features).

6.3.1 Introduction

The use of surfaces with highly controlled features is regarded as indispensable for this work. Indeed, an ideal surface is both chemically & morphologically homogeneous, while a real surface presents nano-scale chemical & morphological inhomogeneity. That is, on a real surface the location of certain adsorption, or structuring, dynamics is determined by the solution and the surface local parameters likewise. This is further detailed in Fig. 6.7.

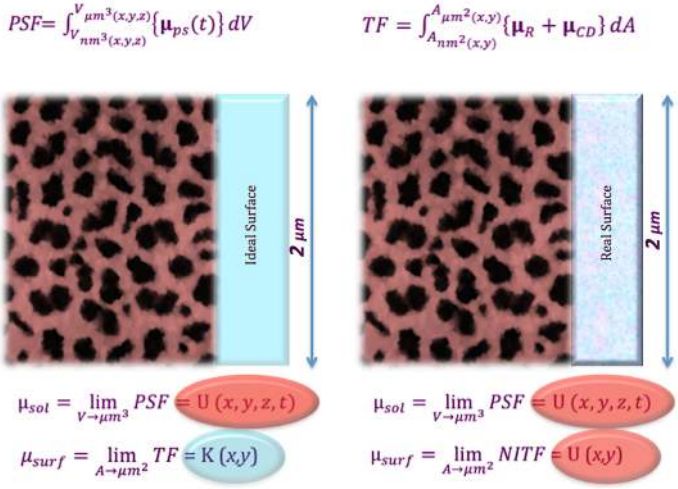


Fig. 6.7 *In the picture;*
A is the area, V is the volume, t is the time and x, y, z are the Cartesian variables.
PSF and TF are the protein solution and topographic factors (respectively);
μ_{ps}, μ_R and μ_{CD} are the chemical potential contributions of the protein solution, surface roughness and surface chemistry (respectively);
μ_{sol} and μ_{surf} are the solution and surface chemical potentials (respectively);
U and K: are unknown and known variables (respectively),
(Agnese Zicari ©, 2014).

As a result of this, specific nano-patterning techniques (and methods) were selectively chosen to manufacture the substrates for this work. As explained, this was, primarily, to reduce the number of experimental steps and ensure little inter-sample and intra-sample variability. Also, the use of surface chemical modification techniques in the vapour phase has been, generally, preferred for the same reason.

6.3.2 The manufacture of substrates by nano-imprinting

A 6 inch and 600 nm thick silicon (100) wafer was used to make 5 × 5 mm substrates with 180 nm groves. The wafer was manufactured in the Obducat AB clean rooms according to the following protocol, (1):

1. a Si mask was covered with a tridecafluoro-1,1,2,2-tetrahydrooctyl-1-trichloro-like silane, (via CVD).
2. the Si mask was replicated onto PDMS to form a soft stamp (via hot-embossing).
3. a 6" and 600 nm thick Si (100) wafer was spin coated with an epoxy-polymer layer.
4. the PDMS stamp was used to imprint 180 nm periods in the polymer (Sindre 400).
5. the imprinted epoxy-polymer layer was cured with a patented two-stage process.
6. the pattern features and weaviness were characterised according to section 4.2.2 (with an AFM Veeco-3100 in tapping mode, first, and with a surface profiler Kla-Tencor P15, afterwards).

The wafer was, thereafter, diced into 5 × 5 mm substrates according to the following procedure (Agnese Zicari ©, 2010):

1. The patterned wafer was mounted (in a class-100 clean room) on a 7" & 5 mm thick glass.
2. The patterned side of the above-mentioned wafer was facing the glass while the backside was firmed up with anti-static tape.
3. A stealth-dicing type laser-cut, that is, a thermally induced crack propagation method, was applied from the back down to 2/3 of the wafer thickness (HM1400 by GSI Lumonics). The wafer after laser processing is represented in the picture of Fig. 6.8.
4. The back of the processed wafer was, thereafter, cleaned (with vacuum, first, and IPA, afterwards) and broken into 5 × 5 mm substrates.

(1) An NDA (i.e., a non-disclosure-agreement) is in place between the college and the company. As a result of this no further details can be disclosed on the Obducat patented processes or on the exact chemical structure of the resin-polymer.

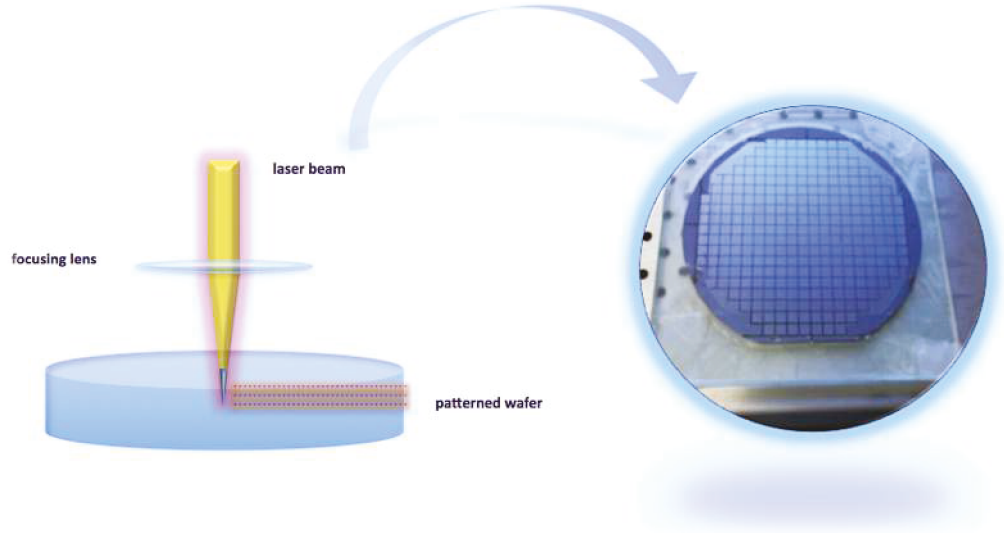


Fig. 6.8 *A representation of the stealth-dicing process (left). A picture of the wafer after stealth-dicing (right), (Agnese Zicari ©, 2010).*

6.3.3 The manufacture of substrates by interference lithography

Additional, substrates with 50 nm dot patterns were manufactured in the Eulitha ltd clean rooms. This was performed according to the following protocol, (2):

- The manufacture of diffraction gratings:

    1. a 100 nm-thick Si_3N_4 membrane was covered with a thin film of Cr, (CVD).
    2. a 40 nm-thick layer of PMMA was spin coated on the Cr film.
    3. the negative resist was polymerized via e-beam lithography.
    4. the non-polymerized negative resist was, thereafter, developed.
    5. the Cr was etched to form ≈140 nm pitch diffracting grooves.

- The use of diffraction gratings to make silicon-based patterns on Si (100) wafer:

    1. a silicone-based negative resist was spin-coated on a 600 nm thick Si wafer.
    2. EUV (λ 13.4 nm) light from a synchrotron radiation source was used to generate 4 coherent light beams after 45° diffraction through a grating system.

(2) An NDA (i.e., a non-disclosure-agreement) is in place between the college and the company. As a result of this no further details can be disclosed on the Eulitha ltd. step & repeat lithography processes.

3. the coherent light beams were recombined onto the spin-coated wafer to form, after interference, a regular pattern of exposed dots. This step is well shown in Fig. 6.9.

4. the non-polymerized negative resist was developed to form patterns of ≈ 50 nm ½ pitches (Eulitha ltd**.** ©, 2010).

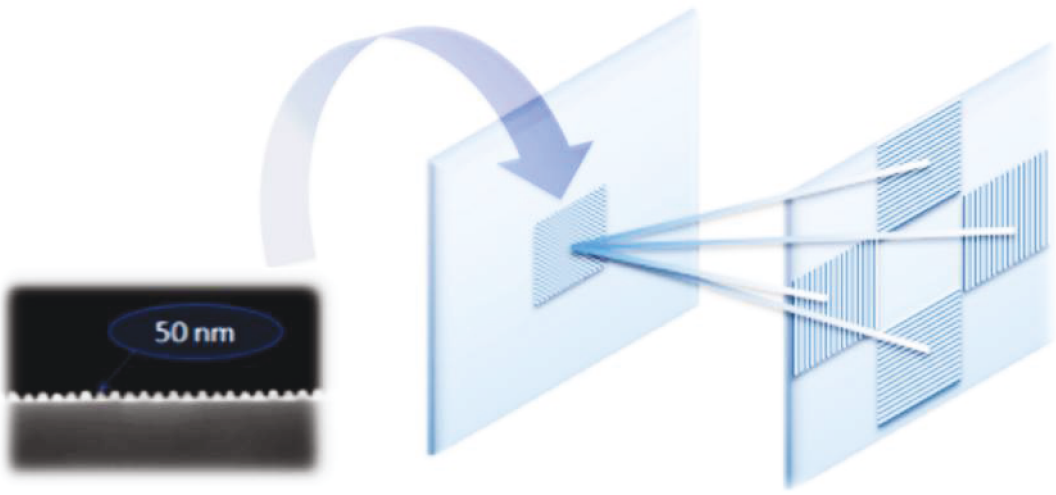


Fig. 6.9 *A representation of the interference lythography process: a EUV light beam is used to generate 4 coherent light beams that, after 45° diffraction, recombine (on the spin-coated silicon based resist) to form, after interference, a regular pattern of exposed dots.*

6.3.4 Surface chemistry modification procedures

The chemical modification of the silicon surfaces was performed according to a 2-step protocol (i.e., a surface activation step and a surface modification step):

- *Surface activation;*

1. This was to generate reactive groups on the surface.

2. This was performed on flat silicon surfaces either with a wet method (by using a specifically formulated Piranha protocol, which is shown in Tab. 4.1) or with a vapour phase method by means of plasma equipment (a Diener equipment or a K1050X plasma asher).

- *Surface silanization;*

1. Wet reaction techniques were tried, in the first instance, as a possible surrogate. Although a CVD would be the first choice method for surface modification, this technique was not available for this work. Also an in-house CVD (that is, without a dedicated equipment) did not generate acceptable intra-sample repeatability values. The wet reaction repeatability was, instead, improved by dispensing the silane volumes with electronic pipets. The following silanes were wet-reacted:

a. 3-aminopropyl-triethoxy silane
b. 3-mercaptopropyl-trimethoxy silane
c. 3,3,3-trifluoropropyl-trimethoxysilane
d. methyl-trimethoxy silane
e. 3,4-epoxy-cyclohexyl-ethyl-trimethoxy silane

The silanization reactions were performed according to the method that is described in Fig. 6.10 and the procedures that are listed in the following sections. The mini-reactor in Fig. 6.10 was filled up to 2/3 of its volume with the reacting acidic solution so that the slide to be reacted was fully covered by this solution after sealing the reactor. Also intra-sample and inter-sample repeatability were further improved by means of a high-speed magnetic stirring method.

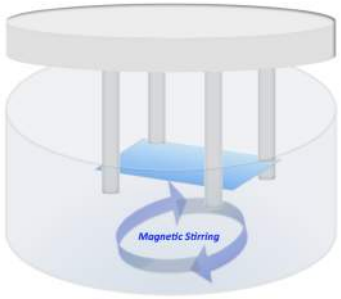


Fig. 6.10 *In this picture a mini-reactor, which was designed and manufactured in-house (PTFE), is shown, (Agnese Zicari ©, 2009).*

The acidic reactions were performed according to the following in-house procedures (Agnese Zicari ©, 2009):

Procedure α

Procedure α	*Description*
Solvent v/v %	12.5 % acetic acid 1M in ethanol-95 % & 87.5 % ethanol-95 %
Silane v/v %	2 % 3-aminopropyl-triethoxy-silane or 2 % 3-mercaptopropyl-trimethoxy-silane
Surface & solution degassing (sonication)	2 – 3 seconds
Reaction time	30 min – 2 hrs
Reaction temperature	RT – 40 °C
Mixing speed	40 rpm

Curing was performed (at 120 °C for 10 hr) only after rinsing the silanized surface with pure ethanol.

***

Procedure β

Procedure β	*Description*
Solvent v/v %	99.34 % absolute ethanol & 0.66 % ammonium hydroxide-28 %
Silane v/v %	2 % 3,3,3-trifluoropropyl- trimethoxy-silane or 2 % methyl-trimethoxy-silane
Surface & solution degassing (sonication)	2 – 3 seconds
Reaction time	30 min – 4 hrs
Reaction temperature	60 °C
Mixing speed	40 rpm

Curing was performed (at 120 °C for 10 hr) only after rinsing the silanized surface with pure ethanol.

***

2. Also, as a result of:

✓ the points made in sections 6.1.1 and 6.1.2,

✓ the averaged CA values in Tab. 4.2. In the latter some of the CA average values from this work have been compared to those from the literature. Both sets have, also, been plotted here below in Fig. 6.11:

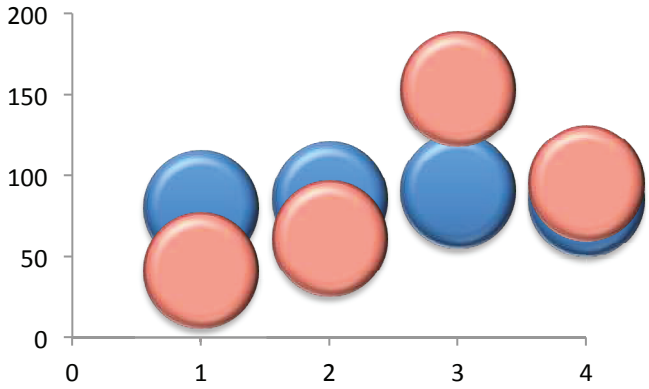


Fig. 6.11 *From left to right the average contact angles of the substrates that were treated with different silanes: 1st, 3-aminopropyl-triethoxysilane; 2nd, 3-mercaptopropyl-trimethoxysilane; 3rd, 3,3,3-trifluoropropyl-trimethoxysilane and 4th, methyl-trimethoxysilane.*

✓ the XPS analysis of the 3,3,3-trifluoropropyl (or methyl) functionalised surfaces (that is, the silanes in c and d at point 1 of this section):

the details relating to sample 3, from the surface composition table in Fig. 4.20, are further reported in Fig. 6.12. In the latter the measurement relating to the 3,3,3-trifluoropropyl-trimethoxysilane functionalised surface shows a fluorinated/carbonated ratio of 0.02 only.

	Sample 3 Dark	Sample 3 light
O 1s	21.3	21.5
C 1s methyl	34.1	34.3
C 1s contamination	24.4	19.7
Si 2p	18.4	22.6
Na 1s	0.1	0.1
F 1s	0.5	0.9
Ca 2p	1.2	1.0

Fig. 6.12 *In this picture the XPS fluorinated/carbonated ratio for the 3,3,3-trifluoropropyl-trimethoxysilane functionalised substrates shows that their surfaces have a highly inhomogeneous chemical distribution.*

✓ the AFM surface analyses was performed in contact mode for all the surfaces of the silanes at point 1 of this section. These, have been performed with a Veeco diInnova AFM and either silicon, or silicon nitride coated, tips depending on the surface hydrophobicity.

The 3,4-epoxy-cyclohexyl-ethyl-trimethoxy silane (in e at point 1 of this section) has been, finally, selected for this work, since this has been deemed appropriate to manufacture surfaces with the same morphology but different hydrophobicity.

The manufacture of the epoxy-surfaces:

Hence, following the points in sections 6.1.1 and 6.1.2 the vapour phase activation, and modification, of flat, and patterned, epoxy-surfaces (with a K1050X plasma asher or a Diener plasma cleaner) was the chosen method to prepare the substrates and perform the following crystallization trials. The second equipment has shown slightly worse average roughness values. Also the flat epoxy-surface, has been necessarily manufactured via wet-silanization after plasma activation. That is, the silanization was performed according to the here below procedure, (Agnese Zicari ©, 2010):

Procedure γ

Procedure γ	*Description*
Solvent v/v %	0.742 % acetic acid-100 % 99.26 % absolute ethanol
Silane v/v %	1.58 % 3,4-epoxy-cyclohexyl-ethyl-trimethoxy-silane
Surface & solution degassing (sonication)	2 – 3 seconds
Reaction time	30 min – 2 hrs
Reaction temperature	90 – 160 °C
Mixing speed	40 rpm

Curing was performed (at 120 °C for 10 hrs) only after rinsing the silanized surface with pure ethanol.

***

Also since the silanes' average viscosity is higher than that of common protein solutions, in the above-mentioned procedures silane volumes were dispensed with electronic pipets after wetting their tips with the same liquid to be dispensed. The latter procedure has been, also, optimised in order to ameliorate the after reaction washing method. It has been previously explained that rinsing is by procedure applied after reaction, that is, before curing. Rinsing the samples in IPA first and ethanol afterwards (or the sonication in ethanol for 5 seconds) have produced lower average contact angles. The initial rinsing method (that is, rinsing the surface with ethanol for 3 times without sonication) has been, hence, preferred. This is also in agreement with the rinsing method that has been performed during the aforementioned procedures.

The pre- and post-silanization activation of the epoxy-surfaces:

As explained in the previous sections the plasma activation method was elected to make both activated surfaces for silanization and hydrophilic chemistries (for crystallization) from the epoxy-surfaces (Walther et al. 2007). The surfaces after pre-silanization activation and epoxy-silanization have been tested with a Kruss Drop Shape Analysis System DSA and ≈12 μl drops. These surfaces were reacted according to the above-mentioned procedures. Also, their power and time of exposure to plasma were calibrated by increasing it from 60 to 70 W and from 40 W to 60 s respectively. Average contact angles in the 57 – 80.3° range were observed. Moreover, the epoxy-silanized surfaces (which had been prepared with a 70 W and 60 s plasma exposure, silanization, rinsing and curing) were chosen for additional testing. Some samples, after curing, were re-exposed to 20W oxygen plasma for 20 s and a 9.8° average contact angle was observed following this. Nevertheless, after keeping these samples in a vacuum oven for 2 hrs at 120 °C the average contact angle values showed different from those that had been recorded immediately after reaction & curing. Hence, since partial corrosion of the silanized layer was inferred the plasma exposure power and time were further decreased to 10 W and 20 s, and, finally, to 10 W and ≈ 4 s. These samples, that had no sign of corrosion, were exposed to the novel precipitant solution for 24 hrs, rinsed (3 times) with water and kept in a vacuum oven for 2 hrs at 120 °C. Their average contact angle values were found reverted to ≈ 80°. Lastly,

it was concluded that the above manufacture and crystallization conditions are appropriate.

Similarly to the silanized flat surfaces, also the epoxy-patterned samples were treated with oxygen plasma and the precipitant solution. Nevertheless, since these samples had undergone the stealth-dicing procedure, they needed to be washed before use. That is, the following cleaning procedures were, first, tested on the epoxy-patterned samples:

1. water
2. water → IPA→ water
3. water → IPA→ aceton → water

Initial signs of possible delamination were observed only in the samples that had been treated with aceton too, and this was in one edge section only. The cleaning protocol at point 2 of the above list was, hence, selected. After cleaning and exposure to oxygen plasma, the patterned epoxy-surfaces showed a 13.6° average contact angle. Also, after 24 hr exposure to the precipitant solution little, or no, sign of delamination was observed. A picture, which is representative of the delamination that was observed by the edge of the diced samples, is shown in Fig. 6.13.

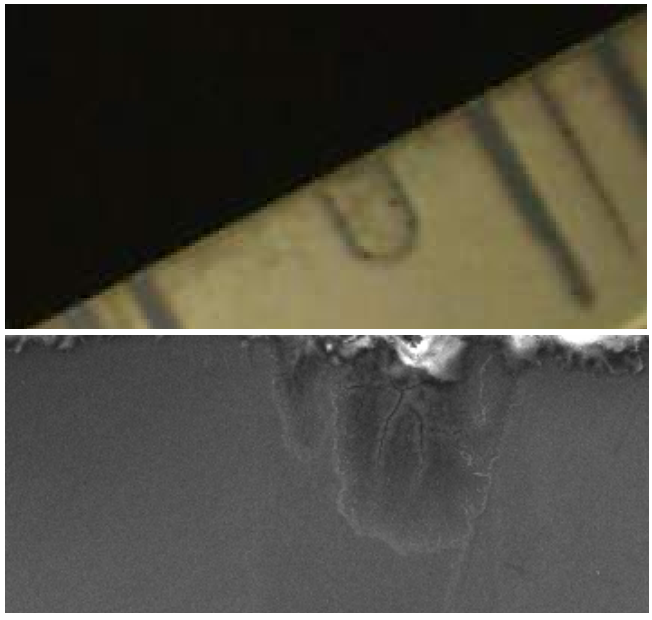


Fig. 6.13 *The optical microscopy* ***(a)*** *& SEM* ***(b)*** *of the patterned epoxy-substrates: the signs of edge-delamination were observed after 24 hr exposure to wet-conditions, (Agnese Zicari ©, 2010).*

The AFM analysis of all the samples was also performed to test the average roughness of the silicon surfaces after oxygen plasma activation and reaction, or to test any possible effect of the crystallization conditions on the surface patterns. The sample surfaces were all tested by sampling 2 × 4 μm areas and 0.5 μm areas within each of the 4 μm areas. The sample average R_a for each type of area size was this way calculated. The average roughness values for flat silicon surfaces before oxygen plasma activation were: 4 μm R_a = 0.0210 (0.5 μm R_a = 0.0094) and 4 μm R_a = 0.0028 (0.5 μm R_a = 0.0028). It is worth noticing an out-layer sample, the average roughness of which before reaction was 4 μm R_a = 0.0468. The average roughness of the silicon even surfaces after oxygen plasma activation (at chosen powers and times) and reaction was also measured, and it was ranging from R_a = 0.0019 to R_a = 0.0143 for the samples' 4 μm areas and from R_a = 0.0013 to R_a = 0.0028 for the samples' 0.5 μm areas. It is, also, worth noting that different reaction protocols (including different mixing methods such as sonication) or repeated reaction protocols have been used before defining the methods and procedures that have been described, earlier in this section. The AFM and SEM analyses of other samples that had been treated similarly to those in Fig. 6.13 (that is, after exposure to plasma, first, and to the precipitant solution, afterwards) were also performed. Also in this case different 4 μm areas were sampled and it was, especially, observed that the areas that looked delaminated under microscopy presented an intact pattern, instead. This is shown in Fig. 6.14.

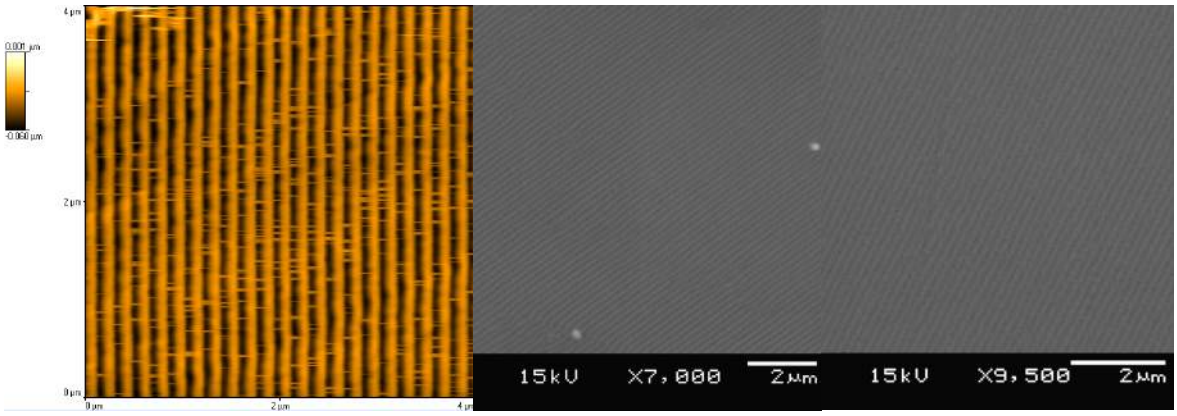


Fig. 6.14 *The AFM analysis of the epoxy-patterned substrates after exposure to the oxygen plasma and precipitant solution (on the left) & the SEM analysis of the epoxy-patterned substrates after exposure to the oxygen plasma only (in the middle), and after exposure to the oxygen plasma and precipitant solution (on the right), (Agnese Zicari ©, 2010).*

6.4 Comparing Homogeneous vs. Heterogeneous Crystallization Times

6.4.1 Making ➔ characterising the low-salt formulation & implementing the air-depleted method

As explained in section 6.1 of this chapter a new formulation has been developed. This formulation allows to test the heterogeneous crystallization in an environment that is fairly close to the ideal crystallization conditions. The choice of the final salt additives has been performed after trying different salt formulations that conform to the traditional theory on biomolecule salting-out. After a few screening trials, a new precipitant formulation with very low Jones-Dole B-coefficient has been prepared. The finally formulated solution features low ionic strength, low lysozyme concentration and fast crystal growth times and it has been prepared according to the following procedure (Agnese Zicari ©, 2009):

Procedure δ

Procedure δ	*Description*
(A) Lysozyme buffer solution	preparation of the lysozyme solution (10 mg/ml) in 50 mM borate buffer
Filtration of (A)	0.22 μm
(B) Precipitant solution	pipetting 9.16 – 14.88 % v/v of a sodium nitrate solution (0.6 % w/v) in 50 mM borate buffer solution
Filtration of (B)	0.22 μm
Mixing (A) & (B)	mild mixing of equal volumes of (A) & (B); i.e., no shaking or magnetic stirring
Filtration	0.22 μm at 20 – 25 °C

***

The aforementioned 4.58 – 7.44 % v/v concentration range (in the final crystallizing solution) has been delimited as in this range of precipitant concentrations crystallization was observed for all the tested lysozyme concentrations (5 mg/ml, 10 mg/ml, 15 mg/ml and 20 mg/ml). Also, during the work following this screening specific protocols have been applied to ameliorate the repeatability of the experiments. The main protocols are listed here below:

- using clean laboratories for most of the experimental steps (class-100 clean rooms).
- dispensing lysozyme powder with analytical scales.
- filtering dust out of all the rinsing water with 0.45 μm before use.
- filtering all the buffer, precipitant and protein solutions with 0.22 μm filters.
- dispensing the protein solution and precipitant solution with electronic pipets.
- rinsing & drying the pipet plastic tips and wetting these before use.

The lysozyme crystals of the 5 mg/ml solution after 24 hr at RT are shown in Fig. 6.15.

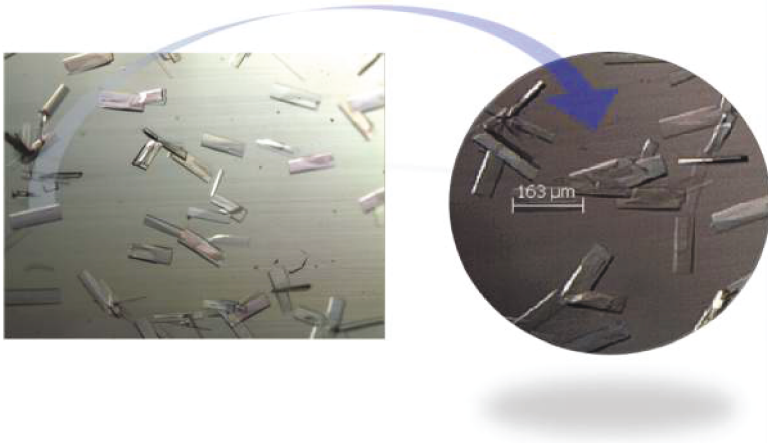


Fig. 6.15 *The light microscopy of the lysozyme crystals that have formed from the 5 mg/ml solutions after 24 hrs at RT, (Agnese Zicari ©, 2010).*

X-ray Crystallography Procedure

A lysozyme crystal was also tested via x-ray analysis (i.e., with a Rigaku Micromax 007HFM):

1. a lysozyme crystal was chosen and observed with an optical microscope.
2. the crystal was picked up from the lysozyme solution with a cryo-pin loop.
3. the cryo-pin loop bottom was thereafter re-inserted on the equipment between the x-ray-collimator (with a set focal spot size of 100 μm) and the beam detector at a 50 mm distance.
4. a cryo-stream was generated from a top nozzle to hit the crystal before exposure to the x-ray (5s).
5. during exposure the goniometer was set to rotate the crystal from/to selected orientations (±45°).
6. data relating to the Ewald sphere were recorded; as expected, the sphere of reflection looks concentric only in Fig. 5.4-b_2, where the x-ray beam is 90° oriented with respect to the lattice plane reflection set.

***

The meaning of the sphere of reflection dots is further explained in Fig. 6.16.

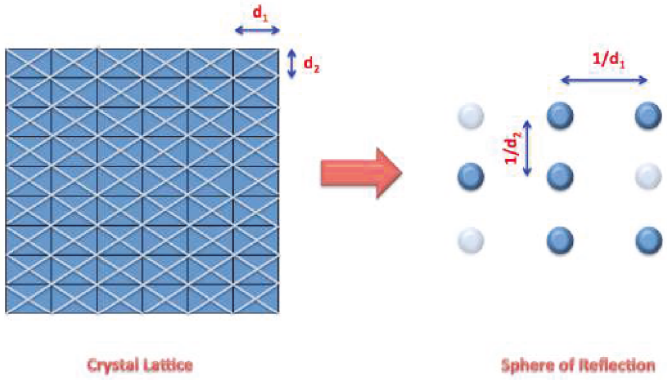


Fig. 6.16 *A section of the reflection sphere, which is generated through a crystal lattice plane set.*

6.4.2 Designing & testing the robustness of the air-depleted micro-batch method

The 5 mg/ml lysozyme solution was also crystallized in the device, which is described in Fig. 6.5. A procedure for this has been, also, drafted (Agnese Zicari ©, 2010):

Procedure ε

Procedure ε	*Description*
The lysozyme crystallising solution preparation (procedure δ)	lysozyme (5 mg/ml) in 50 mM borate buffer after addition of precipitant
5 × 5 mm substrate cleaning	water → IPA→ water rinsing and compressed air drying in class-100 clean rooms
5 × 5 mm substrate firming-up	the 5 × 5 mm substrate is firmed-up on a clean 25 × 25 mm glass slide by means of natural wax in class-100 clean rooms
Device mounting	the device component-1 & component-2 are sealed in class-100 clean rooms
Out-let	vacuum is applied with an airtight syringe (with filter)
In-let	the crystallizing solution is manually filtered & injected with an airtight syringe
Crystallization	the sealed and filled device is turned positioning component 2 above component 1 at 5 °C or RT (20 – 25 °C)

***

According to the trials that have been mentioned in chapter 5, the patterned hydrophobic surfaces induce faster heterogeneous nucleation, and crystal growth, in a few hours only (while the relative homogeneous crystallization has been observed after 24 hrs). As a result of this, the metaphase behaviour of the bulk solution before heterogeneous nucleation has been also characterised by DLS (Malvern Zeta-Sizer-Zen 3600). Indeed, the bulk and heterogeneous nucleation phenomena are highly correlated, and this is also explained in Fig 6.17. The spinodal decomposition (which is well described by Debenedetti) derives from a bulk metastable phase, which generates local but not global minima for the ensemble free energy, (Campbell, 2012). Each minimum of energy resists to small mass fluctuations (as within that minimum the Brownian motion does not apply). That is, a correlation between the pattern of the local bulk concentrations and the heterogeneous processes at the solid-liquid interface may be, indeed, envisaged (Fermani et al., 2013). A version of the Cahn-Hilliard equation (which is briefly noted down here below) may simply visualize the above bulk pattern and correlation:

$$\partial c/\partial t = D\nabla^2\mu \qquad (6.1)$$

According to the above representation the time related solution concentration fluctuations generate a time related chemical potential gradient $\nabla^2\mu$ (where $\mu = c^3 - c - \gamma\nabla^2 c$ depends on both a nominal concentration and a concentration induced surface tension gradient, γ) and a surface diffusion coefficient D, (i.e., D = length^2 / time).

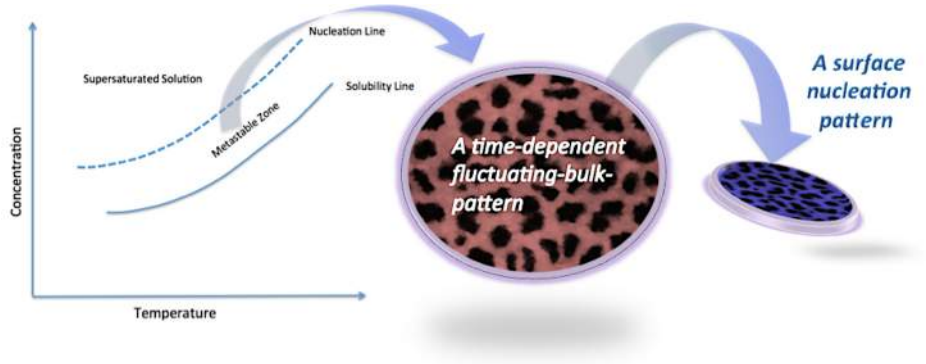


Fig. 6.17 *A metaphase nucleation model; it describes time-related protein-mass fluctuations, (Agnese Zicari ©, 2011)*

The DLS of lysozyme solutions during crystallization

In this work some DLS measurements of the crystallising solution behaviour in the hours before (and after) the heterogeneous crystallization initiation have been performed. Indeed, few hundred μm crystals form, in the micro-batch device bearing nano-patterned substrates, around time 4 – 5 hrs after injection. Notwithstanding the limitations of the equipment that was available in 2010, a Malvern Zen-3600, the DLS results have been satisfactorily understood. It may be, in fact, inferred that, though this might be statistically negligible, ordered structuring is favoured at lower concentrations. That is, larger structures appear to form at lower concentrations. The DLS samples were prepared according to the following procedure (Agnese Zicari ©, 2010):

Procedure ζ

Procedure ζ	*Description*
Dust-rinsing	the (new) disposable DLS cuvettes were rinsed with ethanol → water and dried with compressed air in class-100 clean rooms
The lysozyme crystallising solution preparation (procedure δ)	Lysozyme (5 mg/ml, 10 mg/ml and 20 mg/ml) solutions in 50 mM borate buffer after addition of precipitant
Cuvette filling & sealing	the cuvettes were filled up to 2/3 and sealed with caps in class-100 clean rooms
Cuvette placement in Zeta-Sizer-Zen 3600 (with a 532 laser source)	the sealed cuvettes were placed in the DLS equipment at RT (25 °C) and other standard settings (90°)
Measurement	3 each hr for the first 4 hrs

***

The lowest concentration was filtered also with finer cut-off filters (5 nm, circa, dead-end filters and 10 nm, or 20 nm, cross-flow cut-off filters). The 4.58 – 6.00 % v/v precipitant concentration range was regarded in these DLS experiments (the 5.67 – 6.00 % v/v range was, especially, regarded). Initially, the filtered blank buffer solution and the 6.00 % v/v blank

precipitant solution were, also, tested by DLS. According to the results relating to these tests, some intensity scattering is clearly visible for both blank solutions in the 0.1 nm – 0.9 nm and 164 nm – 190 nm mean size ranges. Indeed, this artifact has no real, or very little, interference with the scattering of the protein monomers and it is in agreement with the limitations of this technique (or equipment). As a result of this all the following experiments results were not interpreted as particle size measurements, but, primarily, as measurements of reversible scattering patterns. All the DLS experiments were performed according to the following general procedure (Agnese Zicari ©, 2010):

Procedure η

Procedure η	*Description*
Dust-rinsing	the (new) disposable DLS cuvettes were rinsed with ethanol → water and dried with compressed air in class-100 clean rooms
The lysozyme crystallising solution preparation (procedure δ)	(5 mg/ml) lysozyme solution in 50 mM borate buffer after addition of precipitant (220 nm cut-off filtration)
Cuvette filling & sealing with additional sample filtration	the solution was filtered (with 5 nm, circa, dead-end filters and 10 nm or 20 nm cross-flow cut-off filters) and the cuvettes were filled up to 2/3 (and sealed with caps) in class-100 clean rooms
Placing in Zeta-Sizer-Zen 3600 (with a 532 laser source)	the sealed cuvettes were placed in the DLS equipment at 90°, RT (25 °C) and other standard settings
Measurement	3 each hr for the first 4 hrs

***

The sample filtration was performed in agreement with the following procedures (Agnese Zicari ©, 2010):

Procedure θ

Procedure θ: filtration with 10 nm and 20 nm cut-off cross-flow filters

1. preparation of a (10 mg/ml) lysozyme solution (procedure δ)
2. rinsing the disposable cuvettes with filtered distilled water (0.45 μm) in class-100 clean rooms
3. drying the rinsed DLS disposable cuvettes with compressed air in class-100 clean rooms
4. assembling a PLC disc membrane & syringe adaptor in class-100 clean rooms

5. rinsing the mounted membrane with the buffer solution in class-100 clean rooms
6. diluting the (10 mg/ml) lysozyme to 5 mg/ml according to procedure δ
7. rinsing the buffer dead-volume out with this lysozyme solution in class-100 clean rooms
8. filtration of this solution straight into the clean DLS disposable cuvettes in class-100 clean rooms
9. sealing the DLS disposable cuvettes in class-100 clean rooms

***

A dead-end filtration with molecular cut-off just below the lysozyme monomer molecular weight (MW) was also performed according to the following procedure:

Procedure ι

Procedure ι: filtration with "5 nm" (i.e., 10 kDa LMW cut-off) dead-end filters

1. preparation of a 5 mg/ml solution (procedure δ)
2. preparation of a (0.25 mg/ml) lysozyme solution via dilution of 1ml of a 5 mg/ml solution in class-100 clean rooms
3. rinsing & drying the ultracentrifuge filter internal tube with filtered distilled water (0.45 μm) in class-100 clean rooms
4. dispensing of 12ml of the solution (after a 220 nm cut-off filtration) in the dead-end filter tube in class-100 clean rooms
5. dispensing 12ml of blank buffer in a simple centrifuge tube
6. placing (and balancing) the filled ultracentrifuge filter tube in a centrifuge
7. centrifugation at ≈ 4000 x g for about 20 min
8. recovering the concentrated sample while adding buffer down to 10 mg/ml in class-100 clean rooms
9. adding an equivalent volume of the filtered precipitant solution B (procedure δ) in class-100 clean rooms
10. filtration (again with a 220 nm cut-off filter), collection of this solution to fill DLS cuvettes up to 2/3 (and sealing these with caps) in class-100 clean rooms

***

The use of modern filtration procedures and the tests on the filtered 5 mg/ml lysozyme solutions have demonstrated that the intensity scattering % that is observable immediately below 1000 nm is clearly visible also in all the samples that have been filtered with 220 nm cut-off filters only. Indeed, according to Parmar et al. (2007), 100 nm size or smaller contaminants might be present in commercially lyophilised lysozyme products. After using lower cut-off filters to investigate the intensity scattering below 1000 nm, it has been concluded that the observed scattering should be related neither to dust particles (which, generally, have sizes of ≈ 0.5 μm) nor to pre-nucleated lysozyme. That is, according to the correlation data in Fig. 5.5 and the intensity scattering data in Fig. 5.6, the observed peaks are

qualitatively related, primarily, to the particle size distribution of the lysozyme monomers in solution. However, the intensity scattering data for the samples that have been filtered with the low cut-off filters in Fig. 5.6 do look different in that the peak repeatability with respect to time seems very poor. That is, notwithstanding the equipment limitations (single angle DLS), it appears that the scattering may be related to dynamically reversible local scatterers that generate a broad range of mean scattering intensities. Indeed, the changes in the solution local polarizability result from the different geometries and permittivity values that are, primarily, induced by the clustering of monomers. Nevertheless, depending on the solution time-dependent local dynamics, reversible structures may, also, evolve from the interaction of solute, co-solute or solvent, and these, alone, may induce the above changes. Even the nucleated crystals may contain over 50 % solution within their structure. As a result of all this, and according to section 5.2, the measurement of the local electromagnetic response of each infinitesimal solution scatterer is only a polarizability related, and field-induced, dipole moment. That is, this might indicate either a particle aggregate or a locally structured solution element. Therefore, the poor repeatability of the 2^{nd} peak (which is observed for the finely filtered, and low protein content, solutions) may, also, indicate solvent-solute structures that, reversibly, break as a result of different time-dependent equilibria.

In addition to this interpretation, soliton like dynamics may be also suggested. With respect to this highly specific topic, the Davydov Model has been often referred to in the literature. Though, so far, a complete soliton physical model for proteins has hardly been defined (Cruzeiro-Hansson et al., 2001). A possible soliton like response would be primarily related to the protein monomer α-helical content, where the H–N–C=O groups link together to form sets of three continuous chains. A few researchers (Radford et al., 1992; Klimov et al., 2003; Ricchiuto et al., 2012) have modelled the development of α-helical structures, for α-helical (or β-sheet) forming peptides, in the assembled oligomer or while assembling. Indeed, the H–N–C=O groups align within the α-helical ordered structures and, as a result of this alignment, the local amide-vibrational energy and their longitudinal deformation can travel

along the chain without determining any energy loss. That is, differently statistically significant energy levels may generate. Indeed, the lower energy antisymmetric solitons are regarded as statistically more significant. Moreover, according to the deductions from chapter 5, combined excitations may behave as if these were particles. That is, very likely, infinitesimal ordered solution ensembles feature local soliton-like behaviours (El-Ganainy et al., 2007).

In the light of this, the data relating to the peaks from the DLS plots of chapter 5 might be reinterpreted. That is, these might be regarded as the time-related snapshots of the responses, that stem from the solvent-solute (or co-solute) structuring to a given intensity beam. Also, these are statistically determined data, as they represent a dynamically diverse gradient of locally reversible (or irreversible) low energy equilibria. Also, one of the instantaneous intensity scattering patterns from chapter 5 is also sketched in Fig. 6.18. The latter shows how the intensity scattering data of a 20 mg/ml lysozyme solution sample can be visually correlated to the correlation coefficient decay (against time) for both the intensity-related absorption peaks. The correlation statistical method is, generally, applied in DLS to explain that data are not randomly determined. Indeed, one particle of a certain size (i.e., featuring a slow decay) gives intensity scattering data in the higher size range, though the intensity scattering by smaller particles (i.e., featuring faster decay) may well induce destructive interference. That is, these scatter at a fast decay rate as they are subjected to a faster Brownian motion. However, not necessarily, this makes them qualitatively more significant than those particle(s) (or assembled structures) that, as a result of their size, scatter at a slower decay rate.

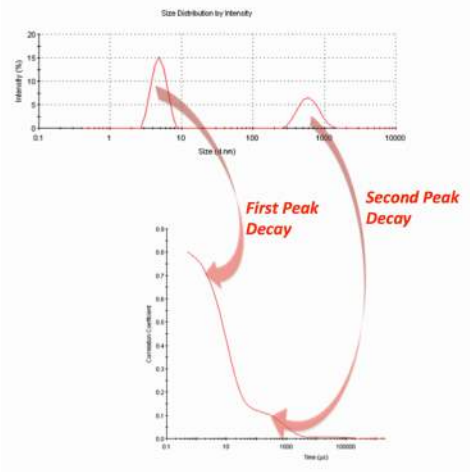


Fig. 6.18 *The correlation between the correlation coefficient decays and the 2 peaks of intensity scattering has been represented in this picture, (Agnese Zicari ©, 2015).*

The UV spectrophotometry of lysozyme solutions during crystallization

A more quantitative description of the bulk nucleation phenomenon has been attained by means of UV spectrophotometry methods. That is, the understanding of the UV light microscopy data from chapter 5 was ameliorated by means of UV spectrophotometry tests. 5 mg/ml lysozyme solutions with a broad range of precipitant concentrations (from 3 – 8 % v/v) have been, indeed, tested for absorption in the 320 – 380 nm lambda range and through 10, or 40, mm path length quartz cuvettes. Quartz cuvettes have been preferred, for these tests, as any interference due to adsorption, or heterogeneous nucleation, might become an unwanted uncontrollable factor to plot the turbidity data at 350 nm.

The solutions were prepared in class-100 clean rooms according to the procedure δ, though a wider range of precipitant concentrations was regarded in this instance. The following cleaning protocol was performed, before every use, on both types of quartz cuvettes:

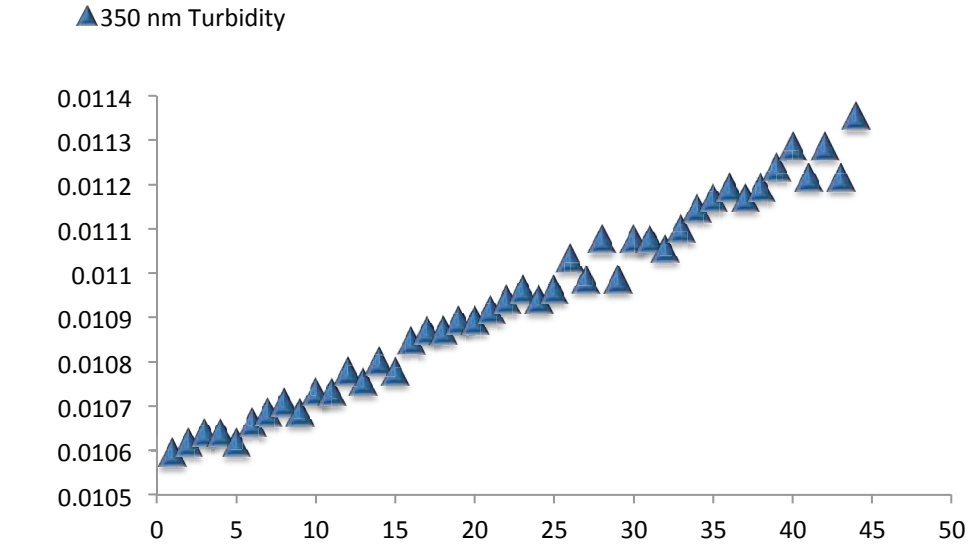
1. aceton
2. ethanol and water
3. Triton X-100 (rinsing; 1- abundant water, 2- distilled water)

The following procedure was followed, thereafter, to perform the UV spectrophotometry tests:

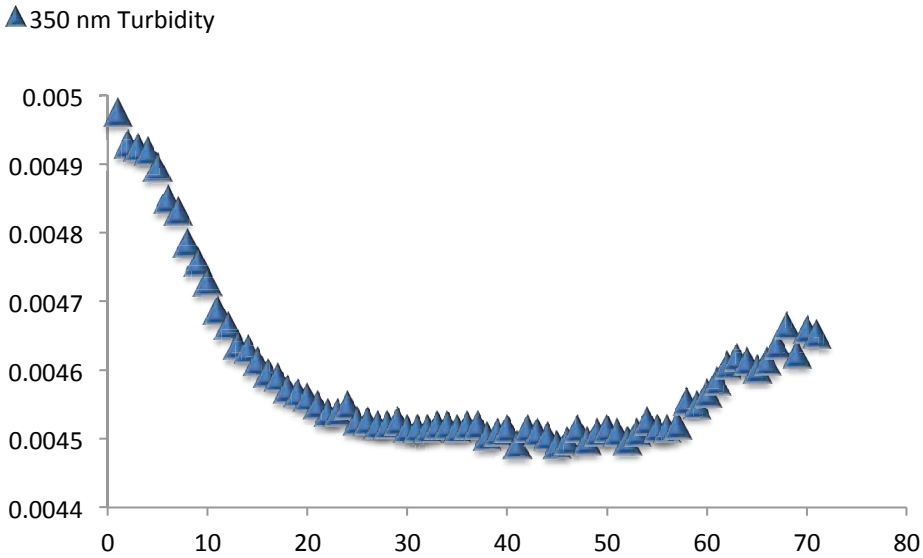
Procedure κ

Procedure κ	*Description*
Dust-rinsing	the (clean) quartz cuvettes were rinsed with 0.45 μm filtered water and dried with compressed air in class-100 clean rooms
Preparation of the lysozyme crystallising solution (procedure δ)	preparation of a (5 mg/ml) lysozyme solution in 50 mM borate buffer by adding the precipitant solution
Cuvette filling & sealing with additional sample filtration	the cuvettes were filled up to 2/3, while filtering the solution (with 220 nm cut-off filters), and sealed with caps in class-100 clean rooms
Placing in a Perkin Elmer UV/Vis spectrophotometer	the sealed cuvettes were placed in the UV equipment at RT (25 °C) and a 320 – 380 nm λ range was set
Measurement	24 – 62 hrs

***



(a)



(b)

Fig. 6.19 *The (350 nm) turbidity values of the 5 mg/ml lysozyme solution at high precipitant concentration ≈ 8 % v/v: (a) the plot over 48 hrs may show that the nucleation process is progressively increasing over the 48 hrs (a 10 mm path length was used on this occasion). (b) the plot over 66 hrs may reveal that for longer path lengths the sedimentation process blurs the nucleation process since time 0 (a 40 mm path length was used on this occasion), (Agnese Zicari ©, 2010).*

According to the UV spectroscopy plots in Fig. 6.19, although quartz cuvettes have been used, there may be some interferences due to heterogeneous crystallization. This may happen since time 0 hr, as observed in Fig. 6.18 (a), or after time 60 hrs, as observed in Fig. 6.19 (b). Since the data in Fig. 6.18 are related to the high precipitant concentration tests, a similar test has

been performed at the 3 % v/v final precipitant concentration. The results from the latter are shown in Fig. 6.20. Nevertheless, also in this instance, heterogeneous crystallization phenomena were observed.

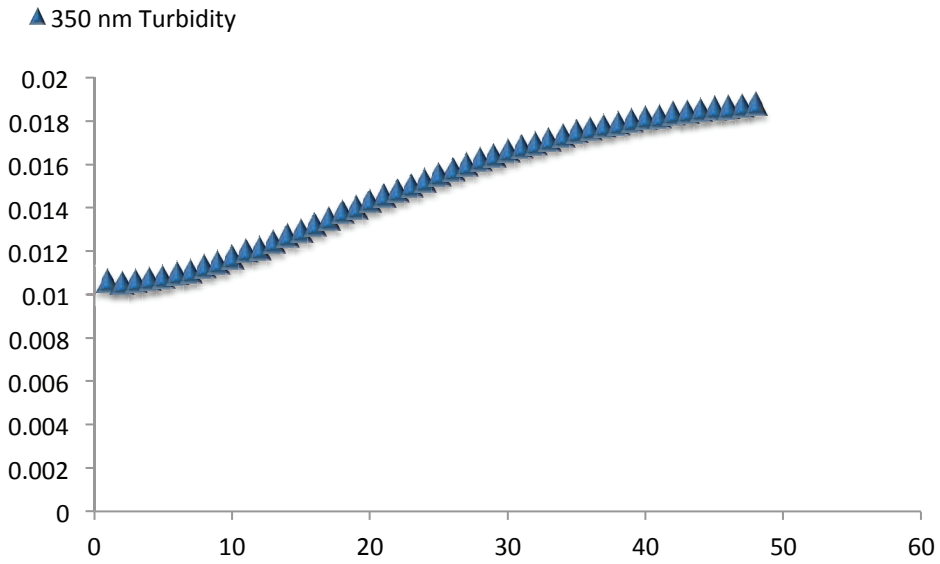


Fig. 6.20 *The (350 nm) turbidity values of the 5 mg/ml lysozyme solution at low precipitant concentration ≈ 3 % v/v: the turbidity data are plotted over 48 hrs and these may reveal that the heterogeneous nucleation is proceeding over time (10 mm path length was used on this occasion), (Agnese Zicari ©, 2010).*

As a result of all the above plots (as well as the observations from section 5.2 and section 6.4.2), the UV spectrophotometer detector, very probably, may not be sufficiently sensitive to discern the different absorptions relating to the infinitesimal local variations of turbidity. Nevertheless, these plots may confirm that there are two contemporary on-going local metaphase phenomena in the lysozyme crystallising solution, the bulk nucleation (or "demixing") and, maybe, a pseudo-sedimentation phenomenon that overlaps with the nucleation. Indeed, the overlapping dynamics of different bulk phenomena might become more evident, especially, when the nucleation in the bulk was selectively regarded.

Summary & Recommendations

According to Lutsko (2012) proteins nucleate from a metastable solution where spatial mass fluctuations form amorphous clusters, first, and structured agglomerations, thereafter. Additional modelling, infers that the grouping of protein molecules is locally originated as a result of multifactorial correlations, since these molecules are simultaneously subjected to translation and orientation as well as conformational activity. Videlicet, statistically or kinetically speaking, proteins are stereochemically wobbling molecules. Indeed, local equilibria (i.e., misfolding, unfolding, refolding or grouping) might arise from solvent (or solute) mediated local dynamics (Anfinsen, 1973; Chan et al., 1994; Guo et al., 1995; Lomakin et al., 2003; Klimov et al., 2003). Earlier in this report, it has been inferred already that the copolymeric adsorption from a solution on to a solid-liquid interface is not diffusion related only. Videlicet, conformational dynamics, almost certainly, influence the solute adsorption, and structuring, at the aforementioned interface (Ward et al., 1944/1946; Varoqui et al., 1986; Schaaf et al., 1987; Clark et al., 2007).

In fact, the passage of a protein molecule from its natural state into an intermediate conformational state has, also, been defined as an extremely slow and influenceable transition (Creighton, 1997). This would mean that the latter is also constrained by adjoining dynamics. Videlicet, extraneous factors, such as the local features at the solid-liquid interface, may well induce conformational bulk equilibria that initiate ordered structuring within the interface compartment (Kaulmann et al., 2003). Hence, a conformationally catalysed compartment at the aforementioned interface would progressively transform the surface tension local values when certain transitions occurred, or reoccurred (Gibbs J.W. et al., 1961; Guggenheim et al., 1967). Local changes in the surface tension may, in turn, govern the structuring of protein molecules at the interface (Abraham et al. 2009). Videlicet, for a given copolymer, local surface

energy decrements may allow for certain intermolecular interactions that initiate crystallization rather than amorphous aggregation (Guo et al., 1995; Junghans et al., 2008).

Accordingly, a novel approach to investigate the, conventionally regarded, lysozyme heterogeneous dynamics has been suggested in this work. Videlicet, a multifactorial dependence has been inferred and the possibility to control this dependence during nucleation has been assessed. Indeed, the conventional lysozyme crystallizing solution has been reformulated, in this work, i.e., the salt-excess interference on its nucleation has been this way controlled. Also, the new formulation, featuring low solution ionic strength and low lysozyme concentration, presents rapid homogeneous crystallization times that have been approximately characterised by DLS, UV spectroscopy and x-ray analysis. Finally, a device, which performs crystallization in an air-depleted micro-batch environment, has been invented to control critical factors, such as the entrainment of air droplets, that interfere at the solid-liquid interface.

Furthermore, collaborations have, also, been established to engineer homogenous features on large enough surfaces. Substrates with submicron- and nano-scale topographies that are suitable for silanization have been, hence, manufactured. Specifically, two different types of patterned surfaces have been manufactured: those bearing submicron epoxy-polymer structures and those bearing nano-periodic silicone-based structures. The first set of substrates for crystallization are 5 × 5 mm square chips bearing 180 nm pitch epoxy-polymer grooves. These have been fabricated from a (6 inch diameter and 600 μm thick) silicon (100) wafer by, first, performing on this a two-stage imprinting procedure with a PDMS-soft stamp (Obducat ltd.). Afterwards, the patterned wafer has been diced via a stealth dicing procedure (Tam et al., 1992). The second set of substrates, instead, are 25 × 25 mm square slides bearing narrow dot patterns (i.e., patterns in the 45 − 52.5 nm size range). These have been directly written on a silicone-based resist by means of an interference lithography procedure, first, and a step & repeat lithography procedure, afterwards (Hesch et al., Moser et al., Dattoli et al., 2001; Solak et al., 2002; Auzelyte et al., 2009). Additionally, the homogeneity of the degree of substitution, after silanization via wet chemistry, has been, also, investigated in this work.

Indeed, some of the hydroxyl-terminated (even, or submicron-patterned) substrates have been activated, and modified with different silanes (including the 3,4-epoxy-cyclohexyl-ethyl-trimethoxy silane). The silanization reactions have been, first, optimized on even silicon units, by characterizing the silanized surfaces with different surface analysis techniques, such as XPS, ellipsometry, AFM, and contact angle measurement. Subsequently, the stability of the even epoxy-silanized substrates, and the submicron-patterned epoxy-polymer, has been characterised after exposure to cleaning, plasma activation and crystallization conditions by means of additional surface analysis techniques (including SEM). Finally, the crystallization of lysozyme was tested on the standard, or activated, epoxy-surfaces by pouring the low-salt formulation in the above crystallization device, i.e., the lysozyme hetero- and homo-geneous nucleation times have been compared.

Therefore, a modern research approach to study the dynamics that govern protein adsorption & nucleation on surfaces with different chemistries (or morphologies) has been initiated in this project. Presumably, this approach will lead to a certain control of the lysozyme heterogeneous nucleation times (and, possibly, crystal morphologies). Videlicet, an upgraded device with 2 inlets (an inlet for the vapour, which is in equilibrium with a reservoir of the buffered lysozyme solution, and an inlet for the low-salt crystallizing lysozyme solution) might be further developed. Subsequently, the lysozyme metastable region might be, also, characterised by means of more valuable techniques (including multi angle DLS), and its heterogeneous nucleation pattern on even, and nano- (or submicron) -patterned, surfaces bearing different chemistries might be plotted against time. Finally, a higher understanding of the correlation among the different solution factors that govern the lysozyme heterogeneous nucleation might be attained by means of coarse-grained simulations. The abstracts, and pictures, in the Appendix B provide preliminary information to proceed with the simulation work that has been initiated in this project. The engineering of nucleating surfaces with crystallising nano-features that controlled the nucleation initiation of proteins would be the desired ultimate outcome of any additional future work.

References

Abraham D. B., 2009, Newman C. M.; Equilibrium Stranski-Krastanow and Volmer-Weber models, A letters Journal Exploring the Frontiers of Physics, 86, pp. 16002.

Adrover M., 2010, Pauwels K., Prigent S., de Chiara C., Xu Z., Chapuis C., Xu Z., Chapuis C., Pastore A., Rezaei H.; Prion fibrillization is mediated by a native structural element that comprises helices H2 and H3, Journal of Biological Chemistry, 285, pp. 21004.

Aguzzi A., 2010, O'Connor T.; Protein aggregation diseases: pathogenicity and therapeutic perspectives, Nature Reviews Drug Discovery, 9, pp. 237.

Alahverdjieva S. V., 2007, Grigoriev D.O., Ferri J. K., Fainerman V. B., Aksenenko E. V., Leser M. E., Michel M., Miller R.; Adsorption experiments from mixed protein & surfactant solutions, Royal Society of Chemistry, 308, pp. 209.

Anfinsen C. B., 1973; Principles that govern the folding of protein chains, Science, 181, pp. 223.

Angermann H., Henrion W., Röseler A., Rebien M., 2000; Wet-chemical passivation of Si(111)- and Si(100)-substrates, Materials Science and Engineering B73, pp.178.

Arakawa T., 2007, Ejima D., Tsumoto K., Obeyama N., Tanaka Y., Kita, Y., Timasheff S. N.; Suppression of protein interactions by arginine: a proposed mechanism of the arginine effects, Biophysical Chemistry, 127, pp. 1.

Arnaudov L. N., 2007, de Vries R.; Theoretical modelling of the kinetics of fibrillar aggregation of bovine β-lactoglobulin at pH 2, Journal of Chemical Physics, 126, 14, pp. 145106.

Atha D. H., 2012, Reipa V.; Quantitative measurement of p53/p53-antibody interactions by quartz crystal microbalance: A model system for immunochemical calibration, Journal of Biophysical Chemistry, 3, 3, pp. 211.

Austin M. D., 2004, Haixiong Ge, Wei Wu, Mingtao Li, Zhaoning Yu; Fabrication of 5 nm linewidth and 14 nm pitch features by nano-imprint lithography, Applied Physics Letters, 84, 26, pp. 5299.

Auzelyte V., 2009, Dais C., Farquet P., Grützmacher D., Heyderman L.J., Luo F., Olliges S., Padeste C., Sahoo P.K., Thomson T., Turchanin A., David C.; Extreme ultraviolet interference lithography at the Paul Scherrer Institut, Journal of Micro/Nanolithography, MEMS, and MOEMS-SPIE, 8, 2, pp. 021204.

Baer D. R., 2003, Engelhard M. H., Lea A. S.; Introduction to surface science spectra data on electron and x-ray damage: Sample degradation during XPS and AES measurements, Surface Science Spectra, 10, pp. 47.

Baszkin A., 1993, Boissonnade M. M.; Competitive adsorption of albumin against collagen at solution-air and solution-polythylene interfaces, Journal of Biomedical Material Research, 27, pp. 145.

Bemporad F., 2012, De Simone A., Chiti F., Dobson C. M.; Characterizing intermolecular interactions that initiate native-like protein aggregation, Biophysical Journal, 102, pp. 2595.

Bennett M. J., 2006, Sawaya M. R., Eisenberg D.; Deposition diseases and 3D domain swapping, Structure, 14, pp. 811.

Berne B. J., 2000/1975, Pecora R.; Dynamic Light Scattering with Applications to Chemistry Biology and Physics, Dover Books.

Boström M., 2005, Tavares F.W., Finet, S., Skouri-Panet F., Tardieu A., and Ninham B.W.; Why forces between proteins follow different Hofmeister series for pH above and below Ip, Biophysical Chemistry, 117, pp. 217.

Boström M., 2006, Deniz V., Franks G.V., Ninham B.W.; Extended DLVO theory: electrostatic and non-electrostatic forces in oxide suspensions, Advances in Colloid and Interface Science, 123–126, pp. 5.

Branden C. I., 1991, Tooze J.; Introduction to Protein Structure, Garland Publishing of York.

Broide M. L., 1996, Tominc T. M., Saxowsky D. M.; Using phase transitions to investigate the effect of salts on protein interactions, Physical Review, 53, 6, pp. 6325.

Bugg C. E., 1993, Carson W. M., Montgomery J. A.; Drugs by design, Scientific American, 269, 6, pp. 92.

Buijs J., 1998, Britt D. W., Hlady V.; Human growth hormone adsorption kinetics and conformation on self-assembled monolayers, Langmuir, 14, pp. 335.

Cacioppo E., 1991, Pusey M. L.; The Solubility of the tetragonal form of hen egg-white lysozyme from pH 4.0 to 5.4. Journal of Crystal Growth, 114, 3, pp. 286.

Campbell I., 2012; Biophysical Techniques, Oxford University Press, Section 8.

Carfagna C., 1997; Amendola E., Giamberini M., Liquid crystalline epoxy based thermosetting polymers, Progress in Polymer Science, 22, pp. 1607.

Chambers S. A., 2000; Epitaxial growth and properties of thin film oxides, Surface Science Report, 39, pp. 105.

Chan H. S., 1994, Dill K. A.; Transition states and folding dynamics of proteins and hetero-polymers, Journal of Chemical Physics, 100, pp. 9238.

Chayen N. E., 2004; Turning protein crystallization from an art into a science, Current Opinion in Structural Biology, 14, pp. 577.

Chayen N. E., 2006, Saridakis E., and Richard P.; Experiment and theory for heterogeneous nucleation of protein crystals in a porous medium, Proceedings of the National Academy of Sciences, 103, 3, pp. 597.

Chun J., 2006, Je-Luen L., Car R., Aksay I.A., Saville D.A.; Anisotropic adsorption of molecular assemblies on crystalline surfaces, Journal of Physical Chemistry B, 110, pp. 16624.

Clark A.J., 2007, Kotlicki A., Haynes C.A., Whitehead L.A.; A new model of protein adsorption kinetics derived from simultaneous measurement of mass loading and changes in surface energy, Langmuir, 23, pp. 5591.

Cohen S.A., 2012, Vendruscolo M., Dobson C. M., Knowles T.P.J.; From macroscopic measurements to microscopic mechanisms of protein aggregation, Journal of Molecular Biology, 421, pp.160.

Craighead H.G., 1984; 10 nm resolution electron‑beam lithography, Journal of applied physics, 55, pp. 4430.

Creighton T.E., 1997; Protein Structure, Second Edition, IRL Press of Oxford University.

Cruzeiro-Hansson L., 2001, Silva P.A.S.; Protein folding: thermodynamic versus kinetic control, Journal of Biological Physics, 27, S6.

Curtis R. A., 1998, Montaser A., Prausnitz J. M., Blanch H. W.; Protein-protein and protein-salt interactions in aqueous protein solutions containing concentrated electrolytes, Biotechnology and Bioengineering, 58, pp. 451.

Cushman D.W., 1991, Ondetti, M. A.; History of the design of captopril and related inhibitors of angiotensin converting enzyme, Hypertension; Journal of the American Heart Association, 17, pp. 589.

Datar R. V., 1996, Rosen C.G.; In Biotechnology: A Multi-Volume Comprehensive Treatise, Vol. 3, Stephanopoulos G. Editors of New York.

D'Arcy A., 2003, Mac Sweeney A., and Haber A.; Using natural seeding material to generate nucleation in protein crystallization experiments, Acta Crystallographica D59, pp. 1343.

Debenedetti P. G., 1996; Metastable liquids: concepts and principles, Princeton University Press of New Jersey, USA.

Deckman H. W., 1982, Dunsmuir J. H.; Natural lithography, Applied Physic Letters, 41, pp. 377.

Dennis S., 2000, Camacho C.J., Vajda S.; Continuum electrostatic analysis of preferred solvation sites around proteins in solution, Proteins: Structure, Function, and Genetics, 38, pp. 176.

De Oteyza D. J., 2012, Perera P. N., Schmidt M., Falch, M., Dhuey S. D., Harteneck B. D., Schwartzberg A. M., Schuck P. J., Cabrini S., Olynick D. L.; Sub-20 nm laser ablation for lithographic dry development, Nanotechnology, 23, pp. 185301.

Devereaux C. A., 2002, Baker S. M.; Surface features in Langmuir-Blodgett monolayers of predominantly hydrophobic poly-styrene/poly-ethylene-oxide diblock co-polymer, Macromolecules, 35, pp. 1921.

Einstein A., 1910, Theorie der opaleszenz von homogenen flüssigkeiten und flüssigkeitsgemischen in der nähe des kritischen zustandes, Annlen der Physik.

El-Ganainy R., 2007, Christodoulides D. N., Rotschild C., Segev M.; Soliton dynamics and self-induced transparency in nonlinear nano-suspensions, OPTICS EXPRESS, 15, 16, pp. 10207.

Etzkorn M., 2011, Bockmann A., Baldus M.; Kinetic analysis of protein aggregation monitored by real-time 2D solid-state NMR spectroscopy, Journal of Bimolecular NMR, 49, pp. 121.

Feller W., 1966; An introduction to probability theory and it's applications/Vol. I, 3rd Edn, John Wiley of New York.

Ferguson N., 2003, Berriman J., Petrovich M., Sharpe T. D., Finch J. T., Fersht A.R.; Rapid amyloid fibril formation from the fast-folding WW domain FBP28, Proceedings of the National Academy of Sciences, 100, pp. 9814

Fermani S., 2001, Falini G., Minnucci M., Ripamonti A.; Protein crystallization on polymeric film surfaces, Journal of Crystal Growth, 224, pp. 327.

Fermani S., 2013, Vettraino C., Bonacini I., Marcaccio M., Falini G., Gavira J. A. and Garcia Ruiz J. M.; Heterogeneous crystallization of proteins: is it a prenucleation clusters mediated process?, Crystal Growth and Design, 13, 7, pp. 3110.

Fick A., 1855; On liquid diffusion, Philosophical Magazine and Journal of Science, 10, pp. 31.

Fields G. B., 1992, Alonso D.O.V., Stigter D., Dill K. A.; Theory for the aggregation of proteins and copolymers, Journal of Physical Chemistry, 96, pp. 3974.

Finet S., 2004, Skouri-Panet F., Casselyn M., Bonnete F., Tardieu A.; The Hofmeister effect as seen by SAXS in protein solutions, Current Opinions in Colloid Interface Science , 9, pp. 112.

Fischer U. Ch., 1981, Zingsheim H. P.; Submicroscopic pattern replication with visible light, Journal of Vacuum Science and Technology, 19, pp. 881.

Forciniti D., 1991, Hall C.K., Kula M.R.; Protein partitioning at the isoelectric point: influence of polymer molecular weight and concentration and protein size, Biotechnology and Bioengineering, 38, pp. 986.

Forsythe E.L., 1999, Judge R.A., Pusey M. L.; Tetragonal chicken egg white Lysozyme solubility in sodium chloride solutions, Journal of Chemical & Engineering Data, 44, pp. 637.

Frenkel D., 2002; Soft condensed matter, Physica A: Statistical Mechanics and its Application, 313, pp. 1.

Fritz J., 2002, Cooper E. B., Gaudet S., Sorger P. K., Manails S. R.; Electronic detection of DNA by its intrinsic molecular charge, Proceedings of the National Academy of Sciences , 99 , pp. 14142.

Gadegaard N., 2006, Dalby M. J., Martines E., Seunarine K., Riehle M. O., Curtis A. S. G., Wilkinson C. D. W.; Nano-patterned surfaces for biomaterial applications, Advances in Science and Technology, Vol.53, Vincenzini P., Barbucci R. Editors.

Galisteo F., 1995, Nord W.; Adsorption of lysozyme and α-lactalbumin on poly-styrenesulfonate lattices 2. Proton titrations, Colloids Surfaces B: biointerfaces, 4, pp. 389.

George A., 1997, Chiang Y., Guo B., Arabshahi A., Cai Z., Wilson W. W.; Second virial coefficient as predictor in protein crystal growth, Methods in Enzymology, 276, pp. 100.

Gibbs J. W., 1876; On the equilibrium of heterogeneous substances, Transactions of the Connecticut Academy III, pp. 108.

Gilch S., 2001, Winklhofer K. F., Groschup M. H., Nunziante M., Lucassen R., Spielhaupter

C., Muranyi W., Riesner D., Tatzelt J., Schätzl H. M.; Intracellular re-routing of prion protein prevents propagation of PrP(Sc) and delays onset of prion disease, EMBO Journal, 20, pp. 3957.

Ginnai T. M., 1980, Oxley D. P., Pritchard R. G.; Langmuir-Blodgett Films, edited by W.A. Barlow (Elsevier Science ltd), pp. 245.

Goyne W. K., 2002; Surface charge of variable porosity Al2O3(s) and SiO2(s) adsorbents, Journal of Porous Materials, 9, pp. 243.

Guggenheim E. A., 1967; Thermodynamics: An Advanced Treatment for Chemists and Physicists, 5th ed., Wiley of New York.

Guo Z., 1995, Thirumalai D.; Kinetics of protein folding: nucleation mechanism, time scales, and pathways, Biopolymers, 36, 1, pp. 83.

Guyt, J. M., 2002, Van Eesbeek M., Van Papendrecht G.; Detection of organic contamination on surfaces by infrared spectroscopy, Proceedings of SPIE - The International Society for Optical Engineering, 4774, pp. 262.

Hua H., 2001, Hale T., Yang X., Wilson L. J.; A spectrophotometer-based method for crystallization induction time period measurement, Journal of Crystal Growth, 232, pp. 86.

Hamada H., 2009, Arakawa T., Shiraki K.; Effect of additives on protein aggregation, Current Pharmaceutical Biotechnology, 10, pp. 400.

Hampton Research Corp., 1999; Crystallization Research Tools, vol. 9, No. 1, Laguna Niguel, CA.

Hazelwood L. F., 2001; Can't Live Without it: The Story of Hemoglobin in Sickness and in Health, Nova.

Heinemann U., 2003, Bussow K., Mueller U., and Umbach P.; Facilities and methods for the high-throughput crystal structural analysis of human proteins, Accounts of Chemical Research, 36, pp. 157.

Hendrickx N., 2005, Suyal H., Van Steenberge G., McCarthy A., Walker A., Ottevaere H., Thienpont H., Taghizadeh M., Van Daele P.; Laser ablation and laser direct writing as enabling technologies for the definition of micro-optical elements, SPIE Proceedings; Integrated Optics: Theory and Applications, 5956, pp. 59561B.

Hesch K., 2001, Pellegrin E., Rossmanith R., Steininger R., Saile V., Wüst J., Forschungszentrum Karlsruhe, Germany - Dattoli G., Doria A., Gallerano G. P., Giannessi L., Ottaviani P. L., ENEA, Frascati, Italy - Moser H. O., Singapore Synchrotron Light Source/SSLS, National University of Singapore; Proceedings of the 2001, Particle accelerator conference, Chicago.

Hemming S.A., 1995, Bochkarev A., Darst S. A., Kornberg R. D., Ala P., Yang D. S., Edwards A. M.; The mechanism of protein crystal growth from lipid layers, Journal of Molecular Biology 246, pp. 308.

Iovan A., 2012, Fischer M., Lo Conte R., Korenivsk V.; Sub-10 nm colloidal lithography for circuit-integrated spin-photo-electronic devices, Beilstein Journal of Nanotechnology, 3, pp. 884.

Izawa Y., 2008, Tanaka S., Kikuchi H., Tsurumi Y., Miyanaga N., Esashi M., Fujita M.; Debris-free in-air laser dicing for multi-layer MEMS by perforated internal transformation and thermally-induced crack propagation, Micro Electro Mechanical Systems (MEMS), pp. 822.

Junghans C., 2008, Bachmann M., Janke W.; Thermodynamics of peptide aggregation processes: an analysis from perspectives of three statistical ensembles, Journal of Chemical Physics, 128, pp. 085.

Kahle P.J., 2008; Alpha-synucleinopathy models and human neuropathology: similarities and differences, Acta Neuropathologica, 115, pp. 87.

Kaulmann G., 2003, Palm G. J., Schilling K., Hilgenfeld R.; An unfolding/refolding step helps in the crystallization of a poorly soluble protein, Acta Crystallographica D, 59, 7, pp. 1243.

Kelly J. W., 2000, Mechanisms of amyloidogenesis, Nature Molecular & Structural Biology, 7, pp. 824.

Kern K., 1991, Niehus H., Schatz A., Zeppenfeld P., Goerge J., Comsa G.; Long-range spatial self-organization in the adsorbate-induced restructuring of surfaces: Cu{110}–(2×1)O, Physical Review Letters, 67, pp. 855.

Kim G.B., 2007, Park C. D., Seo D. S., Hong S. J., Delamination analysis of low-temperature processed SU-8 photoresist for MEMS device fabrication, Key Engineering Materials, Nam S. W., Chang Y. W., Lee S. B. and Kim N. J. Editors, 345-346, pp. 1397.

Klimov D. K., 2003, Thirumalai D.; Dissecting the assembly of Aβ (16-22) amyloid peptides into antiparallel β sheets, Structure, 11, pp. 295.

Kurth D. G., 1993, Bein T.; Surface reactions on thin layers of silane coupling agents, Langmuir, 9, pp. 2965.

Leader B., 2008, Baca Q. J., Golan D. E.; Protein therapeutics: a summary and pharmacological classification, Nature Reviews Drug Discovery, 7, pp. 21.

Li J., 2009, Sheng X. H.; Nano-tribological characteristics of TiO2 films on 3-mercaptopropyl-Trimethoxy-silane sulfonated self-assembled monolayer, Bulletin of Material Science, 32, 5, pp. 481.

Li Y., 2009, Roberts C. J.; Lumry-Eyring nucleated-polymerization model of protein aggregation kinetics. 2. Competing growth via condensation and chain polymerization, Journal of Physical Chemistry B, 113, 19, pp. 7020.

Lima E. R. A., 2007, Tavares F. W., Biscaia Jr. E. C.; Finite volume solution of the modified Poisson–Boltzmann equation for two colloidal particles, Physical Chemistry Chemical Physics, 9, pp. 3174.

Lindroos V. et al., 2010; Handbook of Silicon Based MEMS Materials and Technologies, Elsevier.

Liu S., 2004, Maoz R., Sagiv J.; Planned nanostructures of colloidal gold via self-assembly on hierarchically assembled organic bilayer template patterns with in-situ generated terminal amino functionality, Nano Letters, 4, pp. 5.

Lomakin A., 2003, Asherie N., Benedek G. B.; Liquid-solid transition in nuclei of protein crystals, Proceedings of the National Academy of Sciences, USA, 100, 18, pp. 10254.

Lu J. R., 1999, Su T. J.; The effect of solution pH on the structural conformation of lysozyme layers adsorbed on the surface of water, Journal of Physical Chemistry B, 103, pp. 5903.

Lutsko J. F., 2012; A dynamical theory of nucleation for colloids and macromolecules, Journal of Chemical Physics, 136, pp. 034509.

Manno M., 2003, Xiao C., Bulone D., Martorana V., San Biagio P. L.; Thermodynamic instability in supersaturated Lysozyme solutions: effect of salt and role of concentration fluctuations, Physical Review E, 68, 1, pt.1.

Martines E., 2006, Seunarine K., Morgan H., Gadegaard N., Wilkinson C. D., Riehle M. O.; Air-trapping on biocompatible nano-patterns, Langmuir, 22, 26, pp. 11230.

Masino L., 2010, Nicastro G., Calder L., Vendruscolo M., Pastore A.; Functional interactions as a survival strategy against abnormal aggregation, The Faseb Journal, 25, pp. 45.

Mc Elroy H. E., 1992, Sisson G. W., Schoettlin W. E., Aust R. M., Villafranca J. E.; Studies on engineering crystallizability by mutation of surface residues of human thymidylate synthase, Journal of Crystal Growth, 122, pp. 265.

McPherson A., 1987, Schlichta P. J.; Facilitation of the growth of protein crystals by heterogeneous/epitaxial nucleation, Journal of Crystal Growth, 85, pp. 206.

McPherson A., 1991; A brief history of protein crystal growth, Journal of Crystal Growth, 110, pp.1.

Miller R., 2000, Fainerman V. B.; Dynamics of protein and mixed protein/surfactant adsorption layers at the water/fluid interface, Advances in Colloid and Interface Science, 86, pp. 39.

Milner S. R., 1907; On the surface concentration and the formation of liquid films, Philosophical Magazine, 13, 6, pp. 96.

Muschol M., 1997, Rosenberger F., Liquid–liquid phase separation in supersaturated Lysozyme solutions and associated precipitate formation/crystallization, Journal of Chemical Physics, 107, pp. 1953.

Nanev C. N., 2006, Dimitrov I., Hodjaoglu F.; Hypergravity as a Crystallization Tool, Annals of the new York Academy of Sciences , 1077, pp. 172.

Nanev C. N., 2007; On the slow kinetics of proteins crystallization, Journal of Crystal Growth & Design, 7, 8, pp. 1533.

Narayanan J., 2003, Liu X. Y.; Protein interactions in under-saturated and super-saturated solutions: a study using light and x-ray scattering, Biophysical Journal, 84, pp. 523.

Nelson R., 2006, Eisenberg D.; Structural models of amyloid-like fibrils, Advances in Protein Chemistry, 73, pp. 235.

Ng S. P., 2007, Randles L. G., Clarke J.; Single molecule studies of protein folding using atomic force microscopy, Methods in Molecular Biology, 350, pp. 139.

Nongyue He, 2009; Biochips nano-technology, Southeast University, (China),
Hari Singh Nalwa, Editor-in-Chief, Journal of Nanoscience and Nanotechnology, USA.

Northrup S. H., 1992, Erickson H. P.; Kinetics of protein-protein association explained by Brownian dynamics computer simulation, Proceedings of the National Academy of Sciences, 89, pp. 3338.

Oki H., 1999, Matsuura Y., Komatsu H., Chernov A. A.; Refined structure of orthorhombic Lysozyme crystallized at high temperature: correlation between morphology and intermolecular contacts, Acta Crystallographica D: Biological Crystallography, D55, pp. 114.

Oshinowo J., 1994, Nishioka M., Ishida S., Arakawa Y.; Highly uniform InGaAs/GaAs quantum dots (≈15 nm) by metal-organic chemical vapour deposition, Applied Physics Letters, 65, 11, pp. 1421.

Otsubo S., 2009, Kimata N., Okutsu I., Oshikawa K., Ueda S., Sugimoto H., Mitobe M., Uchida K., Otsubo K., Nitta K., Akiba T.; Characteristics of dialysis-related amyloidosis in patients on haemodialysis therapy for more than 30 years; Nephrology, Dialysis, Transplantation, 24, pp. 1593.

Parmar A. S., 2007, Gottschall P. E.; Pre-assembled clusters distort crystal nucleation kinetics in supersaturated Lysozyme solutions, Biophysical Chemistry, 129, pp.224.

Pellicane G., 2012; Colloidal model of lysozyme aqueous solutions: a computer simulation and theoretical study, Journal of Physical Chemistry B, 116, pp. 2114.

Penkova A., 2002, Chayen N., Saridakis E., Nanev C.; Nucleation of protein crystals in a wide continuous supersaturation gradient, Acta Crystallographica, D58, pp. 1606.

Plass R., 2001, Last J. A., Bartelt N. C., Kellogg G. L.; Nanostructures: self-assembled domain patterns, Nature, 412, pp. 875.

Podhipleux N., 1999, Damodaran S., McGuire J., Bothwell M.K.; Structural stability effects on T4 lysozyme adsorption at the air–water interface, Colloids and Surfaces B: Biointerfaces, 13, pp. 167.

Pohl K., 1999, de la Figuera J., Bartelt M. C., Hrbek J., Hwang R.Q.; Thermal vibrations of a two-dimensional vacancy island crystal in a strained metal film, Surface Science, 433–435, pp. 506.

Pullara F., 2005, Emanuele A., Palma-Vittorelli M. B., Palma M. U., 2005; Lysozyme crystallization rates controlled by anomalous fluctuations, Journal of Crystal Growth, 58, pp. 426.

Pusey M. L., 1986, Snyder R. S., Naumann R.; Growth kinetics for tetragonal lysozyme crystals, Journal of Biological Chemistry, 261,14, pp. 6524.

Qi X., 2007, Portman J. J.; Excluded volume, local structural cooperativity, and the polymer physics of protein folding rates, Proceedings of the National Academy of Sciences, 104, 26, pp. 10841.

Relkin P., 2003, Sourdet S., Fosseux P. Y.; Fat crystallization in complex food emulsions: Effects of adsorbed milk proteins and of a whipping process, Journal of Thermal Analysis and Calorimetry, 71, pp. 187.

Radford S. E., 1992, Christopher M. D., Philip A. E.; The folding of hen lysozyme involves partially structured intermediates and multiple pathways, Nature, 358, pp. 302.

Rechendorff K., 2006, Hovgaard M. B.; Enhancement of protein adsorption induced by surface roughness, Langmuir, 22, pp. 10885.

Ricchiuto P., 2012, Brukhno A.V., Auer S.; Protein aggregation: kinetics versus thermodynamics, Journal of Physical Chemistry B, 116, pp. 5384.

Sadana A., 1998; Bioseparations of Proteins: unfolding/folding and validations (Volume I, Separation Science Technology), Editors Satinder Ahuja, USA (CA), pp. 203.

Salemme F. R., 1988, Molecular factors stabilising protein crystals, Journal of Crystal Growth, 90, pp. 273.

Sanjoh A., 1999, Tsukihara T.; Spatiotemporal protein crystal growth studies using microfluidic silicon devices, Journal of Crystal Growth, 196, pp. 691.

Sanjoh A., 2001, Tsukihara T., Gorti S.; Surface-potential controlled Si-microarray device for heterogeneous protein crystallization screening, Journal of Crystal Growth, 232, pp. 618.

Schaaf P., 1987, Déjardin Ph.; Coupling between interfacial protein adsorption and bulk diffusion: a numerical study, Colloids and Surface, 24, 2-3, pp. 239.

Schmid H., 2000, Michel, B.; Siloxane polymers for high-resolution, high-accuracy soft lithography, Macromolecules, 33, pp. 3042.

Scopes R. K., 1982, Protein Purification: Principles and Practice, (Springer-Verlag, Berlin, Heidelberg and New York).

Shang H. M., 2005, Wang Y., Takahash K. I., Cao D. L., Xia Y. N.; Nanostructured super hydrophobic surfaces, Journal of Materials Science, 40, pp. 3587.

Scheraga H. A., 1996; Recent developments in the theory of protein folding: searching for the global energy minimum, Biophysical Chemistry Journal, 59, pp. 329.

Shoichet B. K., 1991, Kuntzt I. D.; Protein docking and complementarity, Journal of Molecular Biology, 221, pp. 327.

Solak H. H., 2002, David C., Gobrecht J., Lin W., Cerrina F.; Four-wave EUV interference lithography, Microelectronic Engineering, 61–62, pp. 77.

Sommer J., 1982, Jonah C., Fukuda R., Bersohn R.; Production and subsequent second-order decomposition of protein disulfide anions: Lengthy collisions between proteins, Journal of Molecular Biology, 159, pp. 721.

Stevens R. C., 2000; Design of high-throughput methods of protein production for structural biology, Structure: Folding & Design, 8, pp. R177.

Stolyarova S., 2002, El-bahar A.; Unexpected room temperature growth of silicon dioxide crystallites on passivated porous silicon, Journal of Crystal Growth, 237 − 239, pp. 1920.

Takagi S., 2011, Matsumoto Y.; Surfactant effects on bubble motion and bubbly flows, Annual Review of Fluid Mechanics, 43, pp. 615.

Tam S. C., 1992, Lennie E. N. Lim, K. Y. Quek; Application of Taguchi methods in the optimization of the laser-cutting process, Journal of Materials Processing Technology, 29, pp. 63.

Tanskanen M., 2008, Peuralinna T., Polvikoski T., Notkola I. L., Sulkava R., Hardy J., Singleton A., Kiuru-Enari S., Paetau A., Tienari P. J., Myllykangas L.; Senile systemic amyloidosis affects 25 % of the very aged and associates with genetic variation in alpha2-macroglobulin and tau: a population-based autopsy study, Annals of Medicine, 40, pp. 232.

Teraoka I., 2002; Polymer Solutions: An Introduction to Physical Properties, (Wiley, New York).

Tessier P. M., 2003, Johnson H. R., Pazhianur R., Berger B. W., Prentice J. L., Bahnson B. J., Sandler S. I., Lenhoff A. M.; Predictive crystallization of ribonuclease A via rapid screening of osmotic second virial coefficients, Proteins- Structure Function and Genetics, 50, pp. 303.

Tomaselli S., 2006, Esposito V., Vangone P., van Nuland N. A. J., Bonvin A., Guerrini R., Tancredi T., Temussi P.A., Picone D.; The alpha-to-β conformational transition of Alzheimer's Aβ (1-42) peptide in aqueous media is reversible: a step by step conformational analysis suggests the location of β conformation seeding, ChemBioChem, 7, pp. 257.

Tosi G., 2011, Fermani S., Falini G., Gavira J. A., Garcia Ruiz J. M.; Hetero- vs homogeneous nucleation of protein crystals discriminated by supersaturation, Journal of Crystal Growth Design, 11, 5, pp. 1542.

Tsekova D., 1999, Dimitrova S., Nanev C. N.; Heterogeneous nucleation (and adhesion) of lysozyme crystals, Journal of Crystal Growth, 196, pp. 226.

Umezawa K., 2001, Nakanishi S., Yoshimura M., Ojima, K., Ueda K., Gibson W. M.; Ag/Cu(111) surface structure and metal epitaxy by impact-collision ion-scattering spectroscopy and scanning tunneling microscopy, Physical Review B, 63, pp. 35402.

Urban G.A., 2006, Albert-Ludwigs-University; BioMems, Springer.

Vaiana S. M., 2005, Rotter M. A., Emanuele A., Ferrone F. A., Palma-Vittorelli M. B.; Effect of T-R conformational change on sickle-cell hemoglobin interactions and aggregation, Proteins, 58, pp. 426.

Van Duyne R. P., 2002, Dick L. A., McFarland A. D., Haynes C. L.; Metal film over nanosphere (MFON) electrodes for surface-enhanced Raman spectroscopy (SERS): improvements in surface nanostructure stability and suppression of irreversible loss, Journal of Physical Chemistry B, 106, pp. 853.

Van Der Veen M., 2004, Norde W., Stuart M. C.; Electrostatic interactions in protein adsorption probed by comparing lysozyme and succinylated lysozyme, Colloids and Surfaces B, 35, 1, pp. 33.

Varoqui R., Pefferkorn E., 1986; Adsorption kinetics at a plane interface: the excluded surface effect, Journal of Colloid Interface Sciences, 109, pp. 520.

Velev O. D., 1998, Kaler E. W., Lenhoff A. M.; Protein interactions in solution characterized by light and neutron scattering: comparison of lysozyme and chymotrypsinogen, Biophysical Journal, 75, pp. 2682.

Vedadi M., 2006, Niesen F. H., Allali-Hassani A., Fedorov O. Y., Finerty, Jr. P. J., Wasney G. A., Yeung R., Arrowsmith C., Ball L. J., Berglund H., Hui R., Marsden B. D., Nordlund P., Sundstrom M., Weigelt J., Edwards A. M.; Chemical screening methods to identify ligands that promote protein stability, protein crystallization, and structure determination, Proceedings of the National Academy of Sciences, 103, 43, pp. 15835.

Viheriälä J., 2009, Tommila J., Dumitrescu M., Toikkanen L., Niemi T., Pessa M.; Applications of UV-nanoimprint soft stamps in fabrication of single-frequency diode lasers, Microelectronic Engineering, 86, 3, pp. 321.

Volmer M., 1926 , Weber A.; Keimbildung in übersättigten gebilden, Zeitschrift für Physikalische Chemie, 119, pp. 277.

Walther F., 2007, Davydovskaya P., Zürcher S., Kaiser M., Herberg H., Gigler A. M. and Stark R. W.; Stability of the hydrophilic behaviour of oxygen-plasma activated SU8 Journal of Micromechanics and Microengineering, 17, pp. 524.

Wanzenboeck H. D., Waid S.; www.intechopen.com.

Ward A. F. H., 1944, Tordai L.; Existence of time-dependence for interfacial tension of solutions, Nature, 154, pp. 146.

Ward A. F. H., 1946, Tordai L.; Time-dependence of boundary tensions of solutions: I. The role of diffusion in time-effects , The Journal of Chemical Physics, 14, 7, pp. 453.

Webb S. D., 2002, Golledge S. L., Cleland J. L., Carpenter J. F., Randolph T. W.; Surface adsorption of recombinant human interferon-gamma in lyophilized and spray-lyophilized formulations, Journal of Pharmaceutical Sciences, 91, pp. 1474.

Westermark P. A., 2011, Westermark G.T., Islet amyloid polypeptide, islet amy-loid, and diabetes mellitus, Physiological Reviews, 91, pp. 795.

Whitesides G. M., 1993, Kumar A.; Features of gold having micrometer to centimeter dimensions can be formed through a combination of stamping with an elastomeric stamp and an alkanethiol ‘‘ink’’ followed by chemical etching, Applied Physic Letters, 63, pp. 2002.

Wood M. A., 2007; Colloidal lithography and current fabrication techniques producing in-plane nano-topography for biological applications, Journal of the Royal Society Interface, 4, pp. 1.

Wuthrich K., 1984, Wagner G.; Internal dynamics of proteins, Trends In Biochemical Science, 9, pp.152.

Yada R. Y., 2000; Proteins in Food Processing, Wood Head Publishing in Food Science and Technology).

Ying-Xin Liu, 2007, Xiu-Juan Wang; Influence of the roughness, topography, and physicochemical properties of chemically modified surfaces on the heterogeneous nucleation of protein crystals, Journal of Physical Chemistry B, 111, pp. 13971.

Young B. R., 1988, Pitt W. G., Cooper S. L.; Protein adsorption on polymeric biomaterials: II. adsorption kinetics., Journal of Colloid Interface Science, 125, pp. 246.

Young S. H., 1982, McCloskey M., Poo, M.; In the Receptors, Conn P. M. Editors (Academic, New York), 1, pp. 511.

Zeng X., 2011, Xu G., Gao Y., An Y.; Surface wettability of (3-aminopropyl) triethoxysilane self-assembled monolayers, Journal of Physical Chemistry B, 115, 3, pp. 450.

Zhang J., 2003, Liu X. Y.; Effect of protein–protein interactions on protein aggregation kinetics, Journal of Chemical Physics, 119, 20, pp. 10972.

Zhao A., 2006, Rodgers V. G. J.; Using TEM to couple transient protein distribution and release for PLGA micro-particles for potential use as vaccine delivery vehicles, Journal of Controlled Release, 113, pp. 15.

Zhao X., 2009, Pan F., Lu J. R.; Interfacial assembly of proteins and peptides: recent examples studied by neutron reflection, Journal of the Royal Society Interface, 6, pp. S659.

List of Websites

http://www.ap-lab.com, (Sept., 23rd, 2013).
http://www.aps.org/units/fiap/meetings/presentations/upload/tompkins.pdf, (Sept., 23rd, 2013).
http://www.biophys.phys.uri.edu, (Sept., 23rd, 2013).
http://www.fda.gov/, (Sept., 23rd, 2013).
http://www.gelest.com/goods/pdf/Library/Roleofpolarity.pdf, (Sept., 23rd, 2013).
http://www.lifetechnologies.com/uk/en/home/technical-resources.html, (Sept., 23rd, 2013).
http://www.loadpoint.co.uk/, (Sept., 23rd, 2013).
http://www.malvern.com, (Sept., 23rd, 2013).
http://www.microscopyu.com/articles/fluorescence/, (Sept., 23rd, 2013).
http://www.nobelprize.org/, (Sept., 23rd, 2013).
http://www.postnova.com/, (Sept., 23rd, 2013).
http://www.ruf.rice.edu/~bioslabs/studies/sds-page/gellab2.html, (Sept., 23rd, 2013).
http://www.wwpdb.org (Feb., 4th, 2015)

Appendix A

Contact details relating to the multi-institutional collaborations

Nanofilm: Surface Analysis, Halcyonics GmbH. Address: Anna-Vandenhoeck-Ring 5, 37081, Göttingen, Germany. Tel. +49-551-9996015, fax: +49-551-9996010, am@nanofilm.de, www.nanofilm.de.

Obducat AB. Address: Scheelevägen 2, SE-223 63 Lund, Sweden. Tel: +46-46-101600, fax: +46-46-101660, info@obducat.com, www.obducat.com.

Eulitha AG. Address: ODRA 101, 5232 Villigen PSI or Althau 1, 5303 Würenlingen, Switzerland. Tel: +41-56-310 4279, fax: +41-56-310 4153, info@eulitha.com, www.eulitha.com.

UCL Cancer Institute and Wolfson Institute for Biomedical Research. Address: Gower Street, London, WC1E 6BT, England. Tel: +44-(0)-20-76796719.

London Centre for Nanotechnology. Address: 17-19, Gordon Square, London, WC1H 0AH, England. Tel: +44-(0)-20-76799904.

King's College. Address: Strand, London, WC2R2LS, England. Tel: +44-(0)-20-7836 5454.

STFC: Science and Technology Facilities Council. Address: Rutherford Appleton Laboratory, Harwell Science and Innovation Campus, Didcot, OX110QX, England. Tel: +44-(0)-123-5445989, fax: +44-(0)-123-5446251.

Toshiba Research Europe Limited, Cambridge Research Laboratory. Address: 208, Cambridge Science Park, Milton Road, Cambridge, CB4OGZ, England. Tel: +44-(0)-1223-436934 / -436900, fax: +44-(0)-1223-436909.

The Manufacturing Engineering Centre. Address: Queen's Buildings, the Parade, Newport Road, Cardiff, CF243AA, England. Tel: +44-(0)-29-20875911, fax: +44-(0)-29-20874695.

X-ray Photoelectron Spectroscopy facility. Address: Faculty of Science, School of Chemistry, University Park, Nottingham, NG72RD, England.

Yield Engineering Systems, Inc.. Address: 203-A Lawrence Drive, Livermore, CA 94551-5152 United States of America. Tel: 888-937-3637 / 925-373-8353, http://www.yieldengineering.com.

Appendix B

Abstracts and sketches relating to the exploratory simulation work

The Effect of Solution pH on the Structure of Lysozyme Layers Adsorbed at the Silica-Water Interface Studied by Neutron Reflection

T. J. Su and J. R. Lu
Department of Chemistry, University of Surrey, Guildford GU2 5XH, U.K.
R. K. Thomas
Physical and Theoretical Chemistry Laboratory, South Parks Road, Oxford OX1 3QZ, U.K.
Z. F. Cui
Department of Engineering Science, Parks Road, Oxford OX1 3PJ, U.K.
J. Penfold
ISIS, CCLRC, Chilton, Didcot OX11 0QX, U.K.
Received June 11, 1997. In Final Form: October 29, 1997

ABSTRACT:

We have studied the structure of lysozyme layers adsorbed at the silica−water interface using specular neutron reflection. The effect of pH on the adsorbed lysozyme layer was examined by manipulating the pH in two different cycles at two constant lysozyme concentrations of 0.03 and 1.0 g dm^{-3}; the first cycle was started at pH = 4 followed by pH = 7 and then 8, before returning to 4; the second cycle was started at pH = 7 followed by a decrease to 4 and then back to 7. The neutron reflectivity profiles showed no hysteresis in either adsorbed amount or structure. There was less adsorption at pH = 4 than at pH = 7 for both lysozyme bulk concentrations. No variation of the reflectivity with time was found at the experimental resolution of about 5 min per measurement. The lysozyme structure at the interface at pH = 4 and pH = 7 was determined from reflectivity profiles at different isotopic compositions of the water. The thickness of the adsorbed layer at the lower concentration of 0.03 g x dm^{-3} was found to be 30 ± 2 Å, suggesting sideways-on adsorption of the ellipsoidally shaped protein. At the higher concentration of 1.0 g dm^{-3} the thickness of the layer was found to be 60 ± 2 Å, suggesting bilayer adsorption with side-on orientation in each layer. These observations disagree with literature results from surface force and ellipsometric measurements which suggest that a side-on monolayer of 30 Å thickness is formed at dilute bulk concentrations, which switches to end-on adsorption of 45 Å thickness as the bulk concentration increases, eventually reaching a bilayer of 90 Å thickness when the bulk lysozyme concentration is further increased. The neutron measurements indicate that the adsorbed amount and the orientation of the globular protein are determined by the electrostatic repulsion between the lysozyme molecules within the layer.

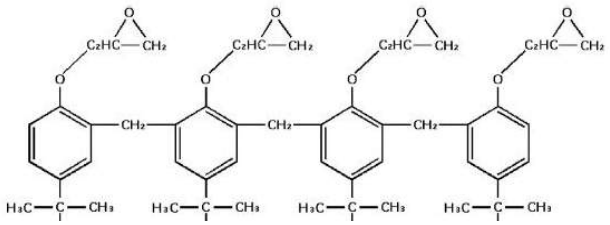
Molecular Dynamics Simulation of Lysozyme Adsorption/Desorption on Hydrophobic Surfaces

Tao Wei, Marcelo A. Carignano, and Igal Szleifer

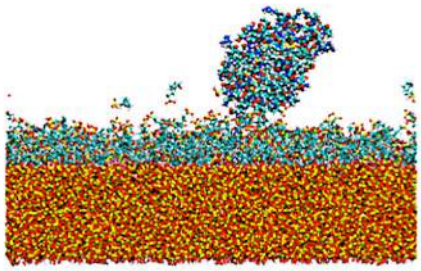
Department of Biomedical Engineering, Department of Chemistry and Chemistry of Life Processes Institute, Northwestern University, Evanston, Illinois 60208, United States

ABSTRACT:

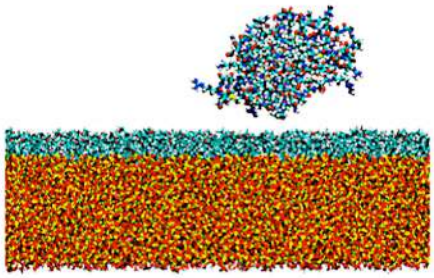
In this work, we present a series of fully atomistic molecular dynamics (MD) simulations to study lysozyme's orientation-dependent adsorption on polyethylene (PE) surface in explicit water. The simulations show that depending on the orientation of the initial approach to the surface the protein may adsorb or bounce from the surface. The protein may completely leave the surface or reorient and approach the surface resulting in adsorption. The success of the trajectory to adsorb on the surface is the result of different competing interactions, including protein-surface interactions and the hydration of the protein and the hydrophobic PE surface. The difference in the hydration of various protein sites affects the protein's orientation-dependent behaviour. Side-on orientation is most likely to result in adsorption as the protein-surface exhibits the strongest attraction. However, adsorption can also happen when lysozyme's longest axis is tilted on the surface if the protein-surface interaction is large enough to overcome the energy barrier that results from dehydrating both the protein and the surface. Our study demonstrates the significant role of dehydration process on hydrophobic surface during protein adsorption.



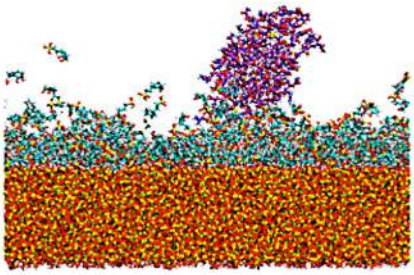
The structure of an epoxy-silane



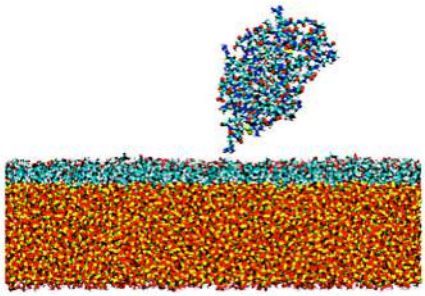
Coarse-grained simulation (by Gromacs) of Lysozyme on a surface after physisorption of an epoxy silane.



Coarse-grained simulation (by Gromacs) of Lysozyme on a surface after chemisorption of an epoxy silane.



Coarse-grained simulation (by Gromacs) of Lysozyme on a surface after physisorption of an open epoxy silane.



Coarse-grained simulation (by Gromacs) of Lysozyme on a surface after chemisorption of an open epoxy silane.

Coarse-grained simulation trials (in collaboration with Dr. Chris Lorenz)
(Pictures by Dr. Chris Lorenz ©)